Physical and biogeochemical features of the Southern Ocean: Their variability and change over the recent past and coming century

by

Natalie M. Freeman

B.S., University of Kansas, 2012

M.S., University of Colorado, 2014

A thesis submitted to the

Faculty of the Graduate School of the

University of Colorado in partial fulfillment

of the requirements for the degree of

Doctor of Philosophy

Department of Atmospheric and Oceanic Sciences

2017

This thesis entitled:

Physical and biogeochemical features of the Southern Ocean: Their variability and change over the recent past and coming century

written by Natalie M. Freeman

has been approved for the Department of Atmospheric and Oceanic Sciences

Nicole S. Lovenduski

Weiqing Han

Date

The final copy of this thesis has been examined by the signatories, and we find that both the content and the form meet acceptable presentation standards of scholarly work in the above mentioned discipline.

Abstract of the Dissertation

Freeman, Natalie M. (Ph.D., Atmospheric and Oceanic Sciences)

Physical and biogeochemical features of the Southern Ocean: Their variability and change over the recent past and coming century

Thesis directed by Assistant Professor Nicole S. Lovenduski

While the Southern Ocean has experienced substantial changes in atmospheric forcing over the past few decades, the subsequent impacts on basin circulation and biogeochemical cycling is not well understood. Using satellite and hydrographic observations and model output, this dissertation investigates the variable and changing large-scale physical and biogeochemical features of the Southern Ocean. From 1998 to 2014, austral summer surface phytoplankton calcification and calcite concentration are found to decline by 9% and 24%, respectively, in large portions of the Southern Ocean's Great Calcite Belt, concurrent with a reduction in surface ocean carbonate ion concentration. A regional increase in biocalcification and calcite near the Antarctic Polar Front (PF) in the Atlantic sector is attributed to a physical southward shift in the location of the PF, altering local temperature and nutrient availability. Using methods that avoid cloud contamination and steric sea level change, a novel, comprehensive frontal mapping scheme was developed to create a high-resolution data set of weekly PF locations from 2002–2014. The spatio-temporal variability of the location and strength of the PF and its associated Silicate Front (SF) is largely influenced by the underlying bathymetry: over shallow bathymetry, Southern Ocean fronts are strong and interannual variability in position is low, while long-term meridional shifts in front position are found over the deeper regions of the Indian and Pacific sectors. From 2002 to 2014, the PF is found to have intensified both in zonal average and at nearly all longitudes; a more zonally asymmetric atmospheric circulation drives changes in wind forcing and, through modifications in SST, the strength of the PF. A state-of-the-art coupled climate model predicts a more poleward SF by the end of the 21st century under a high emission scenario, due to large-scale

reductions in surface silicate as a consequence of a warmer, more stratified Southern Ocean, with implications for local biology and the interpretation of paleoclimate records from deep sea sediments.

Dedication

To my best friend, my mother.

Acknowledgements

Chapters 2, 3, and 4 are versions of the following articles, respectively, and should be cited as follows:

Freeman, N. M. and N. S. Lovenduski, 2015: Decreased calcification in the Southern Ocean over the satellite record. *Geophysical Research Letters*, **42**, 1834–1840, doi:10.1002/2014GL062769.

Freeman, N. M. and N. S. Lovenduski, 2016: Mapping the Antarctic Polar Front: weekly realizations from 2002 to 2014. *Earth System Science Data*, **8**, 191–198, doi:10.5194/essd-8-191-2016.

Freeman, N. M., N. S. Lovenduski, and P. R. Gent, 2016: Temporal variability in the Antarctic Polar Front (2002–2014). *Journal of Geophysical Research: Oceans*, **121**, 7263–7276, doi:10.1002/2016JC012145.

This research was partially supported by the National Science Foundation under the Graduate Research Fellowship Grant DGE-1144083.

A number of people have contributed to my development as a scientist and the development of this work. I would like to give my most sincere, special thanks to:

- Professor Nikki Lovenduski for her incomparable example and for giving me that first 'Southern Ocean project' that set the past 5 years in motion; her confidence, support and encouragement afforded me opportunities to succeed and grow personally and professionally throughout my graduate career. My gratitude is boundless.
- The past and present members of the Ocean Biogeochemistry Research Group at CU Boulder for their friendship, support and sense of community.
- Dr. Peter Gent for his friendship and care, his kind and thoughtful guidance and his invaluable mentoring and sharing of wisdom.
- The SMART Program at CU Boulder for equipping me with the tools necessary to pursue and succeed in graduate school, and for the opportunity to pay my experience forward by serving as a mentor for the next generation of STEM scientists.
- Chad and Tara for their countless hours of assistance, for sharing in the frustrations and the laughter, and for their genuine care.

Contents

1 Introduction **1**
1.1 The Southern Ocean 1
1.2 Basin-scale, persistent physical and biogeochemical features 3
1.2.1 The Antarctic Polar Front 3
1.2.2 The Silicate Front 5
1.2.3 The Great Calcite Belt 6
1.3 Synopsis 7

2 Decreased calcification in the Southern Ocean over the satellite record **10**
2.1 Abstract 10
2.2 Introduction 11
2.3 Methods 12
2.4 Results and Discussion 14
2.5 Conclusions 20

3 Mapping the Antarctic Polar Front: weekly realizations from 2002 to 2014 **22**
3.1 Abstract 22
3.2 Introduction 23
3.3 Methods 25
3.3.1 Sea surface temperature observations 25
3.3.2 Mapping the Polar Front 26
3.4 Validating the Polar Front position 31
3.5 Results and Discussion 35
3.6 Conclusions 38
3.7 Polar Front data availability 38

4 Temporal variability in the Antarctic Polar Front (2002–2014) **40**
4.1 Abstract 40
4.2 Introduction 41
4.3 Data and Methods 44
4.3.1 Time-variable Polar Front properties 44
4.3.2 Wind speed and the surface westerly jet 45
4.3.3 Climate indices 46
4.4 Results 48
4.4.1 Seasonal variability 48

4.4.2 Interannual variability . . . 49
4.4.3 Long-term trends . . . 52
4.5 Discussion . . . 55
4.5.1 A changing Southern Ocean . . . 55
4.5.2 Topographic influence on the Polar Front . . . 57
4.5.3 Role of wind . . . 57
4.5.4 Climate variability impacts . . . 61
4.5.5 Widespread frontal intensification . . . 61
4.5.6 The Polar Front on glacial-interglacial timescales . . . 63
4.6 Conclusions . . . 64

5 Present and projected variability of the Southern Ocean Silicate Front: Insights from the CESM Large Ensemble 66
5.1 Abstract . . . 66
5.2 Introduction . . . 67
5.3 Data and Methods . . . 70
5.3.1 Model description . . . 70
5.3.2 Observations . . . 72
5.4 Results . . . 73
5.4.1 Mean state . . . 73
5.4.2 Seasonal variability . . . 73
5.4.3 Interannual to interdecadal variability . . . 76
5.4.4 Long-term change . . . 77
5.5 Discussion . . . 79
5.5.1 A more poleward SF: Mechanisms and implications . . . 80
5.5.2 Observational and intermodel comparison . . . 84
5.5.3 Study limitations . . . 86
5.6 Conclusions . . . 87

6 Summary and Conclusions 89

A Supplementary Material for Chapter 2 111

List of Tables

2.1 What drives calcification trends (1998–2014)? 16

3.1 Estimated Polar Front location RMS error 33

4.1 Mean values and regression and correlation coefficients of the mean Polar Front time series with the SAM and ENSO index 49

A.1 Carbonate analyses data information table 113

List of Figures

1.1 The physical and biogeochemical state of the Southern Ocean 2
1.2 Schematic of Southern Ocean circulation 4
1.3 Apparent frontal-biogeochemical relationship in Drake Passage 7

2.1 Calcification and PIC: Mean state and trends 15
2.2 Basin-mean calcification: Multi-decadal trends 17
2.3 Concurrent changes in carbonate ion concentration 18

3.1 Example of spatial and thermal discontinuity 27
3.2 When is spatial and thermal discontinuity justified? 29
3.3 Polar Front location validation using XBT data 30
3.4 Southern Ocean mean SST, SST gradients, and Polar Front location 32
3.5 Climatological characteristics of the Polar Front 34
3.6 How does this study compare to previous studies? 37

4.1 Influence of bathymetry on Polar Front position and variability 42
4.2 Does the Polar Front exhibit a seasonal cycle? 47
4.3 Polar Front location, by season 50
4.4 Time series of monthly, zonal mean Polar Front location and intensity 53
4.5 Monthly, zonal mean Polar Front location and intensity: Multi-decadal trends 56
4.6 Total change in Polar Front location and intensity (2002–2014) 58
4.7 What drives frontal intensification (2002–2014)? 60

5.1 Coincidence between observed and modeled frontal features 68
5.2 Silicate-to-nitrate ratio: Mean state 74
5.3 Does the Silicate Front exhibit a seasonal cycle? 75
5.4 Influence of bathymetry on interdecadal variability in the Silicate Front . . . 77
5.5 The Silicate Front shifts poleward during the 21st century 78
5.6 Why does the Silicate Front shift south? 80
5.7 What drives long-term decreases in surface nutrients? 82
5.8 Intermodel comparison: present-day surface silicate concentration 85

A.1 Chlorophyll-a and SST: Mean state and trends 112
A.2 Continuous satellite time series: An example 114
A.3 Regional calcification: Multi-decadal trends 115
A.4 What if satellite algorithms are over-/underestimating PIC or chlorophyll-a? 116
A.5 The Polar Front shifts poleward in Region 4 117

Vita

August 20, 1990 Born, Kansas City, Kansas

2012 B.S., Mathematics, University of Kansas

2014 M.S., Atmospheric and Oceanic Sciences, University of Colorado

Publications

Munro, D. R., N. S. Lovenduski, B. B. Stephens, T. Newberger, K. R. Arrigo, T. Takahashi, P. D. Quay, J. Sprintall, **N. M. Freeman**, and C. Sweeney, 2015: Estimates of net community production in the Southern Ocean determined from time series observations (2002–2011) of nutrients, dissolved inorganic carbon, and surface ocean pCO_2 in Drake Passage, *Deep-Sea Research II*, 114, 49–63, doi:10.1016/j.dsr2.2014.12.014.

Freeman, N. M. and N. S. Lovenduski, 2015: Decreased calcification in the Southern Ocean over the satellite record. *Geophysical Research Letters*, 42, 1834–1840, doi:10.1002/2014GL062769.

Krumhardt, K. M., N. S. Lovenduski, **N. M. Freeman**, and N. R. Bates, 2016: Apparent increase in coccolithophore abundance in the subtropical North Atlantic from 1990 to 2014. *Biogeosciences*, 13, 1163–1177, doi:10.5194/bg-13-1163-2016.

Freeman, N. M. and N. S. Lovenduski, 2016: Mapping the Antarctic Polar Front: weekly realizations from 2002 to 2014. *Earth System Science Data*, 8, 191–198, doi:10.5194/essd-8-191-2016.

Freeman, N. M. and N. S. Lovenduski, 2016: Mapping the Antarctic Polar Front: Weekly realizations from 2002 to 2014. *Supplement to: Earth Syst. Sci. Data*, 8, 191–198, doi:10.1594/PANGAEA.855640.

Freeman, N. M., N. S. Lovenduski, and P. R. Gent, 2016: Temporal variability in the Antarctic Polar Front (2002–2014). *Journal of Geophysical Research: Oceans*, 121, 7263–7276, doi:10.1002/2016JC012145.

Chapter 1

Introduction

1.1 The Southern Ocean

The Southern Ocean is a fundamental player in and moderator of the global climate system, owing to its unique physical and biogeochemical oceanography. While only making up ∼20% of the total ocean area, the Southern Ocean accounts for nearly three quarters of the oceanic uptake of excess heat and nearly half the oceanic uptake of excess carbon dioxide (Figure 1.1), acting to suppress the rate of anthropogenic climate change (*Sabine et al.*, 2004; *Mikaloff Fletcher et al.*, 2006; *Khatiwala et al.*, 2009; *Frölicher et al.*, 2014). This vast ocean is largely characterized by the Antarctic Circumpolar Current (ACC; Figure 1.2; Section 1.2.1), the world's largest current driven by the world's strongest sustained band of winds; as such, the Southern Ocean has been affectionately regarded as *hostile, mysterious, and extreme* by those who have experienced its remote waters. The ACC is the conduit by which the Southern Ocean interacts with and imprints on the rest of the World Ocean: by providing the southern link to the global thermohaline circulation, regulating uptake of anthropogenic carbon (Figure 1.1) and heat, allowing inter-basin exchange of key climate variables, and creating a unique macronutrient-rich environment (Figure 1.1) that fuels the majority of the biological production to its north (*Banks et al.*, 2000; *Rintoul et al.*, 2001;

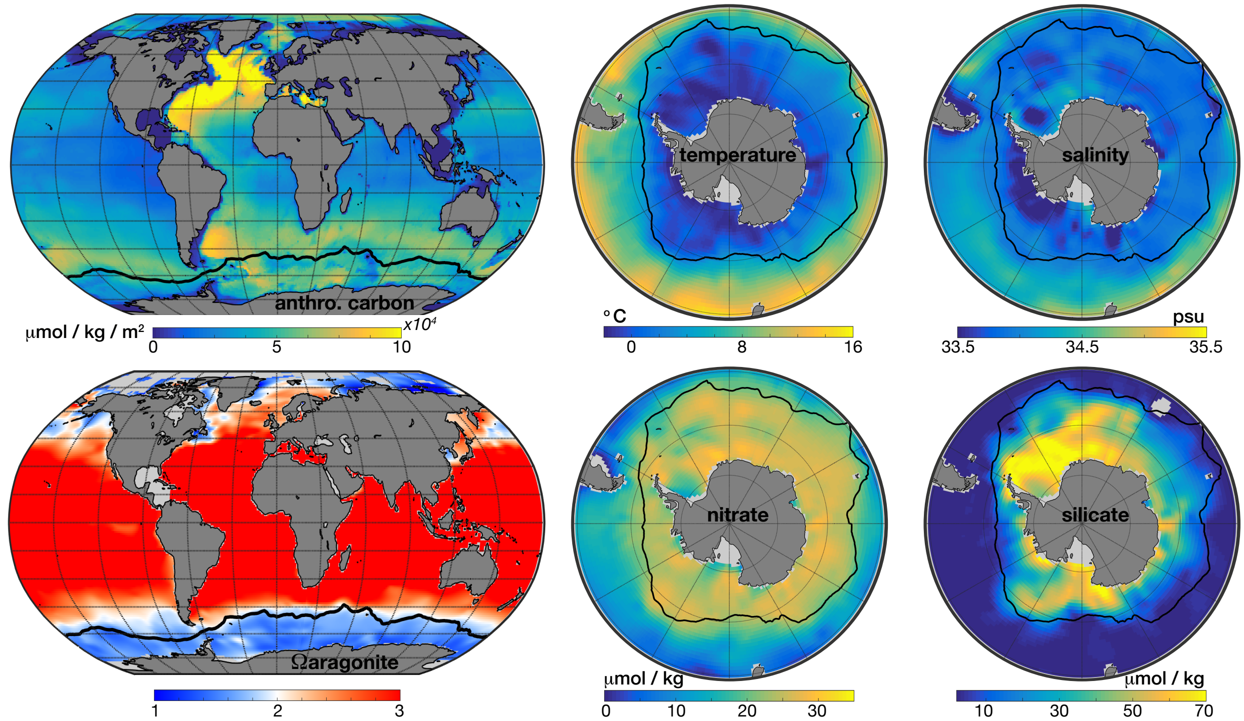

Figure 1.1: Global maps of the climatological mean (top) anthropogenic carbon (vertically-integrated) inventory and (bottom) aragonite saturation state ($\Omega = 1$ indicates favorable conditions for dissolution of aragonite shells). Stereographic maps of climatological mean *surface* temperature, salinity, nitrate, and silicate south of 44°S. Climatological data from GLODAP (version 2; *Key et al.*, 2015; *Olsen et al.*, 2016; *Lauvset et al.*, 2016); the black contour in each map indicates the mean position of the Antarctic Polar Front, an important physical and biogeochemical front, described in Chapter 3 (2002–2014; *Freeman and Lovenduski*, 2016a).

Sarmiento et al., 2004; *Marinov et al.*, 2006).

The large-scale view of the lateral and overturning circulation of the Southern Ocean (i.e., the "southern link") is depicted schematically in Figure 1.2. The strong westerly winds (i.e., westerlies) are partially responsible for driving the eastward, geostrophic flow of the ACC while the land opening through the Drake passage allows for this flow to be zonally unbounded around Antarctica, making the Southern Ocean the only place on Earth where waters circle the globe. The westerly winds also drive northward Ekman transport in surface layers, which in turn acts to drive an ageostrophic meridional overturning circulation (MOC), fundamental to heat and carbon exchange with the atmosphere. Indeed, a hallmark of the Southern Ocean is its significant upwelling, as one of the only locations on Earth where deep, ancient waters (~1–2 km deep, $\mathcal{O}(100)$ years old; e.g., North Atlantic Deep Water) upwell to the surface, allowing for the formation of new water masses that sink back into the global ocean interior (e.g., Subantarctic Mode Water, Antarctic Intermediate Water; *Rintoul et al.*, 2001). Southern Ocean biogeochemical cycling is inherently linked through this unique circulation: the upwelled water is rich in macronutrients (Figure 1.1) and carbon and while at the surface, has the opportunity to interact with the atmosphere, exchanging heat and carbon (Lumpkin and Speer, 2007) and fueling biological productivity.

The Southern Ocean is considered one of the major high nutrient, low chlorophyll (HNLC) regions (Minas and Minas, 1992) owing to its abundance of macronutrients (nitrate, phosphate, silicate; see Figure 1.1) and its persistent lack of the micronutrient iron (*Boyd et al.*, 1999, 2007). Of the dominant marine phytoplankton found here, coccolithophores (e.g., *Emiliania huxelyi*; see illustration in Figure 1.3) are calcifying phytoplankton that secrete shells out of calcium carbonate ($CaCO_3$) and diatoms are larger, silicifying phytoplankton that build their shells out of silica (i.e., opal). The overall productivity and biogeography of these and other algal groups is largely determined by local physical and biogeochemical factors (e.g., *Dugdale and MacIsacc*, 1971; *Egge and Aksnes*, 1992; *Aksnes et al.*, 1994) influencing bottom-up (e.g., nutrient supply) and top-down controls (e.g., zooplankton grazing).

1.2 Basin-scale, persistent physical and biogeochemical features

1.2.1 The Antarctic Polar Front

As light surface waters are pushed equatorward through Ekman transport, mass balance requires that water must upwell from below, traveling along isopycnals from depth to the surface; these sloping density layers tilt poleward toward the surface in order to compensate for the resulting elevated sea surface height to the north, and in doing so, set up the

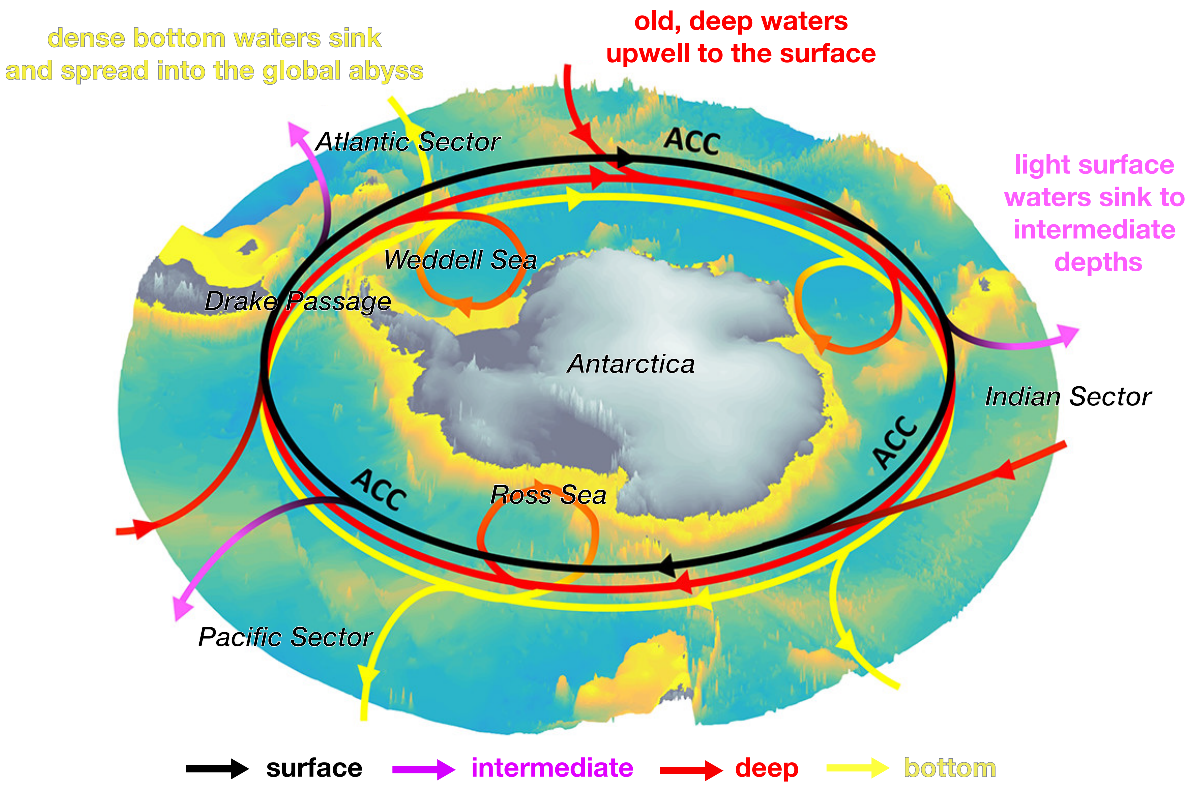

Figure 1.2: Schematic of the surface-to-deep circulation of the Southern Ocean (colored arrows) overlain on the underlying bathymetry, where warm colors indicate shallow bottom depths, and cool colors deep. Adapted from *Meredith* (2016).

many hydrographic fronts (i.e., water mass boundaries) and geostrophic jets (i.e., currents of transport) of the ACC. More than any other region, the Southern Ocean has been defined by its many fronts. Traditionally, from north to south, the fronts of the ACC are the Subantarctic Front, Antarctic Polar Front (PF; see black contour in Figure 1.1), and Southern ACC Front, each characterized by sharp, lateral property gradients (e.g., temperature, salinity) and separating more or less uniform physical and biogeochemical regimes (see Figure 1.1; *Deacon*, 1982; *Pollard et al.*, 2002). For example, waters making up the Antarctic Zone to the south of the PF exhibit a fresh surface signature, shallow mixed layer depths in summer, and high (low) concentrations of macronutrients (micronutrients) as a result of upwelling deep water and local sea ice variability (see Figure 1.1). Therefore, the location of ACC fronts has implications for local physics and biogeochemistry; local shifts in location could lead to changes in basin-scale biological productivity and heat, freshwater, and carbon content, including their fluxes at the air-sea interface.

Recent work on the PF has relied heavily on remote sensing platforms to investigate its large-scale variability on interannual to interdecadal timescales (see Chapter 3), with particular interest stemming from an observed strengthening and poleward shift in the driving westerlies (*Thompson et al.*, 2000; *Thompson and Wallace*, 2001; *Marshall*, 2003; *Thompson et al.*, 2011). Despite a greater understanding of how the location and strength of the PF is influenced by the underlying bathymetry, methodological differences in identifying the PF has led to competing views on long-term change. However, increasingly diverse evidence suggests that the PF has not shifted substantially in response to atmospheric forcing in recent decades (e.g., see Chapter 4).

1.2.2 The Silicate Front

The presence of diatoms are responsible for the Southern Ocean's Silicate Front (SF) at the surface and the vast Opal Belt of siliceous sediments that ring the continent. As silicic acid-rich waters upwell to the south of the PF and are pushed equatorward through Ekman transport, diatoms utilize the available silicate to build their frustules; any unused portion is subducted as mode or intermediate water to the north or exported to the abyss (*Sarmiento et al.*, 2007; *Tréguer*, 2014). This bio-physical mechanism sets up the sharp meridional gradient in silicate observed at the PF (Figure 1.1; see Chapter 5).

Despite the region's HNLC status, the silicic acid-rich surface waters of the Southern Ocean support high diatom presence and subsequent biogenic silica (i.e., opal) production. Indeed, the Southern Ocean is one of the most important silica sinks of the World Ocean (*Pondaven et al.*, 2000; *DeMaster*, 2002). The fraction of the opal that arrives at and is buried in the sediments makes up the Opal Belt. Through decades of sediment coring, this PF/SF-sediment relationship has been used to reconstruct the paleo position of the PF and infer changes in diatom productivity and atmospheric carbon dioxide concentrations on glacial-interglacial timescales (*DeMaster*, 1981, 2002; *Anderson et al.*, 2009; *Kemp et al.*, 2010; *Ho et al.*, 2012; *De Deckker et al.*, 2012; *Kohfeld et al.*, 2013). Knowing the paleo position of the PF is therefore important for our understanding, interpretation, and modeling of these long climatic timescales.

1.2.3 The Great Calcite Belt

The presence of coccolithophores are responsible for the Southern Ocean's Great Calcite Belt (GCB), a seasonally persistent feature of elevated surface reflectance between ∼38–60°S (∼52 x 10^6 km^2 in total area) throughout the productive austral summer months (*Holligan et al.*, 2010; *Balch et al.*, 2011, 2014; *Rembauville et al.*, 2016; *Balch et al.*, 2016). The GCB as a large-scale feature was first realized with the first global composites of remotely-sensed particulate inorganic carbon (PIC) concentrations in the late 1990s. Satellite estimates suggest that ∼26% of the global PIC standing stock is found here (*Balch et al.*, 2005) and nearly five decades of shipboard observations support the existence of the GCB's coccolithophore-rich waters (see *Holligan et al.*, 2010). In particular, satellites reveal that elevated chlorophyll-a and/or PIC concentrations are often found near ACC fronts (*Moore and Abbott*, 2002; *Balch et al.*, 2016) while shipboard observations further support a coupling between distinct phytoplankton communities and frontal zones (*Balch et al.*, 2016). For example, Figure 1.3 demonstrates the co-location of coccolithophores and the PF across the Drake Passage and Scotia Sea: north of the PF, surface waters are rich in coccolithophore PIC, while south of the PF, waters are devoid of PIC. The reader is encouraged to see the conceptual model proposed by *Balch et al.* (2016) outlining the growth and competition of coccolithophores and diatoms in the Southern Ocean in relation to the location of the PF and iron availability.

While the Southern Ocean is the primary conduit for man-made carbon entering the ocean, the direct result is ocean acidification (OA) through lowered seawater pH and $CaCO_3$ saturation state (Figure 1.1). OA is a current and real threat to coccolithophores and other calcifying organisms and thus the biodiversity and structure of ecosystems (*Doney et al.*, 2009; *Feely et al.*, 2009). Owing to the Southern Ocean's naturally low carbonate saturation state ($\Omega_{aragonite}$ in Figure 1.1), it is one of the key areas of the World Ocean expected to feel

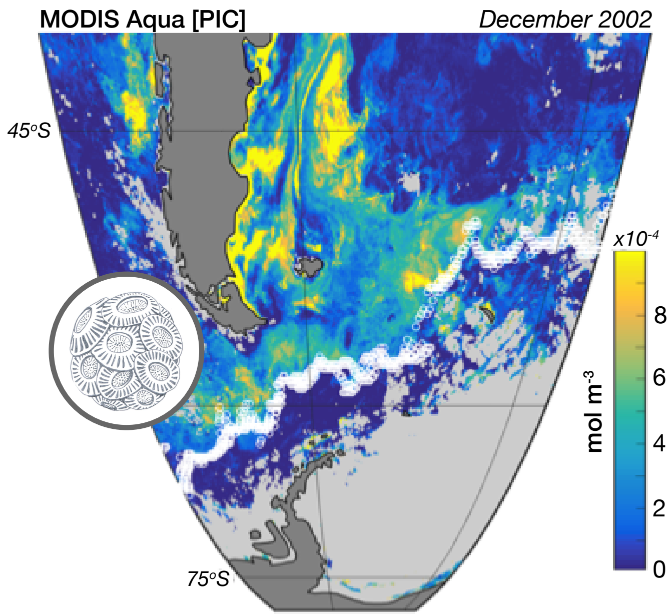

Figure 1.3: December 2002 composite of MODIS Aqua-derived PIC (colors; *Gordon et al.*, 2001; *Balch et al.*, 2005); warm colors indicate high concentrations of suspended calcite, and cool colors, low. Satellite-estimated PIC is a qualitative proxy for the presence of *E. huxleyi* (subset: illustration by Kristen M. Krumhardt, University of Colorado Boulder). White open circles indicate weekly positions of the PF during the month of December 2002 (*Freeman and Lovenduski*, 2016b).

the impacts of OA first; therefore, monitoring and tracking large-scale changes in PIC from remote-sensing platforms is crucial (see Chapter 2).

1.3 Synopsis

While the strong, zonal flow of the ACC combined with the MOC largely determines the Southern Ocean's role in the global climate system, it also demonstrates the region's potential sensitivity to future climate change (*Sarmiento et al.*, 1998; *Murnane et al.*, 1999; *Broecker et al.*, 1999; *Gordon et al.*, 2001; *Karsten and Marshall*, 2002; *Sarmiento et al.*, 2004; *Mikaloff Fletcher et al.*, 2006, 2007). The Southern Ocean has experienced significant changes in atmospheric forcing, heat, freshwater and carbon in recent decades (*Thompson et al.*, 2000; *Thompson and Wallace*, 2001; *Gille*, 2002; *Marshall*, 2003; *Böning et al.*, 2008; *Gille*, 2008; *Rignot et al.*, 2008; *Cai et al.*, 2010; *Thompson et al.*, 2011; *Landschützer et al.*, 2015; *Munro et al.*, 2015a; *Hogg et al.*, 2015) and is projected to undergo continued and additional change in the coming century (e.g., *Fyfe and Saenko*, 2006; *Thompson et al.*, 2011; *Swart and Fyfe*, 2012; *Meijers*, 2014). The Southern Ocean is historically under-sampled, but the onset of varied, yet complimentary observational platforms in recent decades has improved our spatio-temporal understanding of this important region in recent decades (see Chapter 6). Sustained observations of the Southern Ocean are crucial, not only for the ability to detect change but to improve our mechanistic understanding of the key physical, chemical, and biological processes occurring here, and therefore modeling capabilities and predictive skill.

This chapter motivates the global significance of the Southern Ocean and introduces its characterizing large-scale, persistent physical and biogeochemical features. The remaining chapters describe various novel works focused on improving our understanding of these large-scale features from an observational and modeling perspective. Chapter 2 provides a first estimate of changing biocalcification and PIC within the Great Calcite Belt (Section 1.2.3), possibly a result of ocean acidification, and motivates how frontal variability can impact local biogeography. These results have gained attention in both the scientific community and the general public, through social networking and outlets such as The New York Times (*Bhanoo*, 2015) and Nature Climate Change Research Highlights (*Wake*, 2015). Chapter 3 is largely methodological, discussing the formulation of an improved PF (Section 1.2.1) mapping technique and the algorithm and data used to carry it out. In the context of the current, albeit controversial, literature on frontal identification methodologies and long-term change in ACC fronts, Chapter 4 uses this mapping technique and resulting PF location data set to describe the spatio-temporal variability of the PF (its location and strength) over the observed microwave satellite record (2002–2014). Given the lack of time-varying silicate observations in the Southern Ocean, Chapter 5 uses model output to provide a first estimate of the spatio-temporal variability of the SF (Section 1.2.2) and thoroughly describes the varied implications for projected long-term displacements. Chapter 6 summarizes the results and conclusions of this dissertation, which represent significant progress in the study of physical and biogeochemical oceanography in the Southern Ocean, and provides suggestions for future work.

Chapter 2

Decreased calcification in the Southern Ocean over the satellite record

2.1 Abstract

Widespread ocean acidification is occurring as the ocean absorbs anthropogenic carbon dioxide from the atmosphere, threatening marine ecosystems, particularly the calcifying plankton that provide the base of the marine food chain and play a key role within the global carbon cycle. We use satellite estimates of particulate inorganic carbon (PIC), surface chlorophyll, and sea surface temperature to provide a first estimate of changing calcification rates throughout the Southern Ocean. From 1998 to 2014 we observe a 4% basin-wide reduction in summer calcification, with ~9% reductions in large regions (~1x10^6 km^2) of the Pacific and Indian sectors. Southern Ocean trends are spatially heterogeneous and primarily driven by changes in PIC concentration (suspended calcite), which has declined by ~24% in these regions. The observed decline in Southern Ocean calcification and PIC is suggestive of large-scale changes in the carbon cycle and provides insight into organism vulnerability in a changing environment.

2.2 Introduction

The dissolution of carbon dioxide (CO_2) in seawater alters carbonate chemistry by lowering pH and reducing the carbonate ion concentration [$CO_3{}^{2-}$]. A reduction in [$CO_3{}^{2-}$] lowers the saturation state of seawater with respect to calcite and aragonite, the two forms of mineral calcium carbonate ($CaCO_3$). Coccolithophores are calcifying phytoplankton that play a key role in the biological pump; they secrete calcite shells that act as ballast, helping to export carbon from the surface to the deep. As more of the water column becomes undersaturated in the future (*Fabry et al.*, 2009), dissolution of $CaCO_3$ will be favored over precipitation and coccolithophores may be less successful in exporting carbon to the deep (*Fabry et al.*, 2008). Many previous calcification-CO_2 response studies investigating potential impacts of ocean acidification (OA) suggest that elevated CO_2 reduces organism calcification (*Riebesell et al.*, 2000; *Langer et al.*, 2009; *Zondervan et al.*, 2001; *Delille et al.*, 2005; *Engel et al.*, 2005).

The Southern Ocean (>30°S) absorbs a large fraction of anthropogenic carbon dioxide emissions from the atmosphere (*Sabine et al.*, 2004; *Khatiwala et al.*, 2009). As a region characterized by low levels of [$CO_3{}^{2-}$] and a shallow $CaCO_3$ saturation horizon (*Feely et al.*, 2009), we are likely to detect the impacts of OA here earlier than elsewhere in the global ocean (*Fabry et al.*, 2009). High concentrations of coccolithophore particulate inorganic carbon (PIC) extend from the Antarctic continent northward to ~30^{o}S during austral summer, a characteristic detectable from space and referred to as the Great Calcite Belt (*Balch et al.*, 2011). While some studies attribute elevated concentrations of satellite-estimated PIC here to other scattering sources, such as microbubbles (*Zhang et al.*, 2002) or non-calcifying organisms in the Ross Sea (e.g., *Phaeocystis antarctica*; *Arrigo et al.*, 1999), many studies support high coccolithophore abundance in the Great Calcite Belt (*Painter et al.*, 2010; *Balch et al.*, 2011, 2014; *Sadeghi et al.*, 2012). The Patagonian Shelf, the highest reflectance region within the Belt, is also a highly productive region (Figure A.1a) due to upwelling, mixing, tides, and riverine input and home to large coccolithophore blooms in summer (*Painter et al.*, 2010; *Balch et al.*, 2014). High calcification rates have been estimated within these high-PIC regions (*Balch et al.*, 2007), but changes in these rates have not yet been quantified. Here, we present a first estimate of changing calcification rates within the Southern Ocean over the satellite record.

2.3 Methods

This study focuses on austral summer (DJF) calcification south of 30°S from 1998 to 2014. We used satellite observations of monthly-binned PIC, chlorophyll concentration, and sea surface temperature (SST) to calculate calcification rates (C) using Equation 1 of *Balch et al.* (2007):

$$\begin{aligned} C &= 0.2694^{-1}[(-0.0063Z + 0.05081PIC \\ &\quad -0.01055CHL + 0.05806D - 0.0079SST) - 0.4008], \end{aligned} \tag{2.1}$$

where depth (Z) is 1 m and daylength (D; hours) is calculated for the 15th day of each month as a function of latitude; Sea-viewing Wide Field-of-view Sensor (SeaWiFS) Level 3 PIC and chlorophyll (1997–2009) and Advanced Very High Resolution Radiometer (AVHRR) Oceans Pathfinder SST (1997–2009) and Moderate Resolution Imaging Spectroradiometer (MODIS)-Aqua PIC, chlorophyll and SST (2002–2014; both day and night temperature retrievals were equally weighted to maximize data availability) on a 9 km grid. December, January, and February calcification rates of each year were averaged to form a mean summer calcification rate (90-day temporal bins; e.g., December 2002 and January and February 2003 represent *summer 2003*, etc.). The RMS error in calcification rate (RMS = ±0.021 mg PIC m^{-3} day^{-1}) was derived using the $n^{-0.5}$ technique described in *Balch et al.* (2007). Since the RMS error is an order of magnitude smaller than the uncertainty in the trend estimates, we report 95% confidence estimates. One continuous record of calcification from 1998 to 2014 was generated at each Southern Ocean location following the regression technique of *Brown and Arrigo* (2012): we applied linear regression over the 2003-2007 SeaWiFS/MODIS overlap period in order to predict calcification from summer 2008 to 2014 (Figure A.2), excluding 2008-2009 for which limited SeaWiFS data are available.

Calcification rate, PIC, chlorophyll, and SST data were corrected for the presence of summer sea ice. We re-gridded monthly (1998–2012), 25 km sea ice concentrations from Nimbus-7 SSMR and DMSP SSM/I-SSMIS Passive Microwave Data (*Cavalieri et al.*, 1996, updated yearly) to a 9 km grid, using climatological sea ice concentration for missing data points. These data were masked where at least 40 (out of 48) months included some percentage of ice.

Percent changes reported here were determined by (1) calculating the area-weighted mean of a particular location (entire basin or specific region) to create a time series of summers 1998 to 2014, (2) performing linear regression on the time series (in a least-squares sense) to find the slope of the fitted line, and (3) multiplying that slope by the length of the time series and dividing by the arithmetic mean of the time series. Basin-wide calculations exclude locations where the summer mean is missing at least one month of data.

Carbonate ion concentrations were estimated using the program developed for CO_2 system calculations (CO2SYS; *Lewis and Wallace*, 1998), with the preferred dissociation constants (*Takahashi et al.*, 1982; *Dickson*, 1990; *Uppstrom*, 1979). Significant trends, in a least-squares sense, were found if 3 or more summer data points existed in the time series at each location. The variables used in the program for the surface (depth) analysis include fCO_2 and pCO_2 (total CO_2 concentration), alkalinity, silicate and phosphate concentration, salinity, SST (temperature), and pressure (see Table A.1).

To calculate a change in calcification due to a change in a particular satellite variable, for example PIC, we find the equation of the line that best fits PIC in a least-squares sense. Using the calcification algorithm (*Balch et al.*, 2007), the mean calcification rate at time 1 (C_i; year 1998) is calculated as in equation 1, where PIC is the fitted 1998 value. We calculate the estimated final mean rate at time 17 (C_f; year 2014) as in equation 1, where PIC is the fitted 2014 value and chlorophyll and SST are held constant at their initial fitted

1998 values. The difference in C_i and C_f is the resulting estimated change in calcification rate due to the change in PIC concentration for a given region.

The location of the Antarctic Polar Front was found using weekly satellite-estimated (AMSR-E) sea surface temperature (*Dong et al.*, 2006a) from 2002–2011, and defined as the absolute SST gradient at each grid point: $[(dT/dx)^2 + (dT/dy)^2]^{1/2}$. Large gradients found near Antarctica were removed. At each longitude, the position is the southernmost location where the SST gradient exceeded 1.5°C per 100 km. Small patches of high SST gradients spanning less than 4 degrees longitude were removed (possible eddy/ring detection) and relaxations of the SST gradient limit were made for large deviations from the temporal mean. See *Dong et al.* (2006a) for further detail.

2.4 Results and Discussion

Figure 2.1a shows the mean rate of summer calcification. We observe a basin-wide average of 2.28 $\pm$ 0.021 mg PIC m^{-3} day^{-1}, with values lowest in the subtropics and highest south of the Antarctic Polar Front (PF; Figure 2.1a). In agreement with previous studies (*Balch et al.*, 2007; *Beaufort et al.*, 2011), we find elevated calcification rates near the Patagonian Shelf and in the vicinity of the Antarctic Circumpolar Current (ACC). Suspended calcite in the Southern Ocean exists at an average concentration of $\sim$4.65 mg m^{-3}. A sharp decrease in PIC south of the PF is observed in the Bellingshausen and Amundsen sector (Figure 2.1c), in agreement with the same gradient reported for coccolithophore abundance in this region (*Gravalosa et al.*, 2008). We assess the sensitivity of basin-scale calcification rate trends to interannual variability by calculating trends for a range of start and end years. The sign of the trends are robust across many start and end year pairs (Figure 2.2b), suggesting that long-term trends in Southern Ocean calcification are independent of interannual variability.

From 1998 to 2014 we observe a 3.9 $\pm$ 1.3% basin-wide reduction in summer calcification (Figure 2.2a). Throughout the Southern Ocean, significant trends (at the 95% level) in

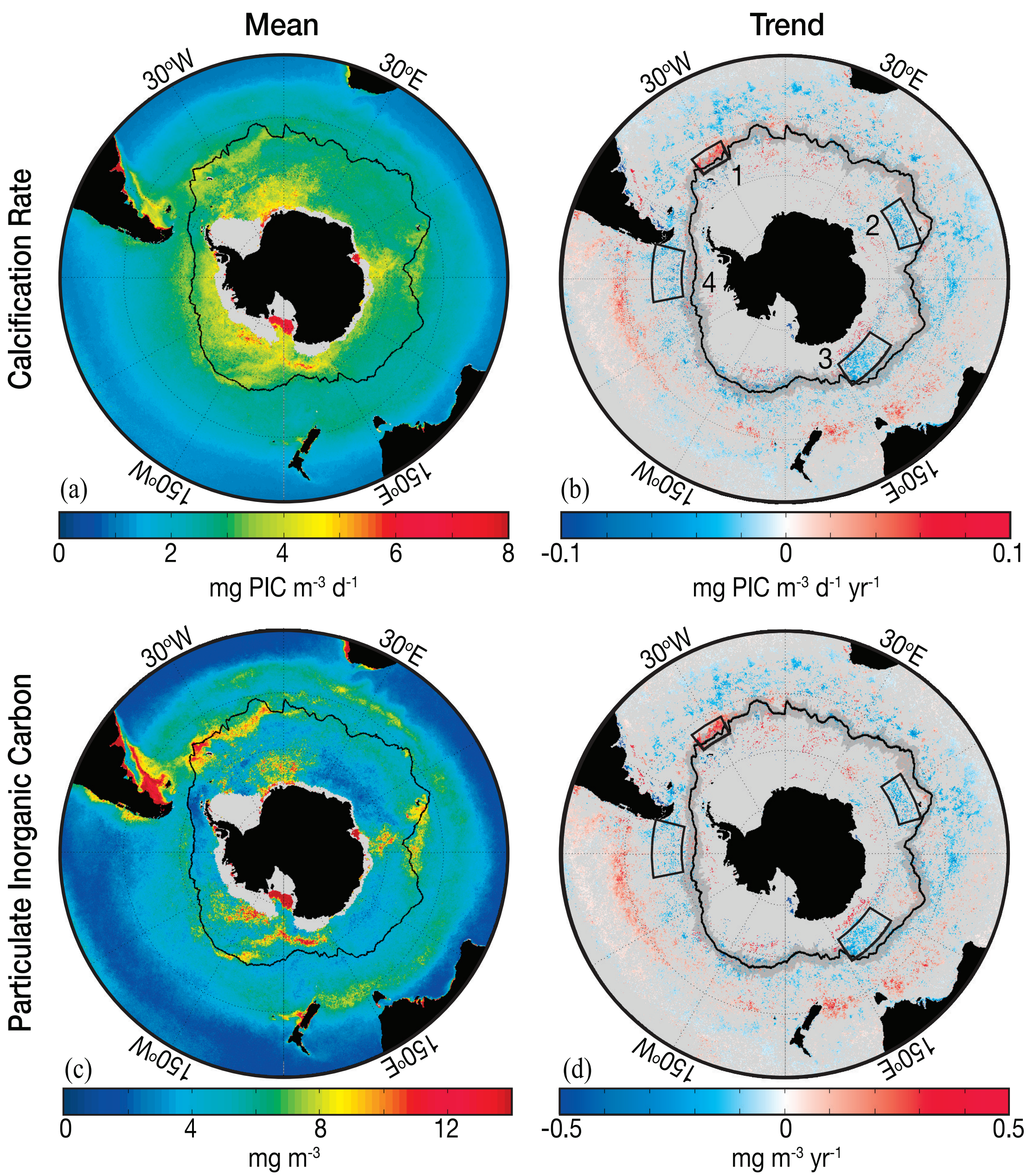

Figure 2.1: Maps of Southern Ocean (>30°S) summer (DJF) mean state of (a) calcification rate and (c) particulate inorganic carbon concentration and linear trends in (b) calcification and (d) PIC, masked for the presence of summer sea ice (see Section 2.3). Only those trends with significance ≥95% are shown. The black line and gray shading indicate the average summer location of the Antarctic Polar Front (see Section 2.3). Boxes indicate regions singled out for further analysis in the (1) Atlantic, (2) western Indian, (3) eastern Indian, and (4) Pacific sectors.

Table 2.1: What drives calcification trends (1998–2014)?

	Region 1	Region 2	Region 3	Region 4
	Mean calcification rate, mg PIC m^{-3} d^{-1}			
	3.193	2.938	2.758	2.775
	Changes in calcification, mg PIC m^{-3} d^{-1}			
[a]*Total change*	0.457±0.164	-0.269±0.127	-0.321±0.086	-0.207±0.086
[b]*PIC contribution*	0.483	-0.227	-0.271	-0.155
[b]*Chl contribution*	-0.007	0.002	0.002	0.001[c]
[b]*SST contribution*	-0.009[c]	-0.008[c]	-0.017[c]	-0.002[c]
	Mean PIC, mg m^{-3}			
	8.169	5.967	4.179	4.893
	[a]***Changes in PIC, mg m^{-3}***			
	2.560±0.909	-1.201±0.648	-1.434±0.452	-0.823±0.425

[a] 95% confidence interval reported for total change.
[b] Sum of contributions ≠ total change values exactly (see Section 2.3).
[c] Trends used in calculation not statistically significant at ≥95% level.

both calcification and PIC are spatially heterogeneous yet negative nearly everywhere in the Atlantic, Indian, and southern-most Pacific sectors (Figure 2.1b,d). Patches of positive trends are found near the PF in the Atlantic sector and near the Subtropical Front in the Pacific sector. We identify four large regions (~1x10^6 km^2) with significant trends located in the ACC region for further analysis (Figure 2.1b). Region 1 in the Atlantic shows a 14.3% (31.3%) increase in calcification rate (PIC concentration) over 1998 to 2014, while regions 2, 3, and 4 in the Indian and Pacific sectors have experienced a 9.2% (20.1%), 11.6% (34.3%), and 7.5% (16.8%) decline over this period, respectively (Table 2.1). We assess the sensitivity of regional calcification rate and PIC trends to interannual variability as above. Again, the sign of the trends are robust across many start and end year pairs (Figure A.3), suggesting that long-term trends are independent of interannual variability in these regions. Maps of the mean state and trends of chlorophyll and sea surface temperature are shown in Figure A.1.

In order to better understand the role of PIC, chlorophyll, and SST in driving calcification trends, we calculate the contribution of each of these quantities to the total change in calcification rate from 1998 to 2014 in each region (see Section 2.3). Table 2.1 shows the total change in calcification rate by region and the contribution to the total change from the

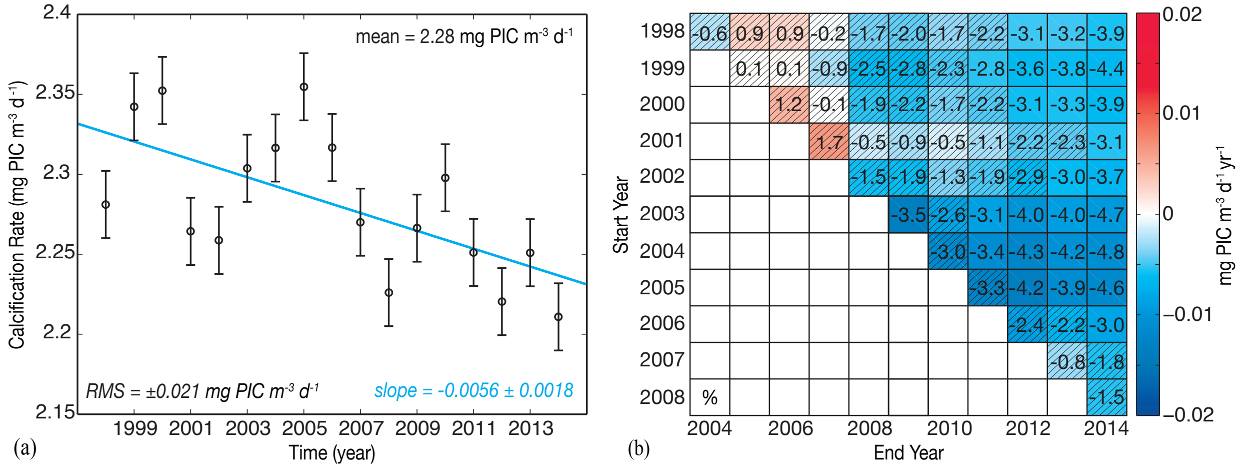

Figure 2.2: (a) Time series of basin area-weighted mean calcification rate from summers 1998 to 2014. Error bars (black) showing expected standard error (with respect to Equation 1; see Methods) and fitted least-squares line (cyan) provided. (b) Multi-decadal trends in basin-mean calcification rate over the same time period. Colorbar indicates the slope of the fitted trend line (in units of mg PIC m^{-3} day^{-1} $year^{-1}$) for each start and end year pair and text shows the percent change in calcification rate with respect to the mean. Trends that are not significant at the 95% level are hatched.

change in PIC, chlorophyll, and SST over this period; it is clear that the PIC contribution is largest. We conclude that the calcification trends in these regions are primarily driven by changes in PIC concentration.

We investigate the drivers of heterogeneity in Southern Ocean calcification trends by quantifying trends in surface ocean carbonate ion concentration from hydrography data. While the calcification-CO_2 response is not completely understood (*Riebesell et al.*, 2000; *Beaufort et al.*, 2011; *Iglesias-Rodriguez et al.*, 2008; *Beaufort et al.*, 2008), we generally expect areas exhibiting negative trends in $[CO_3{}^{2-}]$ to correspond to areas with decreases in calcification over the satellite period. We used underway surface water fugacity of CO_2 (fCO_2) and partial pressure of CO_2 (pCO_2) measurements, together with a combination of concurrent measurements and climatologies of temperature, salinity, alkalinity, silicate and phosphate to estimate the surface ocean carbonate ion concentration and its change over time (see Table A.1; *Lewis and Wallace*, 1998). The sign of the trends in surface carbonate (Figure 2.3a) track the sign of the trends in calcification (Figure 2.1b) and PIC (Figure 2.1d),

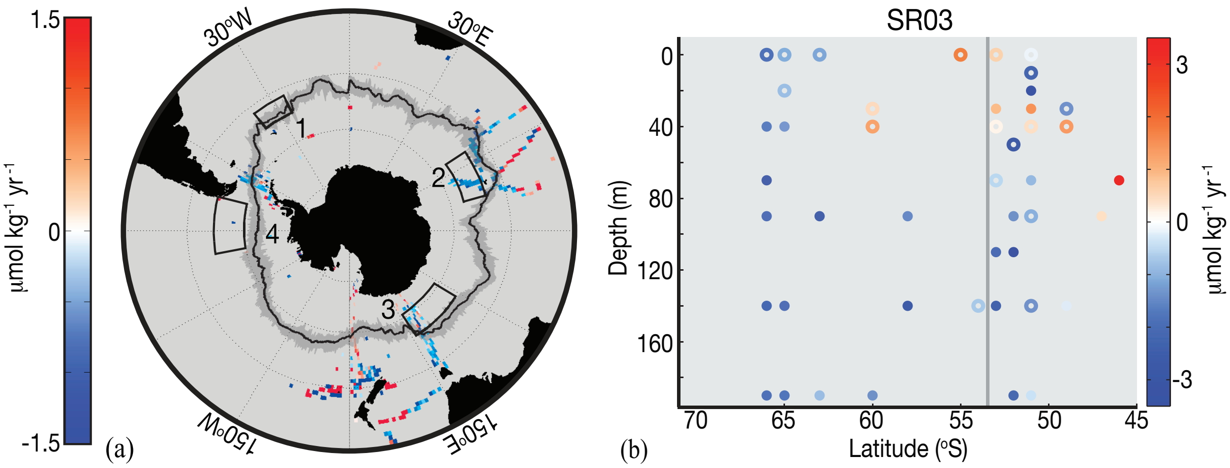

Figure 2.3: (a) Significant trends (at the 95% level) in summer surface carbonate from continuous underway fCO_2 (1998–2011; *Sabine et al.*, 2013) and pCO_2 (1998–2013); the trends using these carbon parameters were calculated separately and then overlaid on the same plot. (b) All trends in the zonal mean carbonate ion concentration at depth from bottle data along repeat transect SR03 in our Region 3 (1994, 1996, 1998, 2001, 2003), where filled circles indicate significance at the 95% level and open circles, otherwise. Austral summer mean position of the Polar Front indicated by the (a) black line and (b) gray line. Mean position of Antarctic Polar Front indicated by the (a) black line and (b) gray line. See Table A.1 for data information.

particularly in Regions 2 and 3 of the Indian sector where hydrographic data are plentiful. Here, a decrease in calcification rate corresponds to a decrease in $[CO_3{}^{2-}]$ over the satellite period. The remaining two focus regions lack underway data for direct comparison. The Drake Passage, adjacent to our Region 4, has seen a decrease in summer $[CO_3{}^{2-}]$ (*Munro et al.*, 2015b). Given the relatively fast transport in this region of the Southern Ocean, the Drake Passage signal of decreasing $[CO_3{}^{2-}]$ could possibly be identified in Region 4 where we observe a significant decrease in calcification.

We estimated changes in the upper water column carbonate ion concentration from bottle data collected on transect SR03, on the eastern edge of our Region 3 (Figure 2.3b). Although hydrographic data from this line are relatively sparse in time, it is the only location with enough carbonate chemistry data to calculate full depth trends in any of our 4 regions. Our analysis of this data indicates that the upper 200 meters south of the PF have experienced a significant decrease in carbonate over 1994–2003. *Cubillos et al.* (2007) observed a north-south decline in calcification within the Australian sector over summers 2003 to 2006; they attribute this decline to shifts in calcifier morphotype abundance and distribution rather than changes in carbonate chemistry or surface warming. Here, we show that in addition to any shifts in inter-species dominance occurring over the past two decades, changes in carbonate chemistry (Figure 2.3) and surface warming (Figure A.1d) are concurrent with changes in calcification rates in this sector. Overall, our carbonate analyses suggest that the observed regional decreases in calcification correspond to regions exhibiting decreases in carbonate over similar time periods.

The proximity of these four focus regions to the Antarctic Polar Front (PF) begs the question whether there exists any association between variability in the location of the front and the observed calcification trends. In order to assess the variability in frontal position over time, we adapted and extended the PF analysis performed by *Dong et al.* (2006a) by calculating the PF location from all available weekly AMSR-E satellite SST data (2002–2011; see Section 2.3). The austral summer mean PF location is plotted as the black line in Figures 2.1 and 2.3 while the darker grey shaded area surrounding the mean (Figure 2.1b,d; Figure 2.3a) indicates the minimum and maximum latitudinal extent of the PF at any given time. The majority of trends observed (Figure 2.1b,d) are unrelated to variation in frontal location, with the exception of the positive trends observed in Region 1; the same is true for trends in chlorophyll concentration (Figure A.1b).

We find a significant southward shift in the mean position of the PF from summers 2003 to 2011 in Region 1 (Figure A.5). This poleward shift may have altered the physical and chemical properties of seawater in this region over time, particularly those that influence inter-species competition for available nutrients. Previous research indicates that the PF marks the boundary between silicate-poor and silicate-rich waters (*Sarmiento et al.*, 2004). Diatoms, the dominant plankton in the Southern Ocean, require a sufficient amount of silicic acid for production. A southward migration of the PF over this 9-year period may have reduced the availability of surface silicic acid here and therefore the ability of diatoms to effectively compete for nutrients. Such a change may have allowed coccolithophores to become more dominant in this region. One possible explanation for the positive trends in calcification (Figure 2.1b) and PIC (Figure 2.1d) in Region 1 is this southward migration of the PF over time.

Calculating trends in calcification rates from satellite observations comes with several caveats. The calcification algorithm used here, while validated, published, and widely used, was empirically derived from observations made primarily in the Northern Hemisphere oceans (*Balch et al.*, 2007). A more complete picture of changing calcification rates in the Southern Ocean from satellite products requires additional observations and validation using data collected in this region. Previous studies have suggested that chlorophyll concentration is underestimated in the Southern Ocean (*Johnson et al.*, 2013). Other studies find large underestimates in mean PIC from satellite; *Beaufort et al.* (2008) report the greatest density of coccoliths (individual calcite plates) at a depth below what is deemed detectable via satellite. However, it has also been suggested that PIC is being largely overestimated in the Southern Ocean (R. Johnson, manuscript in preparation). Figure A.4 demonstrates that over-/underestimations in PIC or chlorophyll concentration do not affect the trends reported here. The estimates presented here represent calcification and PIC standing stock occurring in the topmost layer of the ocean and are therefore not representative of these variables throughout the rest of the sunlit layer. Regardless of potential biases in the mean rate of calcification estimated from satellite, the variability and trends in both calcification rate and PIC concentration reported here are statistically robust.

2.5 Conclusions

In summary, we demonstrate that surface calcification and PIC concentrations have decreased in large portions of the Southern Ocean over the satellite record, concurrent with significant decreases in the surface ocean carbonate ion concentration. One exception is a large region of the Atlantic sector where positive trends in calcification rate correspond to a southward shift of the PF. In addition to changing carbonate chemistry as a result of global change, coccolithophores and other calcifiers will also experience increased stress from other physical and chemical factors that will likely impact organism processes. These results suggest that large-scale shifts in the ocean carbon cycle are already occurring and highlight organism and marine ecosystem vulnerability in a changing climate.

Acknowledgments

The SeaWiFS and MODIS-Aqua Level 3 particulate inorganic carbon, chlorophyll-a and sea surface temperature data were obtained from the NASA Ocean Colour distributed archive (http://oceancolor.gsfc.nasa.gov/). The AVHRR Oceans Pathfinder sea surface temperature data used in conjunction for the SeaWiFS era were obtained from www.science.oregonstate.edu/ocean.productivity/, and regridded to a 9 km grid. CO2SYS is obtainable from cdiac.ornl.gov/oceans/co2rprt/html. Weekly SST observations from AMSR-E ocean products used for the Polar Front analysis obtained online at http://www.ssmi.com. The Surface Ocean CO_2 Atlas (SOCAT) is an international effort, endorsed by the International Ocean Carbon Coordination Project, the Surface Ocean Lower Atmosphere Study, and the Integrated Marine Biogeochemistry and Ecosystem Research program, to deliver a uniformly quality-controlled surface ocean CO_2 database; we thank the many researchers and funding agencies responsible for the collection of data and quality control. Surface pCO_2 data can be found at http://cdiac.ornl.gov/oceans/LDEO_Underway_Database/.

We acknowledge generous funding from NSF (DGE−1144083, OCE−1155240) and NOAA (NA12OAR4310058). We thank Shenfu Dong for her help and guidance in our effort to extend the PF analysis.

Chapter 3

Mapping the Antarctic Polar Front: weekly realizations from 2002 to 2014

3.1 Abstract

We map the weekly position of the Antarctic Polar Front (PF) in the Southern Ocean over a 12-year period (2002–2014) using satellite sea surface temperature (SST) estimated from cloud-penetrating microwave radiometers. Our study advances previous efforts to map the PF using hydrographic and satellite data and provides a unique realization of the PF at weekly resolution across all longitudes (http://doi.pangaea.de/10.1594/PANGAEA.855640). The mean path of the PF is asymmetric; its latitudinal position spans from 44 to 64°S along its circumpolar path. SST at the PF ranges from 0.6 to 6.9°C, reflecting the large spread in latitudinal position. The average intensity of the front is 1.7°C per 100 km, with intensity ranging from 1.4 to 2.3°C per 100 km. Front intensity is significantly correlated with the depth of bottom topography, suggesting that the front intensifies over shallow bathymetry. Realizations of the PF are consistent with the corresponding surface expressions of the PF estimated using expendable bathythermograph data in the Drake Passage and Australian and African sectors. The climatological mean position of the PF is similar, though not identical,

to previously published estimates. As the PF is a key indicator of physical circulation, surface nutrient concentration, and biogeography in the Southern Ocean, future studies of physical and biogeochemical oceanography in this region will benefit from the provided data set.

3.2 Introduction

The large-scale circulation of the Southern Ocean (south of 35°S) is dominated by the strong, eastward flow of the Antarctic Circumpolar Current (ACC), connecting the major ocean basins and allowing for the transport of heat, nutrients, carbon, and other key climate variables globally and to the ocean interior (*Rintoul et al.*, 2001; *Sarmiento et al.*, 2004). The ACC is composed of many deep-reaching hydrographic fronts that divide the Southern Ocean up into physical and biogeochemical zones (see *Deacon*, 1982; *Pollard et al.*, 2002). The flow of the ACC is concentrated in several jets within which the majority of the circumpolar transport is carried (*Rintoul et al.*, 2001). The terms 'front' and 'jet' have often been used interchangeably throughout the ACC literature but are distinct features: an ACC front is a water mass boundary that is often associated with an ACC jet, a strong geostrophic current.

While as many as 10 distinct fronts can be realized in the Southern Ocean (*Sokolov and Rintoul*, 2007a), the three majorly recognized ACC fronts are, from north to south, the Subantarctic Front (SAF), Antarctic Polar Front (PF), and Southern ACC Front (*Orsi et al.*, 1995). At the PF, cold, fresh Antarctic surface waters subduct beneath warmer, saltier sub-Antarctic waters (Deacon, 1933; Deacon, 1937). At the surface, the PF is characterized by strong gradients in temperature, nutrients, and distinct biological communities (*Deacon*, 1933, 1937; *Mackintosh*, 1946; *Deacon*, 1982; *Trull et al.*, 2001). Accurately identifying the location of the PF has been an important and active area of research in recent decades as frontal position has implications for Southern Ocean eddy mean flow, air-sea fluxes, biological productivity, biogeography, and estimates of ACC transport (*Hughes and Ash*, 2001; *Pollard* *et al.*, 2002; *Sarmiento et al.*, 2004; *Ansorge et al.*, 2014).

There are multiple ways to identify the PF using temperature and salinity data collected on hydrographic and bathythermographic sections. A common method uses the 2°C isotherm at ∼200 m to mark the subsurface PF, as it is a good approximation of the northern extent of the cold, fresh Antarctic Surface Water that generally occupies the upper water column between the PF and the Antarctic continental shelf (*Orsi et al.*, 1995; *Belkin and Gordon*, 1996). While useful in capturing the vertical structure of the PF on regional scales and over short time periods, in situ data in the Southern Ocean is spatially and temporally sparse, making difficult the study of spatio-temporal variability in the PF.

Satellites have allowed for a large-scale view of the historically under-sampled Southern Ocean. Altimeter images of sea surface height (SSH) reflect features of the upper ocean density field and gradients in SSH have been used to characterize jet intensity and front location (*Gille*, 1994; *Sokolov and Rintoul*, 2007a; *Sallée et al.*, 2008). *Sokolov and Rintoul* (2002) demonstrate that regions of strong SSH gradients tend to coincide with particular SSH contours and that the circumpolar path of a particular SSH contour marks the location of an ACC front. However, SSH contouring methods to identify the PF should be approached with caution: *Graham et al.* (2012) show that an SSH contour is not always associated with an enhanced SSH gradient, challenging the accurate detection of the time-varying front.

Given the signature strong sea surface temperature (SST) gradient at the PF, satellite images of SST can also be used to identify the PF. However, previous PF studies have used infrared retrievals of SST (*Legeckis*, 1977; *Moore et al.*, 1997, 1999) which are greatly affected by water vapor and clouds, a persistent feature of the Southern Ocean. SST estimates from cloud-penetrating microwave radiometers circumvent the above PF mapping limitations, first demonstrated by *Dong et al.* (2006a).

Our study learns from and advances previous efforts to map the PF. Herein, we use the continuous, all-weather microwave SST record at 25 km resolution to estimate the weekly location of the PF from 2002 to 2014. As such, our method avoids water vapor and cloud contamination and provides circumpolar realizations of the PF at high spatial and temporal resolution. Our realizations of the Polar Front are made publicly available (Section 3.7) so as to benefit studies of Southern Ocean physical and biogeochemical oceanography (e.g., *Munro et al.*, 2015a,b; *Freeman and Lovenduski*, 2015). In the following sections we detail our PF identification method (Section 3.3), use available expendable bathythermograph (XBT) data to test our method in select sectors of the Southern Ocean (Section 3.4), and discuss the mean path of the PF (Section 3.5). A companion paper investigates spatial and temporal variations in the PF and its linkages with key modes of climate variability (*Freeman et al.*, 2016).

3.3 Methods

3.3.1 Sea surface temperature observations

In this study we utilize Remote Sensing System's daily optimally interpolated microwave SST data on a 25 km grid; daily SSTs were averaged over 7 days ending on and including the Saturday file date to create a weekly product. This all-weather SST product is derived from in situ estimates and all available microwave SST radiometers operating on a given day between 02 June 2002 and 22 February 2014: the Advanced Microwave Scanning Radiometers (AMSR-E and AMSR-2) and WindSat Polarimetric Radiometer (see *Reynolds and Smith*, 1994). Data processing involves many quality control measures, including the removal of rain- or sea ice-contaminated SSTs and consideration of diurnal warming and sensor error. It is important to note that there are a few instances in the data record when no radiometer was operational and the SST retrieval from the previous day is used persistently (outages range ~1-7 days). For further details on data processing and specific dates of SST persistence, the reader is encouraged to visit www.remss.com/measurements/sea-surface-temperature/oisst-description.

3.3.2 Mapping the Polar Front

We build on the technique first presented by *Moore et al.* (1997) of using satellite SST gradient maxima to locate the PF. In general, our PF mapping technique is based on locating the southern bound at which the SST gradient exceeds 1.5°C over a 100 km distance, as in *Dong et al.* (2006a). At longitudes where this criterion cannot be satisfied or when large latitudinal distances exist between adjacent longitudes, steps are taken to satisfy spatial and/or thermal continuity, oftentimes as a relaxation of the above limit (see following subsections). *Dong et al.* (2006a) use 2σ and the temporal mean PF to identify such discontinuity. Here, we identify additional physical characteristics of the PF and use this information in a comprehensive mapping scheme. Our methodology does not require knowledge of a temporal mean PF; all information needed to map the PF is found locally. Our mapping scheme yields one continuous, unique PF realization for a given period of time. In regions where the PF is known to have multiple filaments (*Sokolov and Rintoul*, 2002), our algorithm typically selects the southernmost.

PF identification procedure

South of 40°S, we compute the absolute SST gradient (°C km^{-1}) at each grid point,

$$|\Delta T| = \sqrt{(\delta T/\delta x)^2 + (\delta T/\delta y)^2},$$

where δT is the temperature difference (°C) and δx and δy are the kilometer distances between any two longitude or latitude points, respectively. We do not perform initial, first-guess frontal identification (a) in regions where SST is warmer than 10°C, as these are waters characteristic of the SAF (*Dong et al.*, 2006a), (b) within small patches of high SST gradients (closed contours less than 3 degrees of latitude and longitude), so as to reduce noise (as in *Dong et al.*, 2006a), and (c) within 1 degree of latitude of the Antarctic continent or sea ice, in case of melt-influenced SSTs (*Smith and Comiso*, 2008).

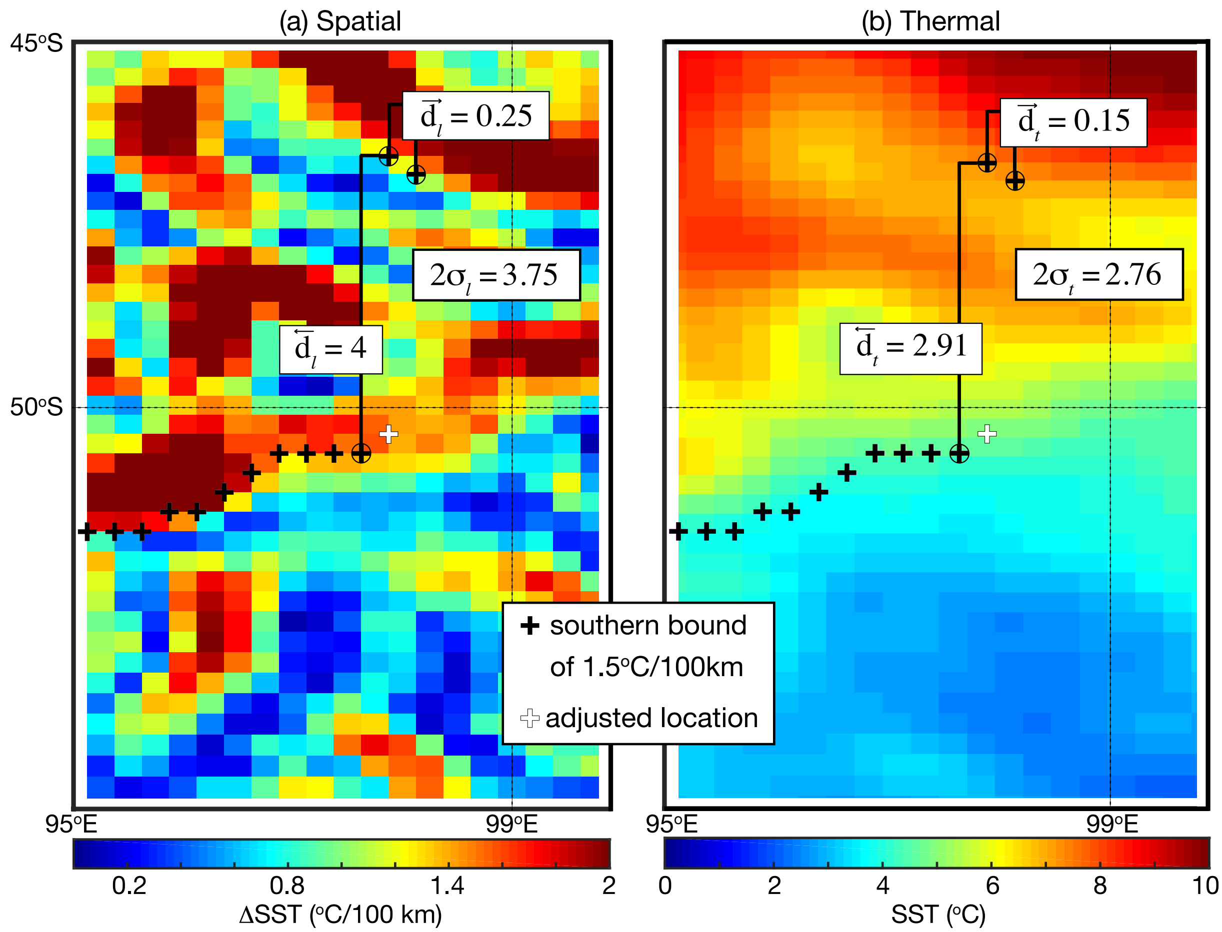

Figure 3.1: Example of (a) spatial and (b) thermal discontinuity resulting in an adjustment in the PF location according to (1) as outlined in Section 3.3.2. d_l, $2\sigma_l$ in units of °latitude and d_t, $2\sigma_t$ in units of °C.

Continuity tests

PF maps are checked for spatial and thermal continuity to determine whether an adjustment in the PF is necessary. Starting at the Greenwich Meridian and moving east, with the general flow of the ACC, we calculate the absolute differences (d) in latitude (l; °latitude), temperature (t; °C), and monthly climatological temperature (tc; °C) between the current position and the point to the west ($\leftarrow$) and east ($\rightarrow$), twice the standard deviation of these differences (normalized by N = 2), $2\sigma_l$ (°latitude) and $2\sigma_t$ and $2\sigma_{tc}$ (°C) respectively, and an additional difference (Δ) between 2σ and d (e.g., $\overleftarrow{\Delta_l} = |\ \overleftarrow{d_l}$ - $2\sigma_l\ |$). Invoking tc is necessary when injections of polar water from the south or subantarctic water from the north affect frontal identification.

An adjustment in the PF position is required if $2\sigma_l > 0.75$°latitude or ($2\sigma_l \leq 0.75$°latitude and ($\overleftarrow{\Delta_l} > 0.25$°latitude or $\overrightarrow{\Delta_l} > 0.25$°latitude)) and any of the following are satisfied:

$$\begin{cases} 2\sigma_l = \overleftarrow{d_l} \text{ and } (\overleftarrow{d_t} \geq 2\sigma_t \text{ or } \overleftarrow{d_{tc}} \geq 2\sigma_{tc}) & \\ \overleftarrow{d_l} < 2\sigma_l < \overrightarrow{d_l}, & \overrightarrow{\Delta_l} > 1 \\ 2\sigma_l < \overleftarrow{d_l} \text{ and } (2\sigma_t < \overleftarrow{d_t} \text{ or } 2\sigma_{tc} < \overleftarrow{d_{tc}}) & \\ 2\sigma_l < \overleftarrow{d_l} \text{ and } \overleftarrow{d_t} < 2\sigma_t < \overrightarrow{d_t}, & \overrightarrow{\Delta_t} > 1 \end{cases} \qquad (1)$$

Figure 3.1 exemplifies spatial and thermal discontinuity according to (1) and shows the subsequent adjustment made in this particular case (adjustment procedure detailed in the following subsection). Here, black plus signs indicate the first-guess PF position (i.e., the southern bound of the 1.5 temperature gradient criterion after removing noise/patches), where the current position being tested for continuity and its immediate neighbors to the west and east are indicated by black open circles. As spatial and thermal continuity is violated in this case (see difference and standard deviation information provided in text boxes), an adjustment in the PF position is made (white plus sign).

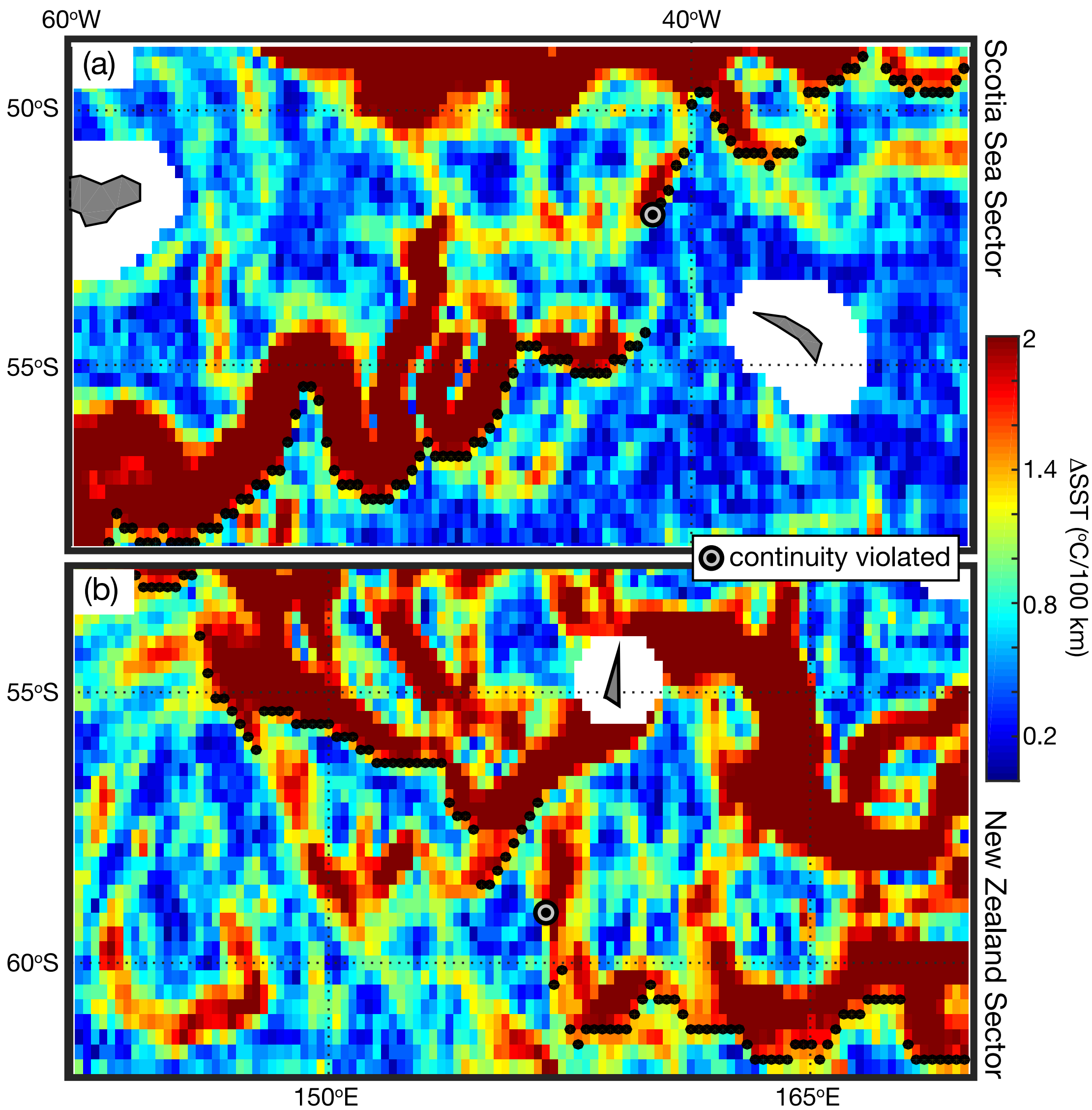

Figure 3.2: Example cases when spatial and thermal discontinuity is justified: frontal filaments (a) disconnected or (b) situated north-south.

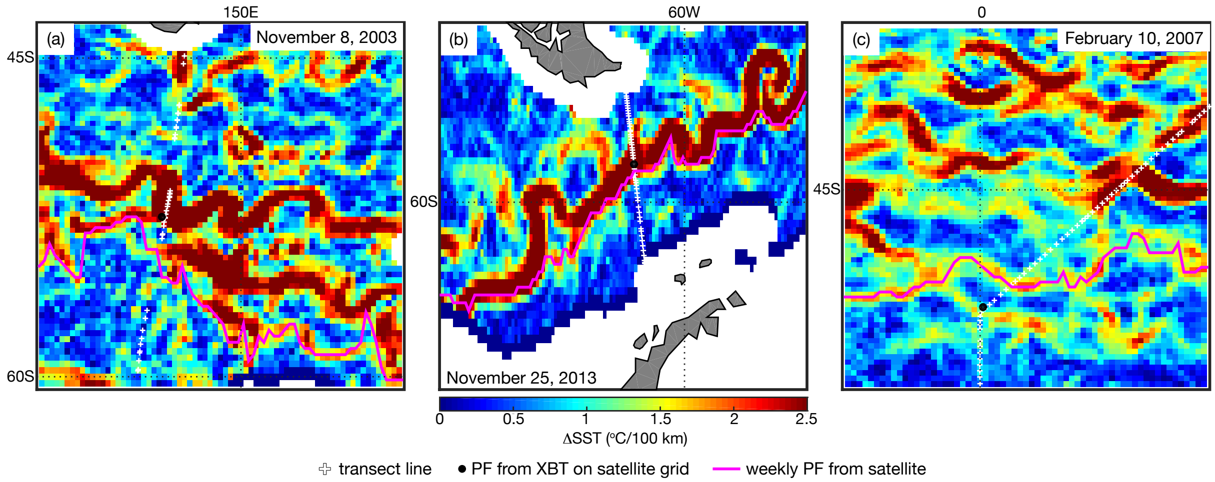

Figure 3.3: PF location identified from surface XBT data (timestamp indicated) overlain on the corresponding weekly satellite-estimated ΔSST and PF realization in the (a) Australian, (b) Drake Passage, and (c) African sectors.

Adjustments

Following spatial and thermal continuity testing, we identify potential adjustment locations as those that satisfy $\overleftarrow{\mathrm{d}_l} < 2\sigma_l$ and $\overrightarrow{\Delta_l} < 1$ (see Figure 3.1). Here, we locate the southernmost position of the 0.015°C km^{-1} absolute SST gradient. If a gradient of that magnitude is not found, we successively relax the gradient by 0.001°C km^{-1} to a lower limit of 0.011°C km^{-1} in order to find the front. In cases where gradients are relatively weak (i.e., $|\Delta \mathrm{T}| < 0.011$°C km^{-1}), we use local gradient maxima (>0.008°C km^{-1}) to mark the position of the front.

In some cases, spatial or thermal discontinuity is justified. This generally occurs when two filaments are disconnected (Figure 3.2a; *Sokolov and Rintoul*, 2002), or when a branch of the front is predominantly situated north-south (Figure 3.2b).

Post-processing

In certain sectors of the Southern Ocean, the characteristics of the PF are such that mapping requires executing the above steps in the opposite direction, from east to west, in order to adequately capture the front's curled, folded, or multi-filament structure (*Sokolov and Rintoul*, 2002) or when it merges with or diverges from the SAF to the north (*Read and*

Pollard, 1993; *Moore et al.*, 1997; *Cunningham et al.*, 2003). The following areas of the Southern Ocean are often mapped as outlined in the previous subsections but from east to west: ~20-32°E, ~50-62°E near Crozet, ~72-80°E near Kerguelen, ~125-150°E along the Southeast Indian Ridge, ~170-190°E in the New Zealand sector, ~200-215°E along the Pacific-Antarctic Ridge, ~240-300°E in the E. Pacific, and ~352-360°E along the Mid-Atlantic Ridge.

3.4 Validating the Polar Front position

In order to verify our methods, we compare realizations of PF location to those estimated from high-resolution XBT surface (<10 m) temperature data. XBT data are available from three Southern Ocean repeat lines: between Hobart, Australia and the Dumont d'Urville Station, Antarctica (line IX28; 64 transects; hereafter referred to as the Australian sector), across Drake Passage (line AX22; 73 transects), and another between Cape Town, South Africa and Sanae IV Station, Antarctica (line AX25; 25 transects; hereafter referred to as the African sector). We note that XBT sampling in the Australian and African sectors is biased to summer and spring seasons, whereas XBT data collected year-round in the Drake Passage (see *Sprintall*, 2003).

Along each transect, we interpolate the XBT SSTs to match the satellite grid resolution and compute meridional surface temperature gradients ($\delta T/\delta y$). We seek to find the in situ PF within one standard deviation of the weekly satellite PF location. In the African and Australian sectors, we identify the in situ PF as the southernmost latitude where $\delta T/\delta y \geq 0.015$°C km^{-1}. Given the strength of the SST gradient in Drake Passage, we adjust our definition to identify the southernmost latitude of the strongest $\delta T/\delta y$ exceeding 0.015°C km^{-1}.

We quantify the error associated with our PF mapping scheme in these three regions by calculating the root-mean-square error (RMSE), a measure of the average magnitude of the

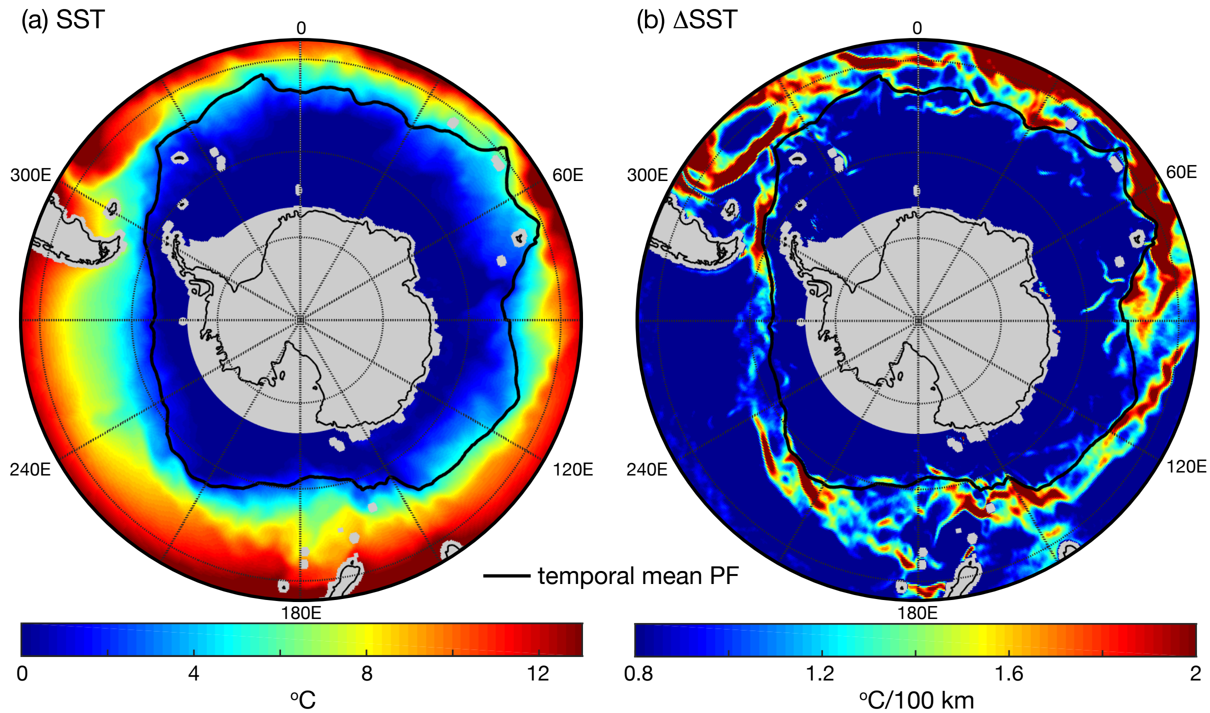

Figure 3.4: Southern Ocean (a) mean SST and (b) absolute SST gradient with climatological PF overlain (June 2002-February 2014).

latitudinal differences between the PF inferred from XBT data (PF_X) and that from weekly microwave data (PF_M), as:

$$RMSE = \sqrt{\frac{\sum_{i=1}^{n}(PF_{X,i} - PF_{M,i})^2}{n}},$$

where n corresponds to the number of transects in a given sector. Table 3.1 lists RMSE and sample size by sector. Transects where a meridional temperature gradient satisfying our 0.015°C km^{-1} criterion could not be identified were excluded from these calculations (8 transects in total).

Differences between in situ and satellite PF locations are likely attributed to one or more of the following: (1) interpolating XBT SSTs on to the satellite grid, (2) differences in the representative temperature measured by the two sources ('bulk' versus 'subskin'; see *Dong et al.*, 2006b), (3) errors in the original temperature data (e.g., manufacturer, accuracy, pre-

Table 3.1: Estimated PF location RMS error (degrees of latitude) and sample size (n), by sector.

	RMSE	n
Australian sector	1.1640	59
Drake Passage	0.5373	71
African sector	0.7971	24

cision, etc.), (4) the regional complexity of the front (i.e., magnitude of mesoscale variability, typical number of branches, etc.), or (5) comparing a daily in situ PF with the corresponding weekly satellite PF.

The PF within the Australian and African sectors (RMSE 1.1640 and 0.7971°latitude, respectively; $2\sigma = 2.33$ and 2.09°latitude, respectively), is known for its multi-filament structure (*Belkin and Gordon*, 1996; *Moore et al.*, 1999; *Sokolov and Rintoul*, 2002, 2009a), making difficult the comparison between in situ and satellite-based definitions. For example, Figure 3.3a shows more than one potential frontal location along a November 2003 transect south of Australia; the in situ PF is identified as the more northerly filament while our weekly PF realization marks the more southerly filament. Figure 3.3c shows a summertime African transect where the in situ PF is identified as a more southerly filament and our weekly realization represents the northern, more spatially continuous filament. In Drake Passage (RMSE = 0.5373°latitude; $2\sigma = 1.47$°latitude), the PF is largely constrained by bathymetry (*Moore et al.*, 1997) and characterized by an intense temperature gradient. Figure 3.3b shows a summertime Drake Passage transect where the in situ and satellite PF are identified one grid box apart (0.25°latitude). Such consistent identifications are reflected in the RMSE here, where on average, our mapping technique will provide PF positions within ~0.5°latitude of an in situ position in a given week.

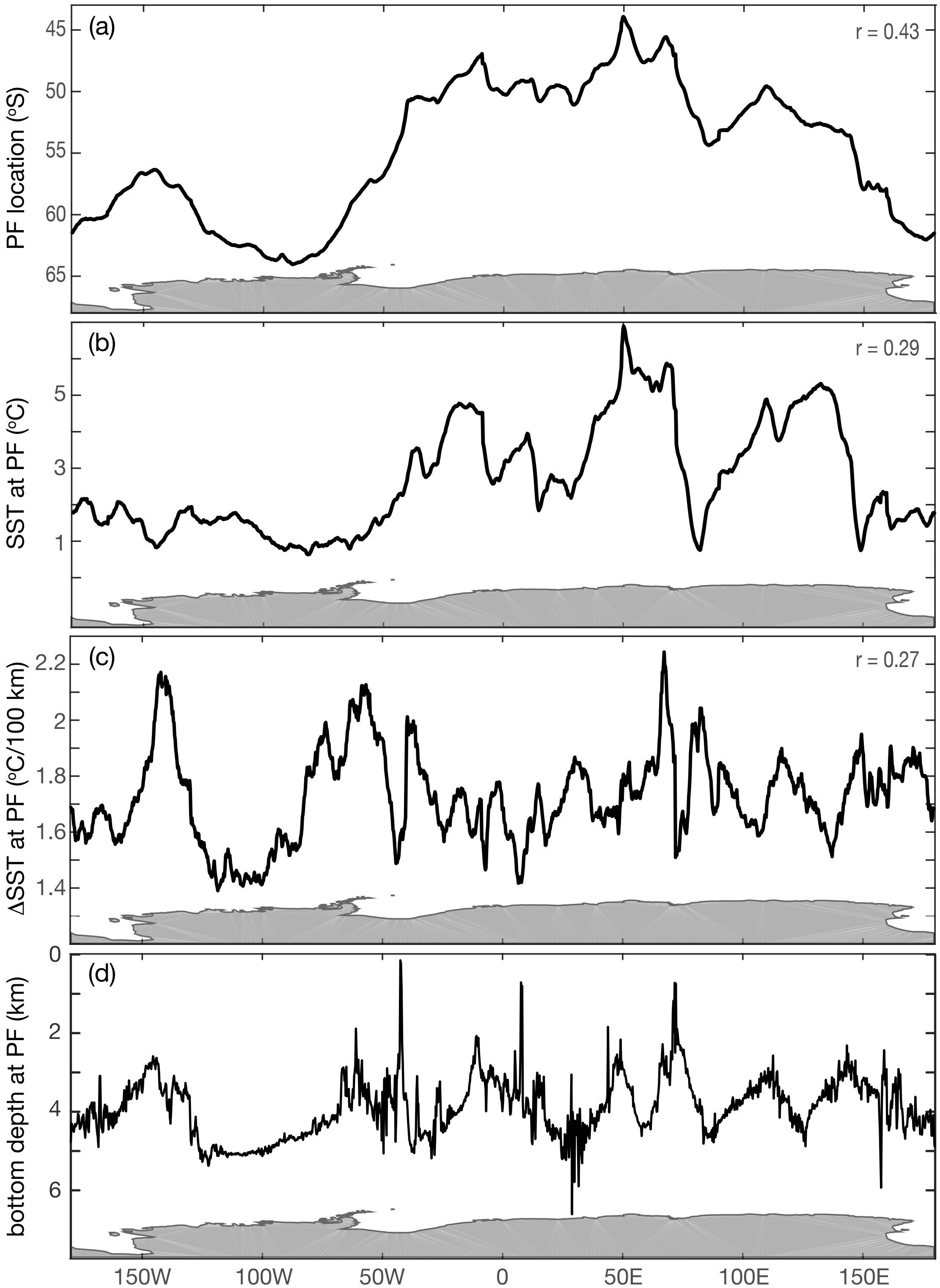

Figure 3.5: Climatological (a) PF location and (b) SST, (c) absolute SST gradient, and (d) bottom depth at the PF (June 2002–February 2014). Statistically significant (>95%) correlation coefficients with bottom depth are indicated in the top right corner of (a–c).

3.5 Results and Discussion

We investigate the climatological position of the front by averaging weekly realizations over 2002–2014 (Figure 3.4, Figure 3.5). The climatological path of the PF is zonally asymmetric, traversing nearly 20° of latitude from its northernmost position in the southwest Indian Ocean (43.89°S) to its southernmost position in the southeast Pacific (64.08°S; Figure 3.4; Figure 3.5a). It follows that the climatological temperature along the path of the PF ranges from 0.6 to 6.9°C (Figure 3.4a; Figure 3.5b). The climatological intensity of the PF (defined as the absolute SST gradient at the front) averaged over all longitudes is 0.0173°C km^{-1}. Climatological intensity ranges from 0.0139 to 0.0225°C km^{-1} (Figure 3.4b; Figure 3.5c), possibly reflecting changes in ACC transport along the front (*Dong et al.*, 2006a).

Figure 3.5 suggests that the mean position, temperature, and intensity of the PF are closely linked to the depth of the underlying topography (r = 0.43, r = 0.29, and r = 0.27, respectively), in agreement with previous PF studies (*Gille*, 1994; *Moore et al.*, 1999; *Sokolov and Rintoul*, 2002; *Dong et al.*, 2006a; *Sallée et al.*, 2008). Indeed, the front tends to be southerly, cold, and weak over the deep ocean, and northerly, warm, and intense over shallow bathymetry. In the southwest Indian sector, the PF is in its northernmost position and characterized by warm SSTs (Figure 3.4; Figure 3.5a,b). Generally, the PF has a more southerly position in the deep, east Pacific sector, characterized by cooler SSTs and relatively weak SST gradients (Figure 3.4; Figure 3.5; *Moore et al.*, 1999; *Dong et al.*, 2006a). Figure 3.5c demonstrates that the PF intensifies at major topographic features, which are associated with strong, large-scale potential vorticity gradients that act to constrain the flow (*Gordon et al.*, 1978; *Sallée et al.*, 2008), including the Kerguelen Plateau (∼80°E), across the Southeast Indian Ridge (∼150°E), Drake Passage (∼60°W), and the Pacific-Antarctic Ridge (∼140°W).

We compare the climatological position of our PF with that estimated by the studies of *Orsi et al.* (1995), *Belkin and Gordon* (1996), *Moore et al.* (1999), and *Dong et al.* (2006a) in Figure 3.6, where the paths of the front are overlain on a map of bottom topography (*Smith* *and Sandwell*, 1994). The topographic influence on the position of the front is apparent: regions of strong topographic steering coincide with regions where all five climatological paths are in good agreement (e.g., along the Southeast Indian and Pacific-Antarctic Ridges in the New Zealand and Ross Sea sectors, respectively, through Drake Passage south of the Falkland Islands, and the eastern flank of Kerguelen Plateau) and these paths diverge from one another in deep ocean regions with weak to no topographic steering (e.g., the southeast Indian and Pacific sectors).

Given the diversity in the methods and data used to identify the fronts shown in Figure 3.6, we do not expect the individual climatological paths to agree everywhere. For example, the *Orsi et al.* (1995) and *Belkin and Gordon* (1996) studies use hydrographic data to identify the front's subsurface expression, the northern extent of the 2°C isotherm at ∼200 m, while *Moore et al.* (1999) (*Dong et al.*, 2006a) identify the front as an SST gradient using infrared (microwave) satellite retrievals from 1987 to 1993 (2003 to 2005). Our climatological PF diverges most from that of *Moore et al.* (1999) in areas where persistent cloud cover contaminates the infrared SST retrieval (e.g., ∼50–70°E and ∼110–140°E). Since our study builds on the PF identification method presented in *Dong et al.* (2006a), it follows that the climatological position of our PF most closely matches that of *Dong et al.* (2006a).

Our climatological PF merges with the SAF north of the Crozet Archipelago (∼50°E), similar to (*Dong et al.*, 2006a). It passes to the north of the Kerguelen Plateau (∼70°E), as in *Orsi et al.* (1995), *Belkin and Gordon* (1996), *Dong et al.* (2006a), and *Sokolov and Rintoul* (2009b). South of Crozet and Kerguelen, SST gradients are generally too weak to discern frontal filaments.

In the southeast Atlantic sector (330–350°E), our climatological PF extends further north than previous climatologies. This sector is characterized by many disconnected, smaller-scale frontal filaments south of the SAF. The continuity constraint in our method precludes identification of small-scale features as part of the PF, so here the PF follows the strongest and most coherent filament.

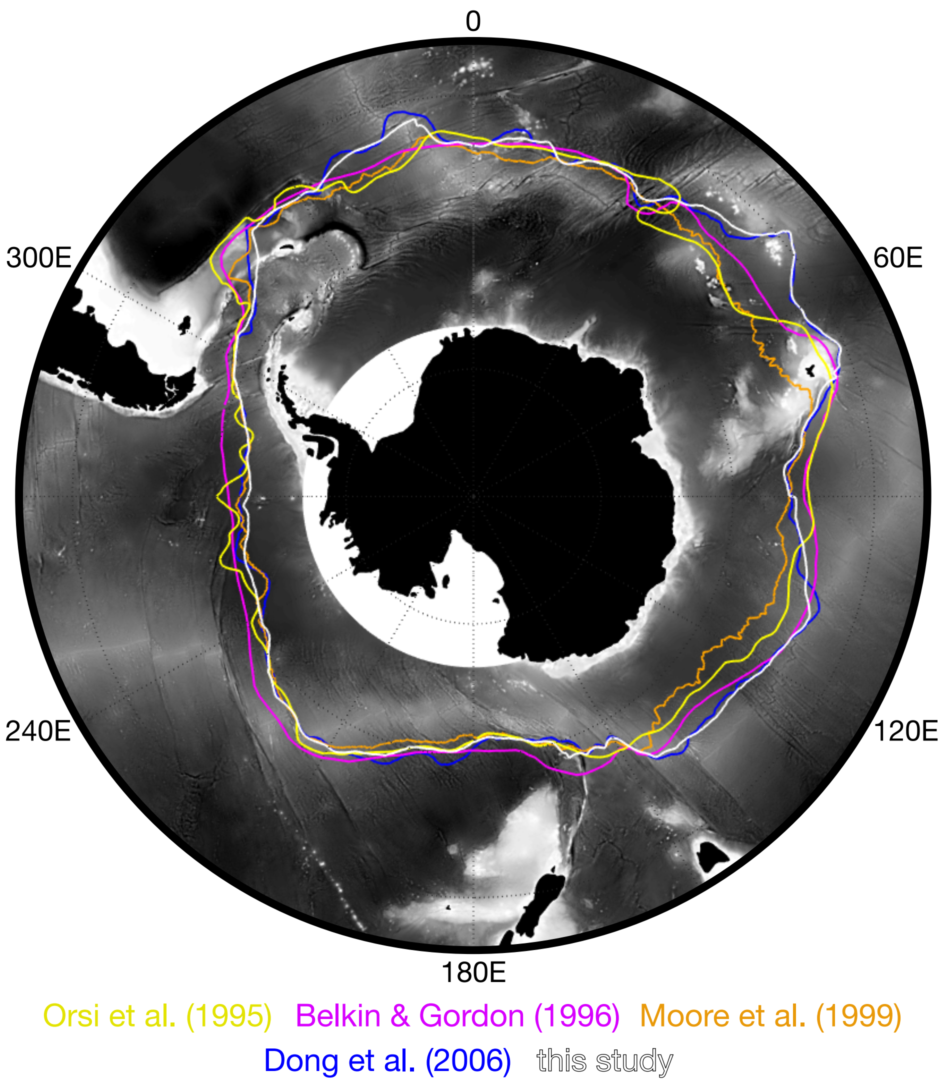

Figure 3.6: The climatological position of the PF in this and previous studies overlain on bottom topography obtained from the National Geophysical Data Center (www.ngdc.noaa.gov/mgg/dat/misc/predicted_seafloor_topography/TOPO/), where light (dark) shading indicates shallow (deep) bathymetry.

3.6 Conclusions

In summary, this study maps the Antarctic Polar Front from 2002 to 2014 at weekly resolution and provides the first temporally-varying PF data set derived from SST available to the scientific community. We outline a verified methodology to locate the PF throughout the Southern Ocean using the high-resolution, all-weather microwave SST data record. Further, we describe the climatological position, surface temperature, and intensity of the PF and compare our climatological PF to previous studies. As evidence for a variable and changing Southern Ocean grows (*Gille*, 2002; *Böning et al.*, 2008; *Cai et al.*, 2010; *Munro et al.*, 2015a; *Landschützer et al.*, 2015), determining the response of the PF to such changes is ever more crucial. For an investigation of intraannual to interannual variability of the PF and associated drivers/mechanisms utilizing this high-resolution PF data set, the interested reader is encouraged to see our companion paper (*Freeman et al.*, 2016).

3.7 Polar Front data availability

Weekly PF locations can be found at http://doi.pangaea.de/10.1594/PANGAEA.855640 in netCDF (network Common Data Form) format and viewed as an animation.

Acknowledgments

Microwave OI SST data are produced by Remote Sensing Systems and sponsored by National Oceanographic Partnership Program (NOPP), the NASA Earth Science Physical Oceanography Program; data are available at http://www.remss.com. Drake Passage and Australian sector XBT data were made available by the Scripps High Resolution XBT program (www-hrx.ucsd.edu). XBT data from the African sector were made freely available by the Atlantic Oceanographic and Meteorological Laboratory and are funded by the NOAA Office of Climate Observations (http://www.aoml.noaa.gov/phod/hdenxbt/ax_home.php?ax=25). The *Orsi et al.* (1995) climatological PF position was obtained from the Australian Antarctic

Data Center (*Orsi and Harris*, 2001). Bottom topography data were obtained at www.ngdc.noaa.gov/mgg/dat/misc/predicted_seafloor_topography/TOPO/. We thank S. Dong for providing her mean PF path. We are grateful for support from NSF (DGE-1144083; OCE-1155240; OCE-1258995) and NOAA (NA12OAR4310058).

Chapter 4

Temporal variability in the Antarctic Polar Front (2002–2014)

4.1 Abstract

We investigate intraannual to interannual variability in the Antarctic Polar Front (PF) using weekly PF realizations spanning 2002 to 2014. While several PF studies have used gradient maxima in sea surface temperature (SST) or height to define its location, results from this study are based on a PF defined using SST measurements that avoid cloud contamination and the influence of steric sea level change. With a few regional exceptions, we find that the latitudinal position of the PF does not vary seasonally, yet its temperature exhibits a clear seasonal cycle. Consistent with previous studies, the position and intensity of the PF is largely influenced by bathymetry; generally, over steep topography we find that the front intensifies and interannual variability in its position is low. We also investigate drivers of PF variability in the context of large-scale climate variability on various spatial and temporal scales, but find that the major modes of Southern Hemisphere climate variability explain only a tiny fraction of the interannual PF variance. Over the study time period, the PF intensifies at nearly all longitudes while exhibiting no discernible meridional displacement in

its zonal mean path.

4.2 Introduction

The large-scale circulation of the Southern Ocean is largely driven by the overlying westerly winds and buoyancy forcing (*Marshall and Speer*, 2012). The strong westerly winds force the eastward-flowing, zonally unbounded Antarctic Circumpolar Current (ACC) and set up a globally-significant meridional overturning circulation. Light, surface waters are forced equatorward through Ekman transport and cold, dense, nutrient- and carbon-rich, and oxygen-poor waters must upwell from below. Here, upwelling water has the opportunity to exchange heat and carbon at the air-sea interface before cooling and sinking to the south to form bottom water or warming and advancing to the north as intermediate and mode water. These pathways help ventilate the global ocean, transporting heat, carbon, nutrients, oxygen, and other oceanic properties (*Rintoul et al.*, 2001; *Sarmiento et al.*, 2004; *Sabine et al.*, 2004; *Mignone et al.*, 2006; *Sallée et al.*, 2012). While the ACC connects the southern Atlantic, Indian, and Pacific ocean basins, it also acts as a barrier to poleward heat transport, contributing to the unique and isolated Antarctic climate (*Rintoul et al.*, 2001). The poleward transport of heat by mesoscale eddies formed within the ACC is likely the only compensation for heat lost during air-sea exchange (*de Szoeke and Levine*, 1981; *Rintoul et al.*, 2001)

Making up the vast ACC are multiple hydrographic fronts characterized by strong meridional gradients in oceanic properties, formed via eddy-mean flow interaction, and delineating physical and biogeochemical zones (*Deacon*, 1982; *Pollard et al.*, 2002). Of these, the Antarctic Polar Front (PF; climatological position shown in Figure 4.1a) marks the transition between cold, fresh Antarctic water and warmer, saltier sub-Antarctic waters as well as the boundary between nutrient-rich and nutrient-poor waters (*Pollard et al.*, 2002; *Sarmiento et al.*, 2004). The position of the PF has implications for the physical and biogeochemical

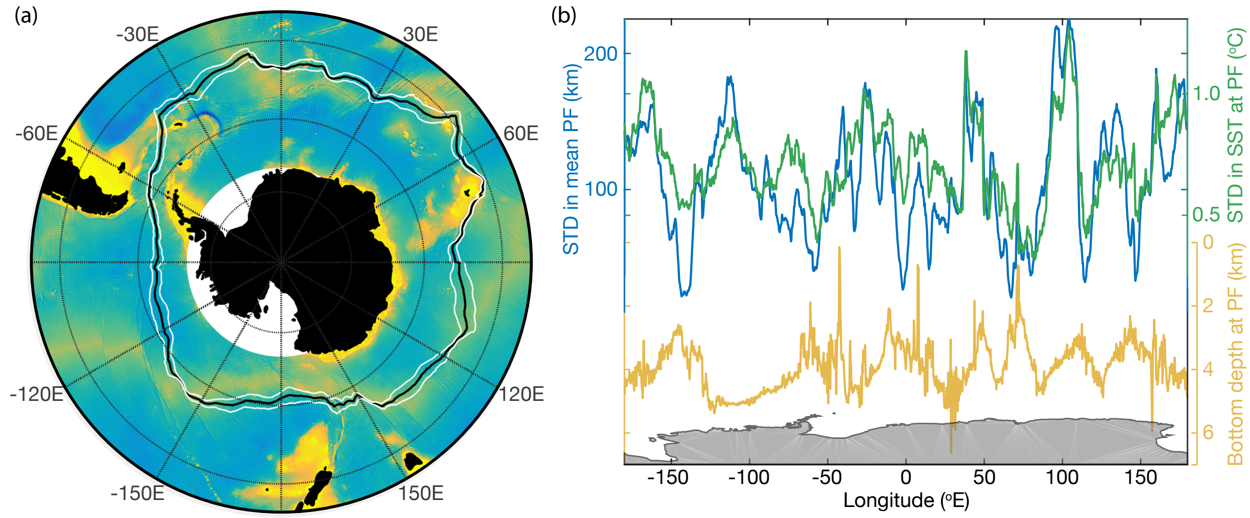

Figure 4.1: (a) Temporal mean (black contour) and standard deviation (white contours indicate $\pm 1\sigma$) in the monthly Polar Front position (June 2002 - February 2014) overlain on predicted seafloor topography obtained from the National Geophysical Data Center (www.ngdc.noaa.gov/mgg/dat/misc/predicted_seafloor_topography/TOPO/; *Smith and Sandwell*, 1994), where warm colors indicate shallow bathymetry and cool colors, deep. (b) Standard deviation in monthly mean PF position (blue) and anomalous SST at the PF (green) along with bottom depth at the mean PF (yellow).

state of the Southern Ocean, as shifts in the location could cause changes in eddy heat fluxes, air-sea fluxes, basin temperature, biological productivity, or biogeography (*Ansorge et al.*, 2014; *Swart and Speich*, 2010; *Gille*, 2002; *Moore and Abbott*, 2000; *Pollard et al.*, 2002). Yet, the temporal variability and long-term trends in the position and strength of the circumpolar PF are still poorly understood, largely due to (a) the paucity of high-resolution, repeat hydrographic data (as in *Orsi et al.*, 1995; *Belkin and Gordon*, 1996), (b) cloud-contamination of infrared satellite coverage (as in *Moore et al.*, 1999), and (c) disparities between commonly-employed PF identification methods (see *Langlais et al.*, 2011; *Graham et al.*, 2012; *Chapman*, 2014; *Gille*, 2014), including those using sea surface height (SSH) data that may be sensitive to the large-scale steric height changes characteristic of climate change (e.g., *Sokolov and Rintoul*, 2009b).

Using historical hydrographic data, the frontal studies of *Orsi et al.* (1995) and *Belkin and Gordon* (1996) provided a first look at the mean location and structure of the circumpolar

PF, but given the lack of repeat observations, its time-varying properties could not be investigated. Observing both SSH and temperature (SST) via satellite has allowed for the remote detection of fronts at greater temporal and spatial resolution (*Gille*, 1994; *Moore et al.*, 1999; *Sokolov and Rintoul*, 2002; *Dong et al.*, 2006a).

Several previous studies have used SSH contouring methods to investigate PF variability (see *Sokolov and Rintoul*, 2002; *Sallée et al.*, 2008; *Sokolov and Rintoul*, 2009b; *Billany et al.*, 2010; *Kim and Orsi*, 2014). *Sokolov and Rintoul* (2009a) present the spatio-temporal variability of the PF over a 15-year period (1992–2007) and document an observed long-term southward displacement in PF position. *Sallée et al.* (2008) suggest that on regional scales, the PF (1993–2005) shifts in spatially inhomogeneous ways in response to large-scale climate variability. However, SSH-based frontal analyses leave a number of open questions. First, shifts in the position of fixed SSH contours are potentially sensitive to steric sea level rise (i.e., thermal expansion), likely associated with a warming Southern Ocean (*Gille*, 2002). Second, *Graham et al.* (2012) highlight that since an SSH contour is not always associated with an enhanced SSH gradient, particularly in regions where fronts weaken or dissipate, tracking these SSH contours alone is insufficient for quantifying variability and change in the PF.

Given the marked temperature gradient at the PF, a few studies have used SST gradient-based definitions to identify its location; methods which are insensitive to steric expansion but previously lacked adequate spatial and temporal resolution. *Moore et al.* (1999) suggest that the PF (1987–1993) exhibits seasonal variability and is greatly influenced by bottom topography. *Dong et al.* (2006a) suggest that displacements in the overlying wind position force shifts in the PF. However, *Moore et al.* (1999) utilize infrared SSTs and therefore cannot resolve the PF in any areas contaminated by clouds and, although microwave radiometers can penetrate cloud cover (see *Wentz et al.*, 2000), *Dong et al.* (2006a) only investigate the first 3 years (2003–2005) of the cloud-penetrating microwave SST record. Circumventing the above SST and SSH methodological limitations, *Freeman and Lovenduski* (2016a) map the

PF at high spatial and temporal resolution for ∼12 years of the microwave record.

Here, we utilize the first long-term, high-resolution PF data set derived from microwave radiometer-based SST gradients (*Freeman and Lovenduski*, 2016a,b) to investigate intraannual to interannual variability and trends in the position and strength of the Antarctic Polar Front from 2002 to 2014 and its linkages with the leading patterns of climate variability.

4.3 Data and Methods

Monthly anomalies are computed by removing the long-term climatological monthly mean. To compute seasonal averages, we average over June–August (JJA), September-November (SON), December–February (DJF), and March–May (MAM). Prior to correlation and regression analysis, datasets are detrended by removing the long-term linear (least squares) trend. Trends are discussed in Section 4.4.3. The statistical significance (at the 95% level) of all reported trends are assessed using the Student's t-test. We use the method of *Bretherton et al.* (1999) to test the statistical significance of all reported correlation coefficients in the presence of autocorrelation.

4.3.1 Time-variable Polar Front properties

Freeman and Lovenduski (2016a) construct ∼12 years of weekly realizations of PF position (612 weeks spanning 02 June 2002 to 22 February 2014), inferred from gradient maxima in microwave SSTs (Microwave OI SST Remote Sensing Systems product, version 4). The methods presented in their study advance previous PF-identification efforts by avoiding water vapor and cloud contamination (see *Wentz et al.*, 2000) and providing circumpolar realizations at high spatial and temporal resolution; these PF realizations are shown to be consistent with those inferred from bathythermographic data and previously published climatologies. Their comprehensive PF mapping scheme locates regions where the absolute gradient in SST exceeds a 1.5 degrees Celsius change over a 100 km distance, relaxing this gradient criterion in order to ensure spatial and/or thermal continuity. The reader is referred to *Freeman and Lovenduski* (2016a) for a detailed description of the PF mapping technique. In this study, weekly PF data (*Freeman and Lovenduski*, 2016b) retain 0.25° spatial resolution and are averaged to monthly temporal resolution (141 months total).

As in *Freeman and Lovenduski* (2016a), the variables *SST* and Δ*SST at the PF* indicate the SST and absolute SST gradient, respectively, identified at the latitude, longitude, and time of the PF realization. We define the absolute SST gradient as,

$$|\Delta T| = \sqrt{(\delta T/\delta x)^2 + (\delta T/\delta y)^2},$$

where δT is the temperature difference (°C) and δx and δy are the kilometer distances between any two longitude or latitude points, respectively. We further refer to the SST gradient at the PF as the intensity or strength of the PF.

Since zonal mean SST and ΔSST at the PF exhibit seasonality (see Section 4.4.1), the seasonal cycle is removed from these variables prior to statistical analysis. As the majority of meridional PF position and intensity do not exhibit seasonal cycles (not shown), the seasonal cycle is only removed from the meridional SST at the PF prior to statistical analysis.

4.3.2 Wind speed and the surface westerly jet

To determine the role of wind on PF variability, we use merged microwave radiometer wind speed data (representing speeds at 10 m height) processed by Remote Sensing Systems (*Remote Sensing Systems*, 2016). This wind product is on a 1 degree grid at monthly temporal resolution and derived from the following satellite radiometers: Special Sensor Microwave Imager (SSM/I F08 through F15), Special Sensor Microwave Imager Sounder (SSMIS F16 and F17), WindSat Polarimetric Radiometer, and Advanced Microwave Scanning Radiometer (AMSR-2). Data processing involves many quality control measures, including the removal of rain- or sea ice-contaminated wind speeds, post-hoc corrections (as described in *Wentz*, 2015), and consideration of differences between instruments (e.g., resolution, look angle, etc.). For further details on data processing, the reader is encouraged to visit www.remss.com/measurements/wind/wspd-1-deg-product.

Between 20°S and 70°S, we define the strength of the surface westerly wind jet as the maximum zonal mean wind speed (m/s); westerly jet position is then defined as the latitude (degrees) of this jet maximum (as in *Swart et al.*, 2015).

4.3.3 Climate indices

We use the monthly (June 2002 to February 2014) SAM (or Antarctic Oscillation) and Niño-3.4 ENSO indices obtained from the National Oceanic and Atmospheric Administration (NOAA) Climate Prediction Center (CPC; www.cpc.ncep.noaa.gov). The SAM index is defined as the leading principal component of monthly 700-hPa geopotential height anomalies (south of 20°S) from the National Centers for Environmental Prediction/National Center for Atmospheric Research (NCEP/NCAR) reanalysis. Variations in Niño-3.4 are based on SST anomalies averaged over the 5°N–5°S, 170- s-120°W region.

We standardize the SAM and ENSO indices prior to analysis by removing the long-term mean and dividing by the long-term standard deviation. We correlate and regress detrended data variables (see Section 4.3.1 for anomalous data information) onto the given climate index using the method of *Bretherton et al.* (1999) to test the statistical significance of all reported correlation coefficients in the presence of autocorrelation. We quantify the proportion of trends linearly attributable to the SAM and ENSO by regressing the monthly time series onto the detrended indices and multiplying the resulting regression coefficients by the trend in the index; the residuals (i.e., the components of the trend that cannot be linearly attributed to the given index) are quantified by subtracting the linearly congruent components from the original trends (as outlined in *Thompson et al.*, 2000).

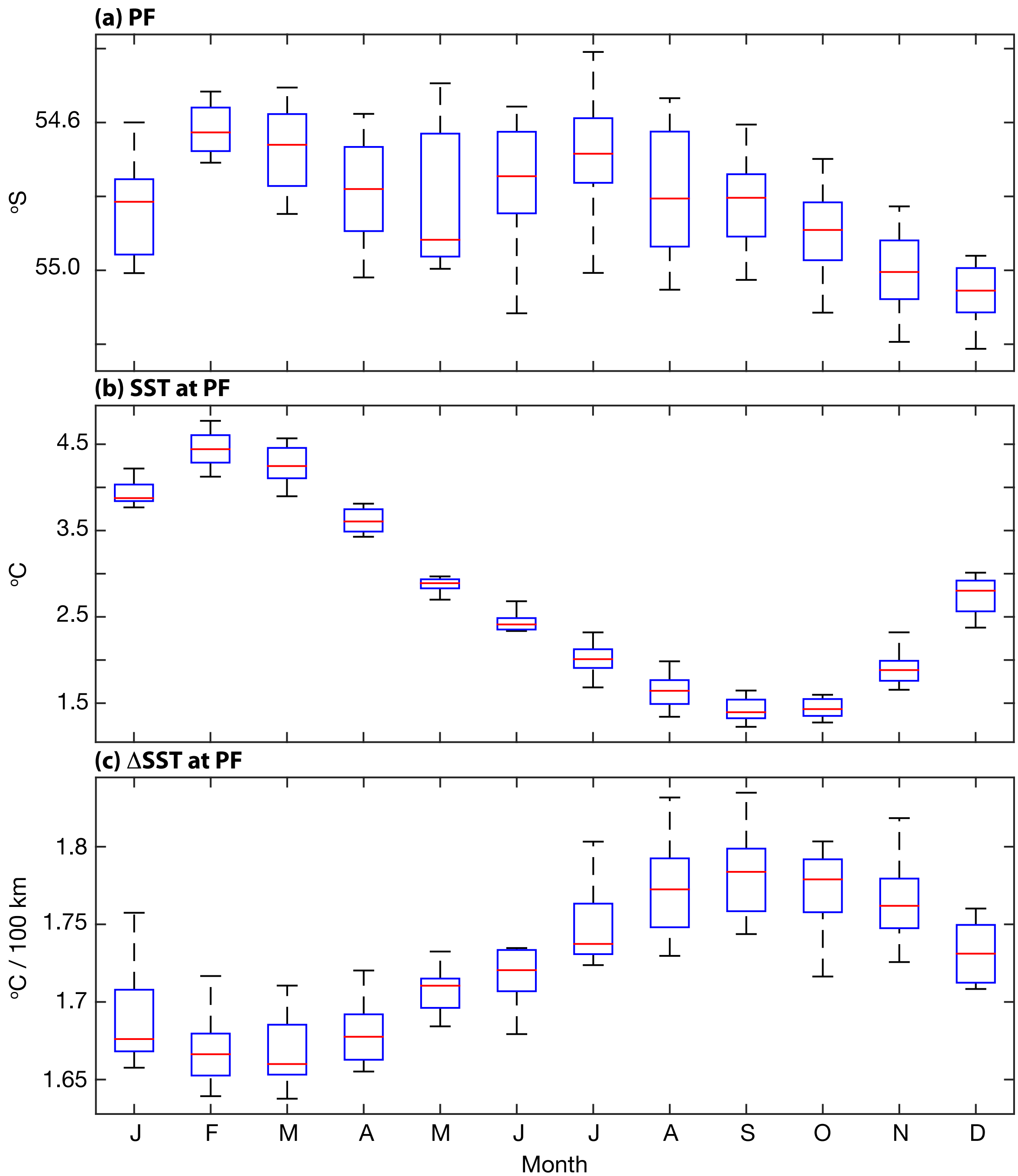

Figure 4.2: The zonal mean (a) Polar Front location and (b) SST and (c) ΔSST at the PF by month from June 2002 to February 2014. Each box indicates the median value (center red line), 25th and 75th percentiles (blue edges), and extreme data points (black whiskers) of the given data variable.

4.4 Results

The climatological mean features of the Antarctic Polar Front are discussed in *Freeman and Lovenduski* (2016a). Figure 4.1a displays the mean PF path (black contour) and its standard deviation (white contours; $\pm 1\sigma$ in the monthly PF) overlain on bottom topography. In general, the latitudinal location of the PF is more northerly in the Atlantic and Indian sectors of the Southern Ocean and more southerly in the Pacific sector. It follows that the SST at the PF is warmer in the Atlantic and Indian sectors and cooler in the Pacific sector (see *Freeman and Lovenduski*, 2016a).

4.4.1 Seasonal variability

We find that the zonally-averaged position of the PF does not exhibit significant seasonality, despite seasonal changes in both the zonal mean SST and ΔSST identified at the PF (Figure 4.2). On average, the front resides in its most equatorward position in both February and July and contracts poleward throughout the spring months. In late austral summer-early autumn, frontal temperatures are the warmest and marked by the weakest gradients (Figure 4.2b,c). Conversely, during late winter-early spring, SSTs are cold and the PF is characterized by strong temperature gradients (Figure 4.2b,c). Indeed, temporal variability in the zonal mean SST at the PF is dominated by the seasonal cycle and varies from ~4.5 °C in February to ~1.5 °C in September. Likewise, temporal variability in the zonal mean ΔSST at the PF is dominated by the seasonal cycle, varying from ~1.78 °C per 100 km in February to ~1.67 °C per 100 km in September. In a zonally-averaged sense, this seasonal behavior is consistent with the findings of *Moore et al.* (1999) and *Dong et al.* (2006a).

Unlike the zonal mean position of the PF, in certain regions of the Southern Ocean the location of the PF is dominated by seasonal variation (Figure 4.3a). During cold season months (winter-spring), the PF has a more northerly position and during warm season months (summer-fall), the PF has a more southerly position, except in the Indian sector

Table 4.1: Mean values and regression and correlation coefficients of the mean time series with the SAM and ENSO index[a]

Variable	Mean Value	Regression Coefficient Associated With $1\sigma_{Index}$		Correlation With Index	
		SAM	ENSO	SAM	ENSO
PF [degrees latitude]	-54.81	-0.27	-0.62	-0.0543	-0.1336
SST at PF [^{o}C][c]	2.71	-1.97	0.93	-0.3517[b]	0.1816
ΔSST at PF [^{o}C/100 km][c]	1.73	-7.51	2.53	-0.1571	0.0581

[a] Regression coefficients correspond to one standard deviation change in the given climate index; significant at the 95% level.
[b] Correlation significant at the 95% level.
[c] Anomalous variable.

(∼90–140°E), where the PF tends to shift north when temperatures are warmer. In the western Pacific, south of New Zealand, the PF shifts equatorward during the cold season and poleward during the warm season. We find that seasonally-dominated regions are characterized by deep ocean depths (Figure 4.3a; e.g., ∼50°E, 120–140°E, 160–180°E, ∼340°E; see Section 4.4.2); here, the winter-spring paths tend to diverge from the summer-fall paths. For example, the amplitude of the seasonal cycle in the mean PF position within the 120–140°E region, characterized by ocean depths of ∼4 km, is 2.1° latitude (∼235 km), exceeding interannual variability (≤120 km standard deviation; Figure 4.1b), suggesting that the seasonal cycle dominates PF variability in this region. In general, the seasonal variability in the PF presented in this study (Figure 4.3a) is relatively small when compared to the differences between the many PF climatological mean positions found in past studies (see Figure 6 of *Freeman and Lovenduski*, 2016a), suggesting that these differences are not the result of seasonal sampling biases.

4.4.2 Interannual variability

We find that interannual variability in the PF path is largely determined by bottom topography, consistent with previous PF studies (*Deacon*, 1937; *Gordon et al.*, 1978; *Chelton et al.*, 1990; *Gille*, 1994; *Moore et al.*, 1999; *Dong et al.*, 2006a; *Sallée et al.*, 2008), most

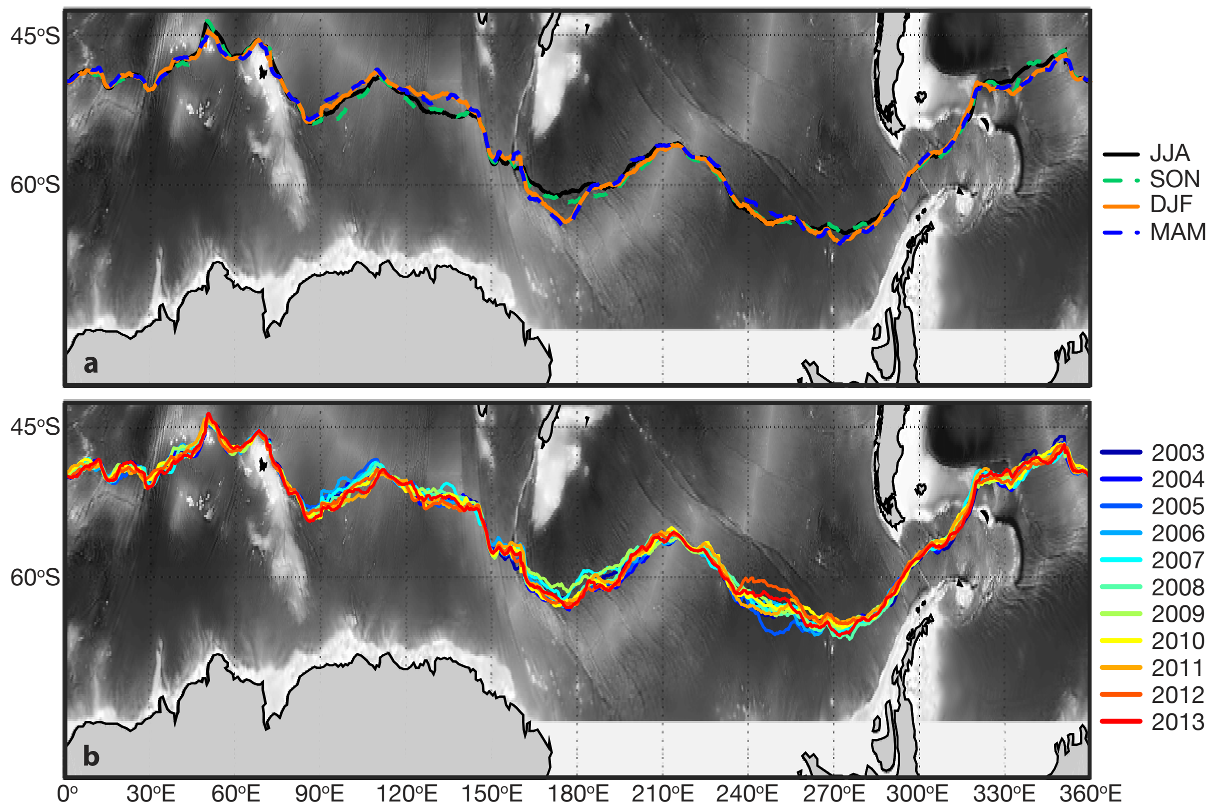

Figure 4.3: (a) Seasonal mean position in the Antarctic Polar Front (June 2002 to February 2014): austral winter (JJA; yellow), spring (SON; blue), summer (DJF; magenta), and fall (MAM; green). (b) Annual mean PF positions (January 2003 to December 2013). Bottom topography (as in Figure 4.1) displayed underneath PF positions in both panels, where light shading indicates shallow bathymetry and dark shading, deep.

notably through Drake Passage, on the lee side of Kerguelen Plateau, and upon crossing major ridge systems (e.g., Pacific-Antarctic, Mid-Atlantic, and Southeast Indian Ridges), where seasonal and interannual variability is minimal (Figures 4.1 and 4.2). Figure 1b demonstrates that the spatial displacement and temperature variation of the PF is largely constrained by bathymetry: over shallow bathymetry, variability in the location of the PF and its temperature is weak and over deep bathymetry, variability in the location and temperature of the PF is strong (Figure 4.1). The standard deviation of the latitudinal position of the PF is (a) significantly correlated with the standard deviation in SST at the PF (0.76), (b) significantly correlated with bottom depth (-0.22), and (c) can be as large as 2.0° over deep regions and as small as 0.19° over shallow regions. This topographic influence on seasonal and interannual variability in the PF path can also be seen in Figures 4.3a and 4.3b, respectively, where we find a greater spread in the seasonal and annual mean position of the PF over regions characterized by weak topographic influence (e.g., 90–110°E and 240–270°E). In these regions of weak topographic influence, previous studies have indicated that fronts tend to be associated with multiple filaments that are often weak (*Sokolov and Rintoul*, 2002; *Graham et al.*, 2012). Since the mapping technique of *Freeman and Lovenduski* (2016a) preferentially selects the southernmost filament in these multi-filament cases, while ensuring spatial and/or thermal continuity, this study tracks only the variability in this filament.

The leading mode of climate variability in the Southern Hemisphere is the Southern Annular Mode (SAM), associated with meridional shifts in the westerlies (e.g., a positive SAM event translates into a poleward shift in the westerly wind jet; *Thompson and Wallace*, 2000). The atmospheric circulation of the Southern Hemisphere is also influenced by the high latitude response to the El Niño-Southern Oscillation (ENSO), associated with anomalous sea level pressure patterns and correlated with various Southern Ocean properties such as sea ice extent, SST, mixed layer depth, and upper-ocean heat content (*Renwick*, 2002; *Sallée et al.*, 2008; *Stephenson et al.*, 2013). To investigate the influence of the SAM on interannual variability in the PF, we regress the monthly, zonal mean PF position, SST and ΔSST at the

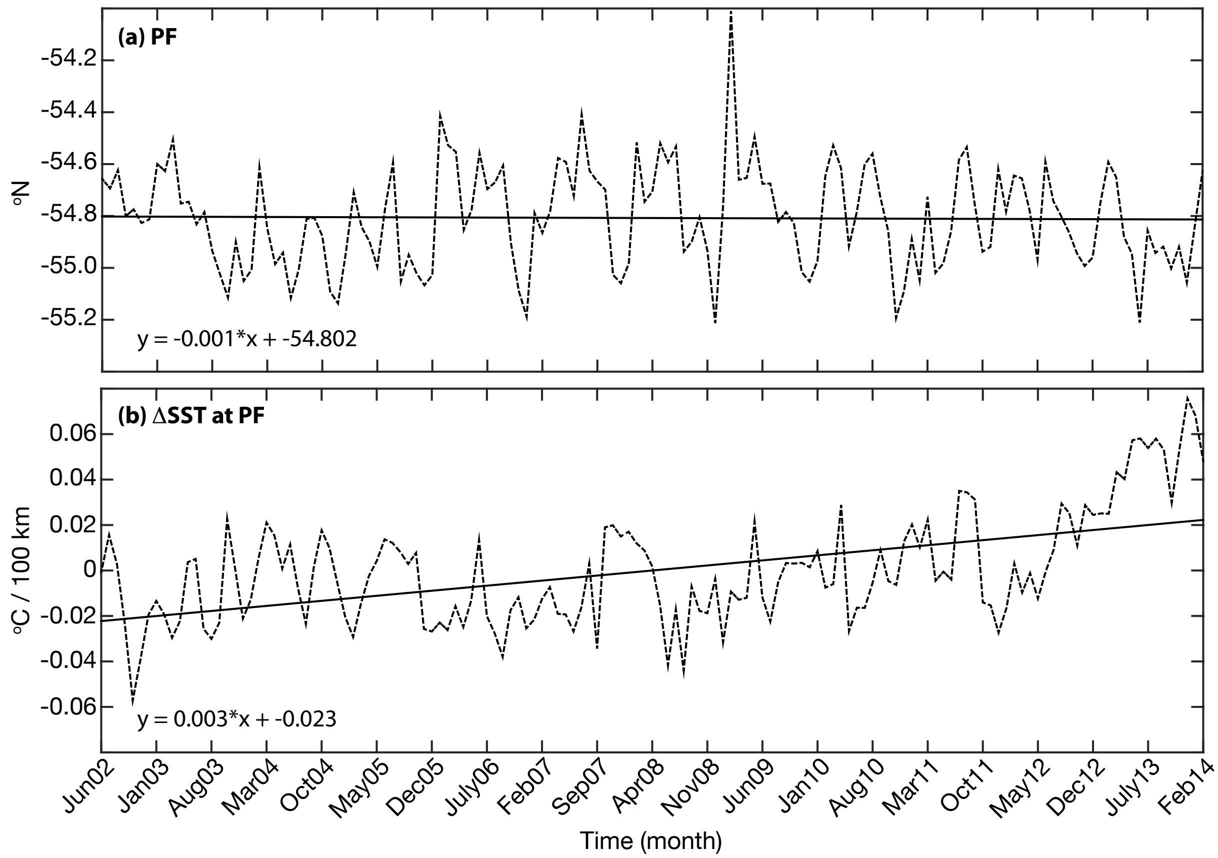

Figure 4.4: Time series of monthly, zonal mean (a) Polar Front position and (b) anomalous SST gradient at the PF (dashed) from June 2002 to February 2014. Fitted linear least squares line (solid) and associated slope-intercept equation indicated; fitted line in (b) is significant at the 95% level.

PF onto the SAM index (see Section 4.3.3), yielding a regression coefficient of -0.27°latitude, -1.97°C, and -7.51°C/100 km per standard deviation change in the index, respectively; see Table 4.1. Similarly, for the influence of the ENSO on interannual variability in the PF, we regress the monthly, zonal mean PF position, SST and ΔSST at the PF onto the ENSO index (see Section 4.3.3), yielding a regression coefficient of -0.62°latitude, 0.93°C, and 2.53°C/100 km per standard deviation change in the index, respectively; see Table 4.1. Therefore, during positive phases of the SAM, we find a cool, weak, and southerly mean PF. During positive ENSO phases, we find a warm, strong, and southerly mean PF. However, in a zonally-averaged sense, the SAM only explains <1% of the monthly variance in the PF, whereas the ENSO explains ∼2%.

4.4.3 Long-term trends

From 2002 to 2014, we find that the trend in the monthly, zonally-averaged PF location is near zero (Figure 4.4a) while the strength of the PF has significantly increased (Figure 4.4b). We assess the sensitivity of these trends to the start and end points of the time series by calculating trends for a range of start and end years (Figure 4.5a,b): start years ranging from 2002 to 2008 and end years ranging from 2007 to 2013. The sign of the PF intensity trends is robust across many start and end year pairs (Figure 4.5b), showing that long-term trends in the strength of the PF are independent of start and end year choices. However, a clear switch from a northward shift in the PF location in the beginning of the time series to a southward shift near the end suggests that the long-term trend in the position of the zonal-mean PF is sensitive to the choice of start and end year (Figure 4.5a).

Figure 4.6a displays the total change in the PF over the study time period across all longitudes. Regional northward and southward shifts emerge, particularly in the Amundsen Sea sector of the Pacific and in the central/east Indian sector, respectively. These regional trends are also evident in Figure 4.3b, demonstrating a clear northward displacement in the annual mean front position in the Pacific sector and a southward displacement in the Indian sector. We investigate PF variability in these sectors by creating regional time series: the Pacific time series is calculated by averaging over 230–260°E and the Indian time series over 75–110°E in order to coincide with the regions of maximum trends. Indeed, we calculate a positive trend (i.e., a northward shift) in frontal position in the Pacific time series and a negative trend (i.e., a southward shift) in the Indian time series over 2002–2014; these statistically significant opposing regional trends combine to produce the near-zero trend in the zonal mean PF (Figure 4.4a). Correlations between the Pacific and Indian time series (not shown) fail to exceed the 95% confidence level, indicating that different processes may be driving PF variability in these two high trend regions. Trends observed in the Pacific and Indian sectors are dominated by trends in the cold season months (winter-spring; not shown).

A previous study has shown that PF variability in the Pacific and Indian sectors is strongly linked to the SAM and ENSO (*Sallée et al.*, 2008). In Section 4.4.2 we demonstrate the influence of these phenomena on interannual variability in the zonally-averaged PF, but find that these relationships are insufficient in explaining long-term trends. In the Pacific and Indian sectors, we find that the proportion of contemporary PF trends that are linearly congruent with the SAM and ENSO is negligible; at most, congruencies peak at <2% and <5%, respectively, and the residual displays magnitudes comparable to the PF trends (not shown; see Section 4.3.3). These congruency analyses were repeated for all seasons for both indices and, in all cases, trends in the two leading patterns of Southern Hemisphere climate variability were unable to account for a significant component of the 2002–2014 trends in PF location in these regions (not shown).

Long-term trends in the monthly mean SST at the PF at every longitude (not shown) reflect large-scale Southern Ocean SST changes: warming in the Atlantic and western Indian basins and cooling in the central/eastern Indian and Pacific basins (Figure 4.7). Despite such regional trends in PF location and SST, the intensity of the PF has increased at nearly all longitudes (Figure 4.6b). We discuss possible mechanisms in Section 4.5.5.

4.5 Discussion

4.5.1 A changing Southern Ocean

Evidence for significant changes in the Southern Ocean has grown in recent years. The Southern Ocean has warmed and freshened (*Gille*, 2002; *Böning et al.*, 2008; *Gille*, 2008; *Cai et al.*, 2010). Glaciers are rapidly melting in West Antarctica where the ACC flows near the continent (*Rignot et al.*, 2008). A recent strengthening of the Southern Ocean carbon sink has been found in two observationally-based studies (*Landschützer et al.*, 2015; *Munro et al.*, 2015a). A trend toward a more positive SAM in austral summer has been identified (see Figure 4.5c), leading to strengthened and more poleward westerly winds (*Thompson et al.*,

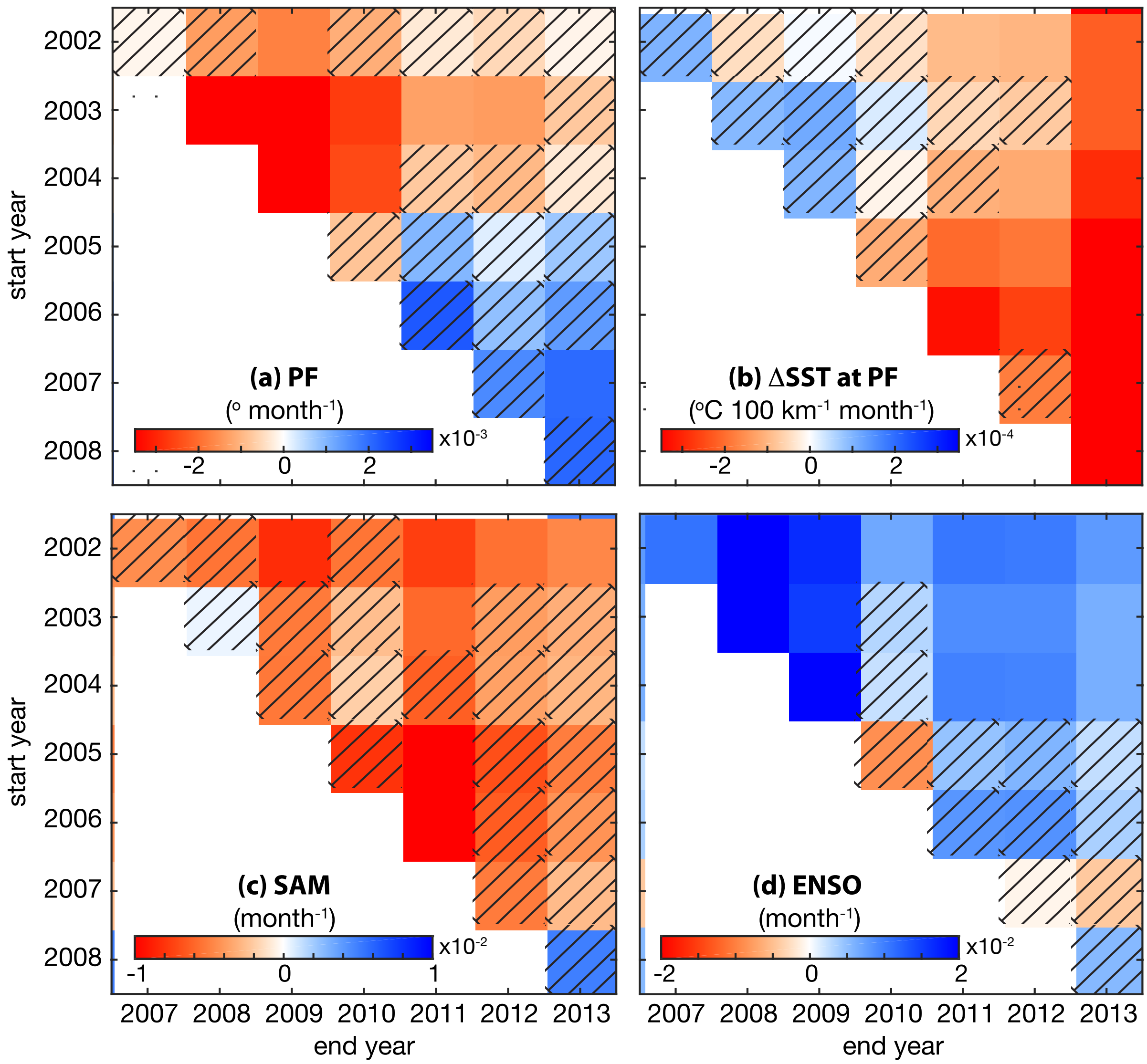

Figure 4.5: Multidecadal trends in monthly, zonal mean (a) Polar Front location and (b) SST gradient at the PF and monthly (c) SAM and (d) ENSO indices. Color indicates the sign of the slope of the fitted trend line (in a least squares sense) for each start and end year pair; trends not significant at the 95% level are hatched.

2000; *Thompson and Wallace*, 2001; *Marshall*, 2003; *Thompson et al.*, 2011). How the ACC, including its fronts, will respond to future Southern Hemisphere changes is an important question. Some climate models project a continued poleward shift in the westerlies over the next century (*Thompson et al.*, 2011; *Swart and Fyfe*, 2012; *Meijers*, 2014) and for the ACC system to mirror them (*Fyfe and Saenko*, 2006). However, the combined role of topography, wind, and large-scale climate modes impacting individual ACC fronts both observationally and from a modeling standpoint is an active area of research.

A large portion of the net warming observed in the Southern Ocean has occurred within the circumpolar band of the ACC (*Gille*, 2008); multiple studies argue that this concentrated warming is consistent with a southward shift in the ACC itself (*Aoki et al.*, 2003; *Sprintall*, 2008; *Gille*, 2008; *Morrow et al.*, 2008). Alternatively, a warming ACC could result from changes in meridional heat transport (e.g., eddy or surface heat fluxes) and not necessarily from a shift in its position, as suggested by *Gille* (2014). *Gille* (2014) finds no long-term meridional displacement in the zonally-averaged latitude of ACC transport, based on analysis of data that are independent of large-scale steric temperature changes. Before our study, the variability and long-term change in the location of the PF within the ACC over this time period of Southern Ocean change was unknown; more specifically, a PF determined without the influence of steric sea level change (see Section 4.3.1), as in *Sallée et al.* (2008), *Sokolov and Rintoul* (2009a), and *Kim and Orsi* (2014). In contrast to such SSH-contour based measures of PF variability, our study finds no significant meridional displacement in the zonally-averaged PF over 2002 to 2014.

4.5.2 Topographic influence on the Polar Front

We find a strong relationship between the PF and the underlying bathymetry, a relationship that has been documented frequently and consistently (*Deacon*, 1937; *Gordon et al.*, 1978; *Chelton et al.*, 1990; *Gille*, 1994; *Moore et al.*, 1999; *Dong et al.*, 2006a; *Sokolov and Rintoul*, 2007a; *Sallée et al.*, 2008). *Moore et al.* (1999) and *Sallée et al.* (2008) suggest that the

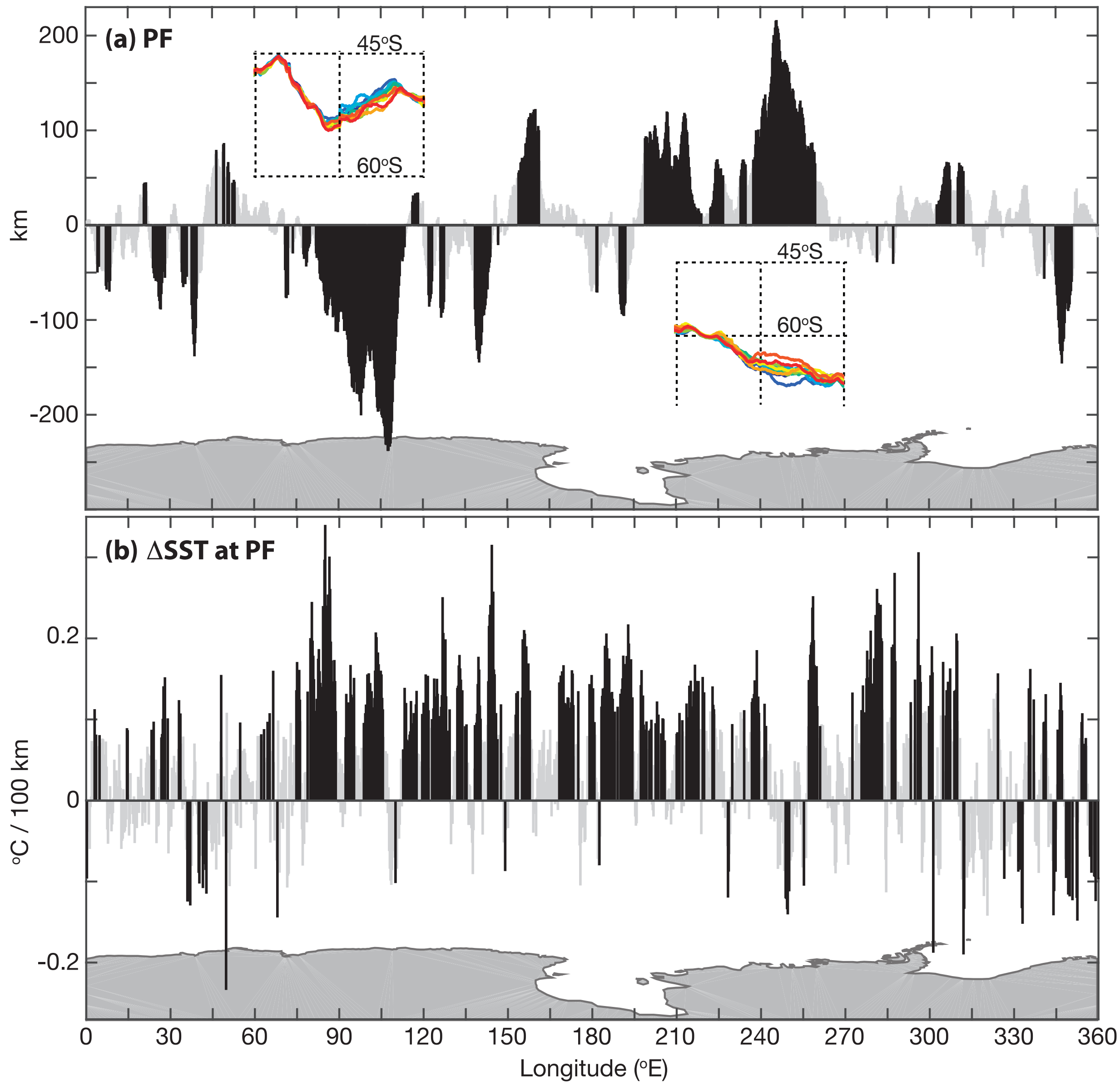

Figure 4.6: Total (a) shift in monthly mean PF location (positive - northward) and (b) change in monthly mean PF intensity (positive - intensified) from June 2002 to February 2014 at every longitude (25 km resolution; black bars indicate significance at the 95% level). Subset plots in (a) are a replication of Figure 4.3b.

position and intensity of the PF are correlated with bathymetry. In order to conserve the barotropic potential vorticity (PV; f/h) in the presence of variable ocean depth (h), the front is steered to a particular latitudinal location (particular value of f), leading to restricted spatial variability. For example, at the shallow Kerguelen Plateau, the PF tends to shift northward to try to conserve PV. Despite this evidence, the extent to which topography determines and controls the PF is still a topic of debate. *Sokolov and Rintoul* (2009a) shed light on the common misconception regarding topographic steering: while it is accepted that topographic features (i.e., plateaus and ridges) inhibit interannual variability in the PF, this does not necessarily mean that, in the presence of sufficiently strong forcing, the PF cannot shift meridionally in these regions over time.

4.5.3 Role of wind

Some studies suggest that away from steep topographic features, where the PF is free to vary across a wide latitudinal range (see Sections 4.4.1 and 4.4.2), changes in the wind field determine its meridional movements (*Howard and Prell*, 1992; *Sokolov and Rintoul*, 2007a, 2009b; *Dong et al.*, 2006a; *Sallée et al.*, 2008; *Kemp et al.*, 2010). From a modeling perspective, a change in the position of the overlying surface wind stress has been understood to induce changes in ACC position (*Hall and Visbeck*, 2002; *Oke and England*, 2004). However, the more recent climate change simulations of *Graham et al.* (2012) show that in response to a change in wind-forcing, and in the absence of strong topographic influence (i.e., over flat topography), the location of the PF exhibits significant seasonal variability with little to no long-term meridional displacement, further suggesting that its position within the ACC is not directly controlled by the overlying winds.

In this study, we find a near-zero meridional displacement in both the zonal-mean position of the PF (Figure 4.4a) and westerly jet (not shown) over the study time period, while both the zonal-mean strength of the PF (Figure 4.4b) and westerly jet (not shown) have increased. Swart et al. [2015] also find a near-zero trend in annual mean jet position in six wind reanalysis products over their 30-year study period between 1979 and 2009. In the Indian sector (75–110°E), a region exhibiting seasonal variability (Section 4.4.1), we find a significant southward displacement in the PF (Figure 4.6a) and a concurrent decrease in monthly wind speed (not shown). Furthermore, we find a weak positive correlation (r = 0.19) between monthly wind speed and PF position in the Indian sector, which suggests that wind may play a small role in determining PF position in this region of weak topographic influence. In the Pacific sector (230–260°E), a region also exhibiting seasonal variability (Section 4.4.1), we find a significant northward shift in the PF (Figure 4.6a) and a concurrent increase in monthly wind speed north of the climatological mean PF position and decrease in monthly wind speed south of the climatological mean PF position (not shown). However, we also find a weak positive correlation (r = 0.03) between monthly wind speed and PF position in the Pacific sector.

4.5.4 Climate variability impacts

Large-scale climate modes have also been linked to regional variability and trends in the PF, particularly over flat-bottom areas (*Sallée et al.*, 2008). The modeling studies of *Hall and Visbeck* (2002) and *Sen Gupta and England* (2006) reveal that the wind changes associated with a positive SAM force a southward annular shift of the ACC system, inconsistent with the observed regional responses presented in *Sallée et al.* (2008) which highlight more spatially inhomogeneous frontal variability patterns. Indeed, *Sallée et al.* (2008) show that the SAM dominates PF displacements on short timescales (<3 months), where the latitude of the PF is positively correlated in the Pacific and anti-correlated in the Indian Ocean (i.e., a positive SAM event is associated with a poleward shift in the PF in the Indian sector); on longer timescales (>1 year), the latitude of the PF is anti-correlated with ENSO. This study finds the regional response of the PF to ENSO in the Indo-Pacific sector (110–220°E) to be consistent with that of *Sallée et al.* (2008): a positive ENSO event is associated with a poleward shift in the PF (r = -0.27, p = 0.00). However, we find weak and insignificant

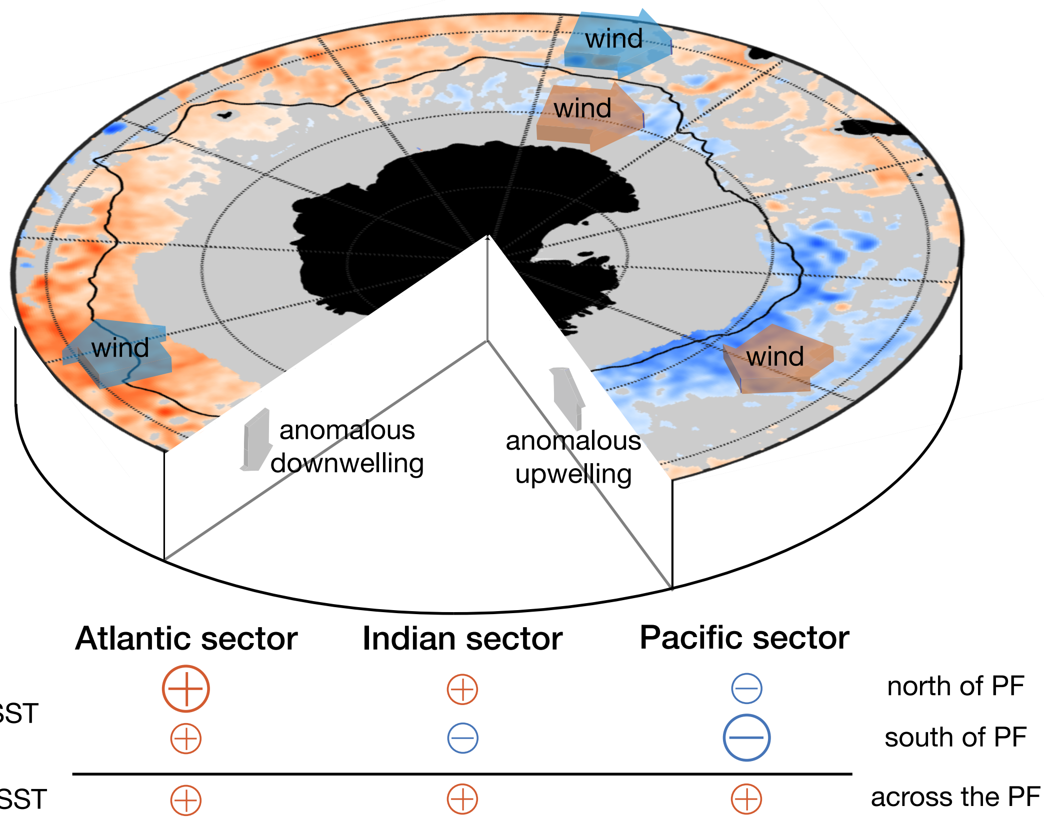

Figure 4.7: Schematic depicting the processes associated with basin-wide frontal intensification since 2002. Stereographic image: the linear trend in monthly microwave SST anomalies from June 2002 to February 2014. The black contour indicates the mean position of the PF. Surface arrows depict changes in the surface wind field over this same period of time. Red colors indicate an increase in SST or surface wind and blue colors indicate a decrease in SST or surface wind over the study time period. Subsurface arrows depict response to changes in surface wind. Figure adapted and modified from *Landschützer et al.* (2015).

correlations between the position of the PF and the SAM or ENSO indices in their other focus regions; we note that a direct comparison of our results to those of *Sallée et al.* (2008) is hindered by different PF definitions.

4.5.5 Widespread frontal intensification

We have demonstrated that while the zonal-mean position of the PF has not shifted, the front has become more intense across all longitudes during our study period. Previous studies have shown that the atmospheric circulation of the Southern Hemisphere has become increasingly asymmetric since the early 2000s, with conditions more cyclonically dominant in the Pacific sector and more anti-cyclonically dominant in the Atlantic and parts of the Indian sector. Concurrently, anthropogenic forcing (e.g., stratospheric ozone depletion and greenhouse gas increases) is driving surface circulation changes that vary by region (*Haumann et al.*, 2014). Therefore, the widespread PF intensification we observe in this study is likely driven by regional changes in temperature and wind, perhaps as a result of this increased asymmetry.

In the Atlantic sector, SSTs have increased more north of the PF and less south of the PF (Figure 4.7), resulting in an increased SST gradient at the PF over this time period. We find that the strength of the westerly winds and the associated westerly jet have weakened here over this time period (Figure 4.7), resulting in less Ekman drift; the westerlies drive northward Ekman transport, associated with convergence and downwelling to the north and divergence and upwelling to the south of the maximum wind stress. As a result of the zonally asymmetric atmospheric circulation described above, the Atlantic has experienced surface warming, likely attributed to (1) a reduction in Ekman transport of cold, high-latitude waters to the north (i.e., anomalous downwelling or reduced upwelling; Figure 4.7; *Landschützer et al.*, 2015) and (2) increased meridional winds that anomalously advect warm air from the subtropics over the basin, providing surface heating from the atmosphere. Therefore, frontal intensification observed in the Atlantic sector is likely attributed to the thermal response of a more zonally asymmetric atmospheric circulation and a weaker westerly jet.

In the Pacific sector (defined ∼210–270°E), SSTs have decreased more south of the PF and less north of the PF (Figure 4.7), resulting in an intensification of the PF since 2002. The observed surface cooling trend in the Pacific can be explained by the more asymmetric atmospheric circulation. Here, increased meridional winds, under a more cyclonically dominant pressure system, act to anomalously advect cold air from the Antarctic continent over the basin; changes in sea ice have likely enhanced this surface cooling trend (*Landschützer et al.*, 2015; *Haumann et al.*, 2014). In addition, increased westerly winds over the South Pacific suggest enhanced northward Ekman transport (i.e., increased upwelling near the Antarctic continent; Figure 4.7; *Landschützer et al.*, 2015). Taken together, we speculate that the frontal intensification observed in the Pacific sector over this time period is attributed to the thermal response of a more zonally asymmetric atmospheric circulation and stronger westerly winds.

The Indian sector exhibits a relatively weaker signal as compared to the Atlantic and Pacific sectors; the relationship between the zonal wind component and SST appears to dominate the Indian sector, whereas the meridional wind component played a bigger role in the other two sectors (see above). Indeed, the mean westerly jet position coincides with the mean position of the PF. Assuming no significant change in wind direction, in the Indian sector, winds have increasedand SSTs have cooled south of the PF (Figure 4.7), due to increased vertical mixing in the upper ocean. Conversely, winds have decreased and SSTs have warmed north of the PF (Figure 4.7), due to decreased vertical mixing in the upper ocean. Therefore, we attribute frontal intensification throughout the Indian sector of the Southern Ocean to changes in the strength of the westerly winds.

4.5.6 The Polar Front on glacial-interglacial timescales

Reconstructing the position of the PF in past climates is a challenging but important step toward improving our understanding and modeling of glacial-interglacial changes in the climate system and to infer details about the paleo position of the westerlies (*Ho et al.*, 2012;

De Deckker et al., 2012; *Kohfeld et al.*, 2013). PF locations in the paleo record have been identified using water mass properties, but the relative paucity of data available from deep sea cores makes difficult the detection of finer frontal features (e.g., paleo SST gradients). To circumvent these challenges, these methods assume that the SST at the PF is relatively constant in both space and time (*Howard and Prell*, 1992), yet this study shows that SST varies considerably both spatially and seasonally along the modern-day PF (see also *Kostianoy et al.*, 2004).

Past locations of the PF have also been reconstructed using sedimentary records. Generally, the PF marks the divide between waters replete with silicic acid (*Sarmiento et al.*, 2004) and thus supportive of diatom (opal) productivity, and waters devoid of silicic acid. As such, sedimentary opal tests have been used to demarcate the location of the PF and to infer changes in silicic acid supply and diatom productivity on glacial-interglacial timescales (*Anderson et al.*, 2009; *Kemp et al.*, 2010). While it is generally agreed that changes in sediment composition occurred in the vicinity of the PF during glacial-interglacial cycles, whether the PF has migrated on these timescales is still an open question (see *Kemp et al.* (2010) and references therein). This uncertainty highlights a need to further investigate the relationship between the PF and biogeography in the modern-day Southern Ocean (e.g., *Chase et al.*, 2015).

4.6 Conclusions

We quantify the temporal variability in the Antarctic Polar Front using a high-resolution PF data set derived from gradients in the microwave SST record (2002–2014; *Freeman and Lovenduski*, 2016b). Microwave SSTs provide an unimpeded look at the cloudy Southern Ocean and thus allow for the continuous tracking and study of the PF over the past 12 years and, with continued retrievals, the opportunity to extend the PF time series into the future.

In summary, this study finds that the location and intensity of the PF is influenced by bathymetry, acting to reduce its spatial extent and temporal variability over shallow bathymetry. In most locations across the basin, the latitudinal position and intensity of the PF does not vary seasonally yet its temperature exhibits a clear seasonal cycle. From 2002 to 2014, the PF intensifies at nearly all longitudes and two regions of the Southern Ocean experience substantial latitudinal displacements ($\sim$200 km): a northward shift in the Pacific sector and a southward shift in the Indian sector. We have investigated the role of SAM and ENSO, the two most dominant modes of large-scale climate variability in the Southern Hemisphere, on the characteristics of the PF and find weak correlations with both phenomena. In zonal average, the PF intensifies with no discernible meridional shift; this basin-wide intensification is possibly a result of observed changes in the westerly wind field and a more zonally asymmetric atmospheric circulation since 2002.

Acknowledgments

Weekly PF realizations are available at doi.pangaea.de/10.1594/PANGAEA.855640. Microwave OI SST data are produced by Remote Sensing Systems and sponsored by National Oceanographic Partnership Program (NOPP) and the NASA Earth Science Physical Oceanography Program; data available at www.remss.com. Microwave radiometer wind speed data processed by Remote Sensing Systems with funding from the NASA MEaSUREs Program and from the NASA Earth Science Physical Oceanography Program; data available at www.remss.com. This study was supported by NSF (PLR-1543457; OCE-1258995; OCE-1155240) and NOAA (NA12OAR4310058); NCAR is funded by NSF.

Chapter 5

Present and projected variability of the Southern Ocean Silicate Front: Insights from the CESM Large Ensemble

5.1 Abstract

The location of the Southern Ocean Silicate Front (SF) is a key indicator of physical circulation, biological productivity, and biogeography but its variability in space and time is currently not well understood due to a lack of time-varying nutrient observations here. This study provides a first estimate of the spatio-temporal variability in the SF, defined using the silicate-to-nitrate ratio (Si:N) as simulated by the Community Earth System Model Large Ensemble (CESM-LE; 1920–2100). The latitude where Si:N is equivalent largely coincides with regions of high gradients in silicate and the observed location of the Antarctic Polar Front (PF), and serves as an approximate indicator of the molar ratio at which diatoms use these nutrients. We find that much like the observed interannual variability in the PF, the

underlying bathymetry of the basin largely determines the position of the SF on interdecadal timescales, with low interdecadal variability over shallow bathymetry. This study also provides a first look at the impact of a changing Southern Ocean on large-scale biogeochemical fronts. From 1920 to 2100, under historical and RCP 8.5 forcing, the zonally-averaged SF shifts meridionally by nearly 3° latitude toward the Antarctic continent. Consistently across the basin, by the 2090s, the SF is found further south than its present-day position, primarily driven by long-term reductions in silicate and nitrate concentration at the surface as a consequence of a warmer, more stratified Southern Ocean. Long-term displacements in the SF have implications for local biogeography, global thermocline nutrient cycling, and the interpretation of paleoclimate records from deep sea sediments.

5.2 Introduction

The Antarctic Circumpolar Current (ACC) system of the Southern Ocean is made up of many dynamically and biogeochemically distinct regions due to the presence of hydrographic fronts and geostrophic jets (*Deacon*, 1937, 1982; *Orsi et al.*, 1995; *Belkin and Gordon*, 1996; *Moore et al.*, 1999; *Pollard et al.*, 2002; *Dong et al.*, 2006a; *Sokolov and Rintoul*, 2009a,b; *Freeman et al.*, 2016). ACC fronts are characterized by strong lateral property gradients (e.g., temperature, salinity) set up by sloping density surfaces. Fronts of biogeochemically important properties often coincide with ACC fronts and jets, owing to the ocean's biological pump which effectively transports biogeochemical properties (e.g., nutrients, oxygen, carbon) from low-density surface waters to denser waters at depth. Across biogeochemical fronts, mixing and advection supply nutrients to the euphotic zone, directly influencing local primary production; indeed, elevated concentrations of satellite-derived chlorophyll-a and calcite are found to be coincident with hydrographic and biogeochemical fronts (*Moore and Abbott*, 2000; *Balch et al.*, 2016). Despite the Southern Ocean being one of the three large high-nutrient, low-chlorophyll (HNLC) areas of the World Ocean, ACC fronts provide a location

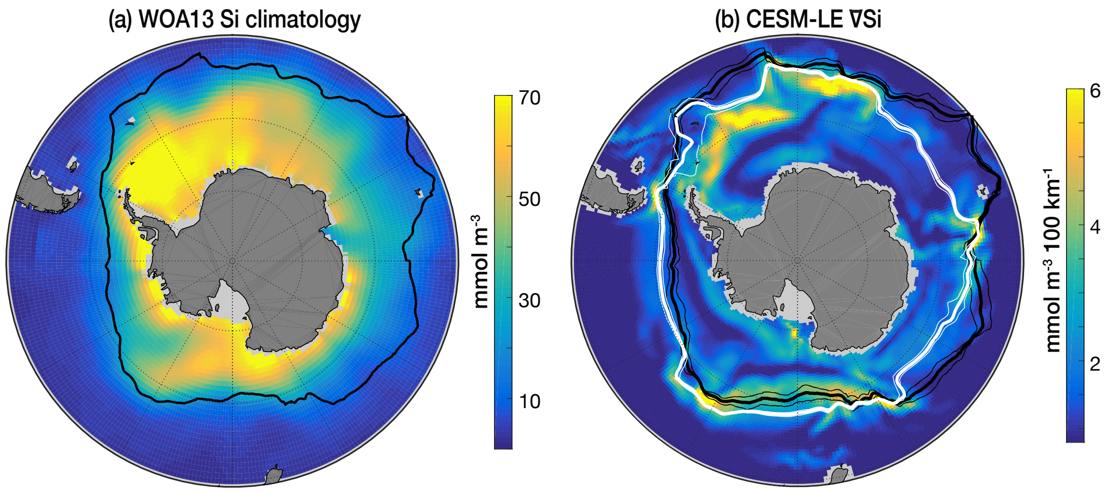

Figure 5.1: (a) Climatological mean surface silicate concentration from the World Ocean Atlas Database (colors; *Boyer et al.*, 2013). The black contour indicates the climatological mean position of the Polar Front (*Freeman and Lovenduski*, 2016a). (b) From 2002 to 2014, CESM-LE simulated Si gradients (colors), the observed mean (black, thick) position of the Polar Front and its standard deviation (black, thin; *Freeman and Lovenduski*, 2016a), and the mean latitude where simulated Si:N = 1 (white, thick) and its standard deviation (white, thin).

where nutrients return from depth to the pycnocline (*Sarmiento et al.*, 2004; *Marinov et al.*, 2006; *Sokolov and Rintoul*, 2007b; *Palter et al.*, 2010).

In particular, the Antarctic Polar Front (PF) of the ACC is a region of marked enhanced phytoplankton biomass, with frequent bloom events in austral spring and summer (*Smetacek et al.*, 1997). Physically, the PF is both a subduction and transition zone: here, cold, fresh Antarctic waters subduct beneath warmer, saltier sub-Antarctic waters and from south to north across the PF, stratification transitions from a salinity-dominated regime to an increasingly temperature-dominated regime, respectively (*Pollard et al.*, 2002). Biogeochemically, the PF marks the boundary between silicate-rich and silicate-poor waters (Figure 5.1; *Sarmiento et al.*, 2004), a distinction important to diatoms, the dominant phytoplankton that require silicic acid (Si) to produce and maintain their indispensable silica frustules. The westerly winds drive the upwelling and mixing of Si-rich Upper Circumpolar Deep Water (UCDW) south of the PF, and as a portion of this UCDW travels northward across the PF through Ekman transport, diatoms strip the available Si, effectively setting up the Southern

Ocean Silicate Front (SF). Therefore, the PF and its associated SF is regarded as important in terms of the biogeography of the Southern Ocean (i.e., the geographic distribution of diatoms vs. non-siliceous phytoplankton).

As such, the Southern Ocean is not only regarded as a major carbon sink (e.g., *Munro et al.*, 2015a), but an important silica sink (*Pondaven et al.*, 2000; *DeMaster*, 2002). The Si-rich waters south of the PF support high diatom abundance and biogenic silica (i.e., opal) production. The resulting high export production out of the surface and ultimately, the burial of opal in abyssal sediments, contribute to the Southern Ocean Opal Belt of siliceous sediments that ring the Antarctic, roughly mirroring the surface PF zone (*DeMaster*, 1981, 2002). The Si left unused at the surface, driven by iron (Fe) limitation (e.g., *Sarthou et al.*, 2005), is subsequently exported to the rest of the World Ocean through mode, intermediate, and deep water formation (see *Tréguer*, 2014).

Diatoms play a critical role in marine ecology and the global carbon cycle by exporting organic carbon and sequestering Si to the deep ocean and sediments, thereby impacting nutrient cycling and atmospheric carbon dioxide concentrations (*Falkowski et al.*, 1998; *Smetacek*, 1999). Under sufficient light and nutrient conditions, the Si demand of most diatoms is equivalent to that for nitrate (N), i.e., a Si:N depletion ratio of 1 (see Section 5.5). The latitude in the Southern Ocean where Si:N = 1 can be used as a spatial indicator of the status of diatom nutrient requirements (e.g., north of this latitude, diatoms are more likely to experience Si limitation). In most regions of the Southern Ocean, this latitude also coincides with high absolute gradients in simulated Si and the observed PF (Figure 5.1b; see Section 5.3). We therefore define the persistent, large-scale Southern Ocean SF as this latitude, where Si:N = 1, in order to track its variability in space and time and quantify long-term change using a state-of-the-art coupled climate model.

5.3 Data and Methods

We define the Southern Ocean poleward of 44°S. We define the absolute gradient in a variable V as,

$$|\nabla V| = \sqrt{(\delta V/\delta x)^2 + (\delta V/\delta y)^2},$$

where δV is the unit difference in the variable and δx and δy are the kilometer distances between any two longitude or latitude points, respectively. As in *Freeman and Lovenduski* (2016a), we refer to the gradient identified at a front as the intensity or strength of that front (e.g., the absolute Si gradient at the SF, $|\nabla \mathrm{Si}|$, is an indication of the strength of the SF).

5.3.1 Model description

We investigate intraannual to interannual variability and long-term change in the Southern Ocean SF by using monthly output from the Community Earth System Model Large Ensemble (CESM-LE) simulations (described in detail in *Kay et al.*, 2015). In short, CESM version 1 (CESM1) is a state-of-the-art coupled climate model run with atmosphere, ocean (nominal 1° horizontal resolution and 60 vertical levels), land, and sea ice components (*Hurrell et al.*, 2013; *Smith et al.*, 2010; *Danabasoglu et al.*, 2012; *Hunke and Lipscomb*, 2008).

The biogeochemical component has three explicit phytoplankton functional types (PFTs; *Moore et al.*, 2004, 2013), a dynamic iron cycle (*Doney et al.*, 2006; *Moore and Bracuher*, 2008), full carbonate system thermodynamics, and allows for multi-nutrient co-limitation. The three PFTs are small phytoplankton, diatoms, and diazotrophs (*Moore et al.*, 2004, 2013; *Kay et al.*, 2015; *Lovenduski et al.*, 2016); as this study focuses solely on the Southern Ocean, our investigation is limited to small phytoplankton and diatom PFTs. Each PFT has a maximum growth rate that is scaled directly by a temperature function (with a Q10 of 2.0 and a reference temperature of 30°C) and is further attenuated by light and nutrient limitation. Zooplankton grazing can also affect these PFTs, with grazing rates increasing with temperature. In general, given the prescribed model parameterizations, diatoms are more productive in cooler, high-nutrient conditions (e.g., south of the PF, SF), while small phytoplankton are more productive in warmer, low-nutrient conditions (owing to smaller half-saturation constants for nutrient uptake) and experience higher grazing pressure than diatoms.

CESM-LE included a control integration (>2,000 years) and 32 ensemble members with ocean biogeochemistry output (*Kay et al.*, 2015; *Lovenduski et al.*, 2016). A great advantage to using a large ensemble of a single Earth System Model (ESM) is the ability to isolate and investigate internal (i.e., natural) climate variability without the effects of model structural uncertainty (e.g., when using the CMIP5 model simulations; see *Lovenduski et al.*, 2016). Atmospheric CO_2 concentrations are prescribed in the CESM-LE and all ensemble members have identical external forcing: historical forcing from 1920 to 2005 and RCP 8.5 forcing from 2006 to 2100. Beginning from an 1850 control simulation with constant preindustrial forcing, the first ensemble member (EM001) was initialized from a randomly selected year (402) of the control and integrated forward in time to 2100. The remaining ensemble members were then integrated from 1920 to 2100 using initial conditions from EM001 at 1920 but with added minute ($\mathcal{O}(10^{-14})$ K) perturbations in initial air temperature; since each ensemble member simulation is identically forced, such perturbations result in different natural (internal) climate variability across members. Therefore, the ensemble mean of any simulated variable is a representation of the long-term, forced trend, while variance across members can be attributed to the influence of internal climate variability on that variable.

For a given month and desired depth level, ensemble mean values of simulated variables were computed by averaging across ensemble members. Decadal averages of simulated variables were computed for present day conditions (2000–2009; referred to as 2000s) and future conditions (2090–2099; referred to as 2090s) for each ensemble member and for the ensemble mean. Here, we report long-term change in the ensemble mean as epoch differences between the present-day and future (2090s − 2000s) and use variation across the ensemble members to evaluate where these changes are robust: statistical significance of long-term change is defined herein as any location where the ensemble mean epoch difference exceeds one standard deviation of the differences across ensemble members (i.e., where the signal-to-noise ratio exceeds one). We define sea ice extent as the northernmost grid point where sea ice fraction exceeds 0.01. We define stratification as the density difference between the surface and 200 m. We quantify model drift by isolating model years (552–652) corresponding to transient years (2000–2100) and computing the future–present epoch difference; model drift in Si at the surface (-0.6037 mmol m^{-3}) is an order of magnitude smaller than the reported long-term change in Si and is therefore deemed negligible.

To provide context for the CESM-LE results, we examine a single integration (1920–2100) from a small group of models from the Coupled Model Intercomparison Project, phase 5 (CMIP5; *Taylor et al.*, 2012): the MPI-ESM-LR from the Max Planck Institute (MPI; *Giorgetta et al.*, 2013), GFDL-ESM2M from the Geophysical Fluid Dynamics Laboratory (GFDL; *Dunne et al.*, 2012, 2013), and HadGEM2-ES from the UK Met Office Hadley Centre (*Collins et al.*, 2011; *HadGEM2 Development Team*, 2011). Just as in CESM-LE, historical forcing was applied through 2005, followed by RCP 8.5 forcing through 2100.

5.3.2 Observations

Observationally-based Si distributions are taken from the World Ocean Atlas 2013 Database (WOA13; *Boyer et al.*, 2013; *Garcia et al.*, 2014). The climatological annual mean field used herein (Figure 5.1a) represents all silicate data collected since the early 1900s interpolated to standard depth levels (102 total) onto a 1 degree latitude/longitude grid (using 4-point Reiniger-Ross, 3-point Lagrangian, or linear interpolation schemes).

Freeman and Lovenduski (2016a) map the weekly location of the PF from 2002 to 2014, inferred from gradient maxima in sea surface temperature (SST) estimated from cloud-penetrating microwave radiometers at 25 km (for a detailed description of their mapping technique, see *Freeman and Lovenduski*, 2016a). In this study, weekly PF data (*Freeman* *and Lovenduski*, 2016b) retain 1/4° spatial resolution and the climatological mean position is computed by averaging over all available data (2002–2014; Figure 5.1).

5.4 Results

5.4.1 Mean state

Figure 5.2a shows the ensemble mean Si:N ratio in the surface layer of the CESM-LE. The climatological path of the surface SF is zonally asymmetric, traversing ∼12° of latitude from its northernmost position along the Mid-Atlantic Ridge (49.41°S) to its southernmost position in the southeast Pacific (61.47°S; Figure 5.2a). The climatological Si concentration along the SF ranges from 16.27 to 21.14 mmol m^{-3}. The climatological intensity of the surface SF ranges from 1.03 mmol m^{-3} 100 km^{-1} southwest of Kerguelen, a region characterized by deep bathymetry, to 8.57 mmol m^{-3} 100 km^{-1} across the Pacific-Antarctic Ridge, a region characterized by shallow bathymetry (see Section 5.4.3); averaged over all longitudes, SF intensity is 2.91 mmol m^{-3} 100 km^{-1}.

Figure 5.2b highlights the Southern Ocean Si cycle: even in the upper 200 m, Si is found to be enriched at depth (consistent with WOA13; not shown), relative to N (high S:N ratio at depth), reflecting the vertical segregation of organic matter remineralization and opal dissolution (as suggested by *Broecker and Peng*, 1982). As such, the subsurface SF, located at 200 m depth, is consistently found to the north of the surface expression, with largest latitudinal differences found in the Scotia Sea sector and smallest differences found in regions characterized by shallow bottom depths (Figure 5.2a; see Section 5.4.3).

5.4.2 Seasonal variability

We find that the zonal mean position and intensity of the surface SF and its associated Si concentration exhibits a clear seasonal cycle (Figure 5.3). Here, we focus on the seasonality of the zonally averaged SF and its characteristics over a present-day period (2000s; decadal

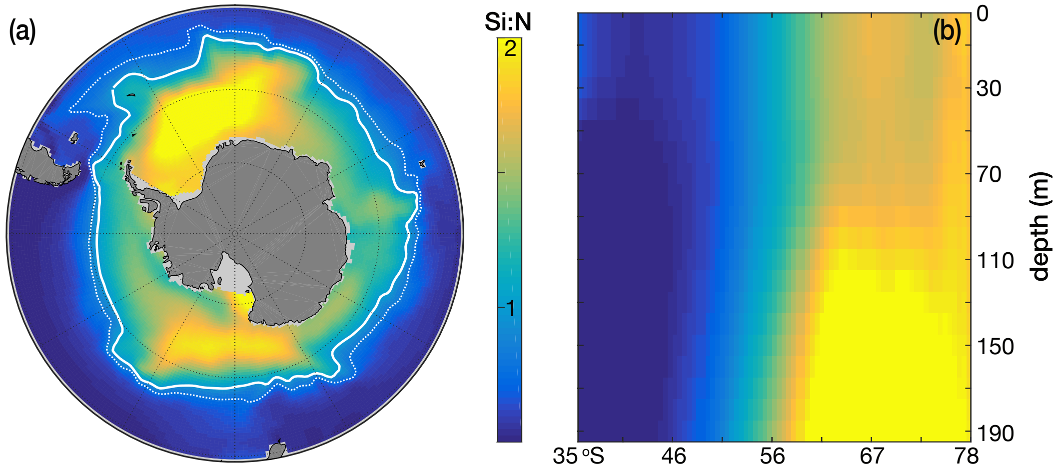

Figure 5.2: (a) Climatological mean (1920–2100) CESM-LE simulated Si:N ratio at the surface (colors); the white contours indicate the latitude where this ratio is equivalent at the surface (solid) and at 200 m (dashed). (b) Climatological (1920-2100), zonally-averaged Si:N ratio in the upper 200 m.

average over 2000–2009) in order to avoid artificial suppression of seasonal variability due to the long-term, externally-forced trend (see Section 5.4.4). The SF resides in its most northerly position in January and September and its most southerly position during austral autumn (MAM; Figure 5.3a). In late summer-early autumn, the SF contracts poleward, reflecting the seasonal drawdown of Si by diatoms, followed by an expansion northward during the winter months (JJA), reflecting a return supply of Si from below. Indeed, Si concentrations found at the SF are largest in late winter-early spring and smallest in late summer-early winter (Figure 5.3b). During this poleward contraction, first, the SF intensifies, characterized by its strongest gradients in February, closely followed by a weakening, characterized by its weakest gradients in April (Figure 5.3c). In general, the mixed layer depth (MLD) at the zonal mean SF shoals in early-mid summer and deepens from February to September while the SST characterizing the SF is warmest in summer and coolest throughout the late winter-early spring months (not shown).

We find that the magnitude of the SF seasonal cycle is influenced by the underlying bathymetry (not shown). In regions characterized by shallow bottom depths (e.g., along the major ridge systems, through Drake Passage, and on the lee side of Kerguelen Plateau), the

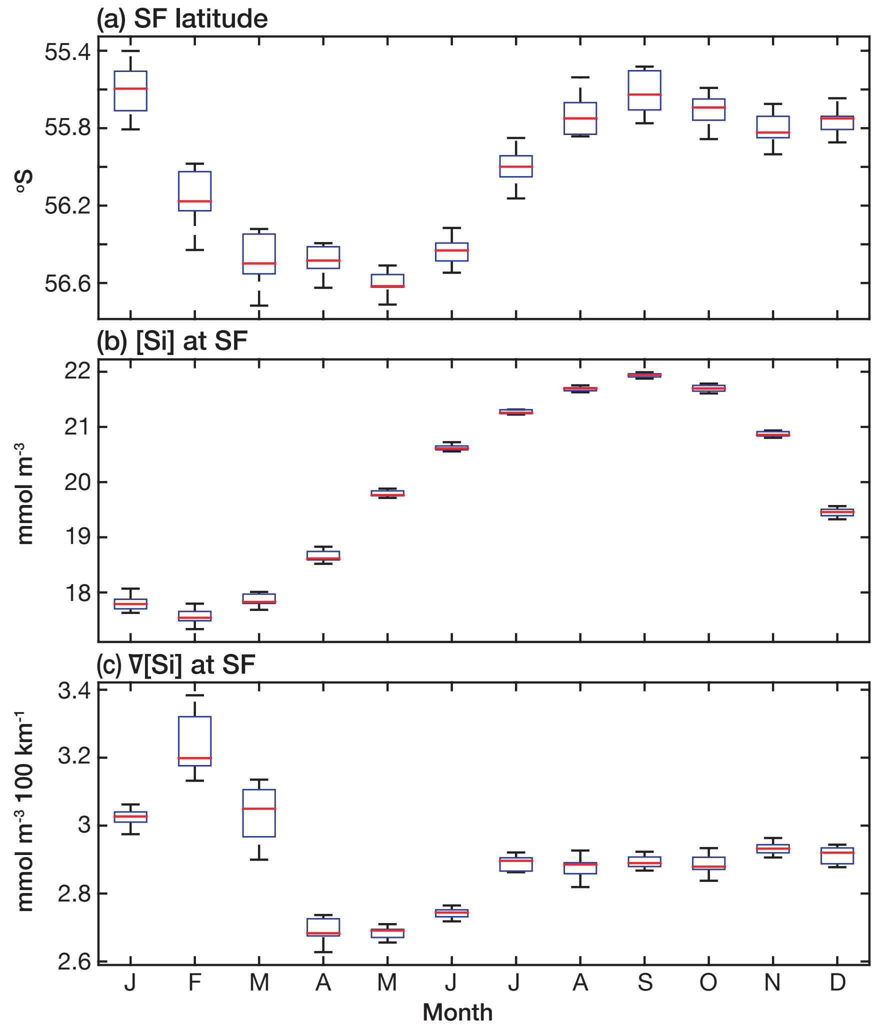

Figure 5.3: The zonal mean (a) SF location, (b) Si concentration at the SF, and (c) intensity of the SF by month from 2000 to 2009. Each box indicates the median value (center red line), 25th and 75th percentiles (blue edges), and extreme data points not considered outliers (black whiskers) of the given data variable.

magnitude of the seasonal cycle described above is suppressed. The magnitude of the SF seasonal cycle is greatest in the ∼300–330°E sector, owing to competing Si pools between the Patagonia Shelf region to the north and the northern Weddell Sea region to the south. During the productive summer months, Si:N exceeds one and increases across and to the south and east of the Patagonia Shelf while in the northern Weddell, where Si is usually enriched relative to N throughout the rest of the year, Si:N generally decreases to less than one. Therefore throughout the year, the SF located in this sector of the Southern Ocean is either representing the northern extent of Si-enriched waters extending from the Weddell Sea or the southern extent of Si-enriched waters extending from the Patagonia Shelf; often in summer, these enriched Si:N pools merge, preventing the detection of a SF.

5.4.3 Interannual to interdecadal variability

We find that interannual variability in the SF is low, where the standard deviation in the monthly SF position is generally ≤1°latitude; one exception being the ∼300–330°E sector, where the standard deviation can be as large as ∼4°latitude (not shown). However, in the long-term, the SF becomes more variable on interannual timescales, particularly in regions where the underlying bathymetry is deep. For example, in the southeast Indian sector (∼100°E), the standard deviation in the monthly SF position is consistently ∼1°latitude during the 20th century but nears ∼3°latitude throughout the 21st. Overall, the seasonal and interannual variability in the SF is relatively low as compared to that in the observed PF (*Freeman et al.*, 2016), suggesting that the underlying bathymetry exhibits greater influence on the PF than the associated SF on these shorter timescales.

The influence of bathymetry on the position of the SF is more evident on longer timescales. Figure 5.4 displays the historical, present, and future decadal mean SF positions overlain on the bathymetry simulated by the CESM-LE. We find that interdecadal variability in the SF is influenced by the underlying bathymetry, similar to the interannual variability reported for the associated PF over the shorter observational record (*Deacon*, 1937; *Gordon*

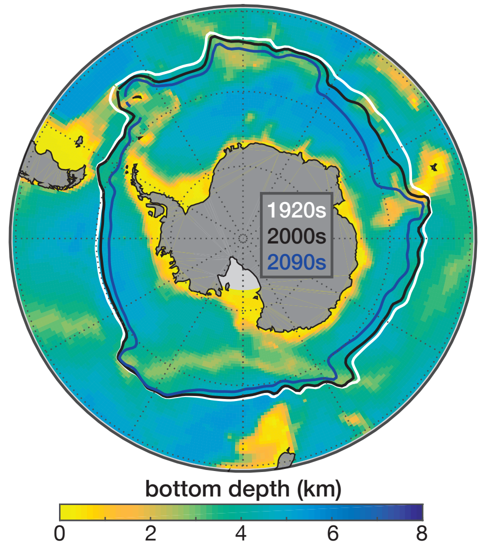

Figure 5.4: Decadal mean SF positions: historical (1920s; white contour), present-day (2000s; black contour), and future (2090s; blue contour) mean location. Bathymetry, as simulated by the CESM1, displayed underneath SF positions in color, where warm colors indicate shallow bathymetry and cool colors, deep.

et al., 1978; *Chelton et al.*, 1990; *Gille*, 1994; *Moore et al.*, 1999; *Dong et al.*, 2006a; *Sallée et al.*, 2008; *Freeman et al.*, 2016). Interdecadal variability is low along the Mid-Atlantic and Pacific-Antarctic ridges and across the Kerguelen Plateau, and larger over the deeper basins, particularly in the ~30–70°E sector.

5.4.4 Long-term change

From 1920 to 2100, we find that the monthly, zonally averaged SF location shifts poleward by ~3°latitude (Figure 5.5a): under historical forcing (1920–2005), the SF is displaced southward by ~1°latitude and under RCP 8.5 forcing (2006–2100), the SF shifts even further south, by an additional ~2°latitude. The intensity of the annual, zonal mean SF and its associated Si concentration increases over this time period, by nearly 0.4 mmol m^{-3} 100 km^{-1} and 0.5 mmol m^{-3}, respectively, a further indication of a more southerly SF in future. Under RCP 8.5 forcing, the annual, zonal mean SF freshens by ~0.2 g kg^{-1} and warms by ~1.5°C, while its associated SSH decreases by ~0.4 m and MLD shoals by more than 5 m.

Figure 5.5b displays the total change in the SF between the 2000s and 2090s (see Section

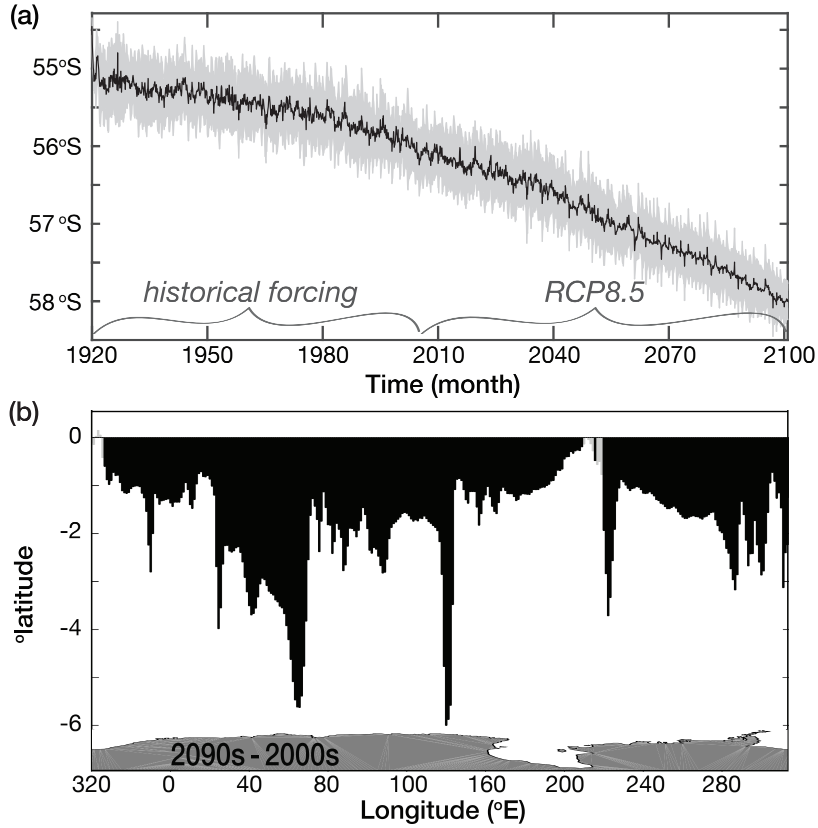

Figure 5.5: (a) Time series (1920–2100) of CESM-LE monthly, zonal, ensemble mean (black contour) SF position ($\pm 1\sigma$ across the 32 ensemble members indicated by gray shading); the seasonal cycle has been removed via seasonal filtering). (b) Total shift in CESM-LE monthly ensemble mean SF position (negative – southward) between the 2000s and 2090s. Black bars indicate significance based on the spread (signal:noise) in the ensemble members.

5.3.1) at all longitudes. We find that the SF shifts poleward, by up to 6 °latitude in some regions. The varied magnitude of the shifts across the basin reflect the influence of bottom depth on long-term change in the SF: smallest (and sometimes not statistically significant) meridional shifts are found in regions characterized by shallow bottom depths while the largest (and most significant) meridional shifts are found in deeper ocean regions (see also Figure 5.4). Across the basin, these poleward displacements are not found to be driven by a particular season but are consistent across summer and winter months, albeit some regions exhibit a greater magnitude in the long-term southward shift in summer (not shown).

Why does the SF shift south? We find that a more poleward SF in future, as simulated by the CESM-LE, reflects large-scale changes in Southern Ocean nutrients in a warmer world: a basin-wide decrease in Si and N availability at the surface (Figure 5.6). The subsurface SF also shifts poleward in future, but in smaller magnitude, also as a result of less Si and N availability at 200 m in future (not shown). Figure 5.6 demonstrates that the magnitude of the long-term decrease in Si is greater than that for N, further supporting a more poleward SF in future; indeed, we find long-term decreases in Si:N ratios across the basin (not shown). Additionally, we find a long-term intensification of the SF. Across the Southern Ocean, the local gradients in Si increase between the present-day and future positions of the SF; a few regional exceptions include the New Zealand and Scotia Sea sectors, on the windward side of Kerguelen, and at ∼20°E, where a southward shift in the SF is marked by a weakening of the background gradients in Si. We discuss possible mechanisms for long-term nutrient decline in the upper 200 m in Section 5.5.

5.5 Discussion

In this study, we present an analysis of the large-scale, persistent SF using the CESM-LE simulations, allowing for the separation of natural variability from long-term forced trends under a high-emission scenario. Here, we examine the long-term poleward shift of the SF

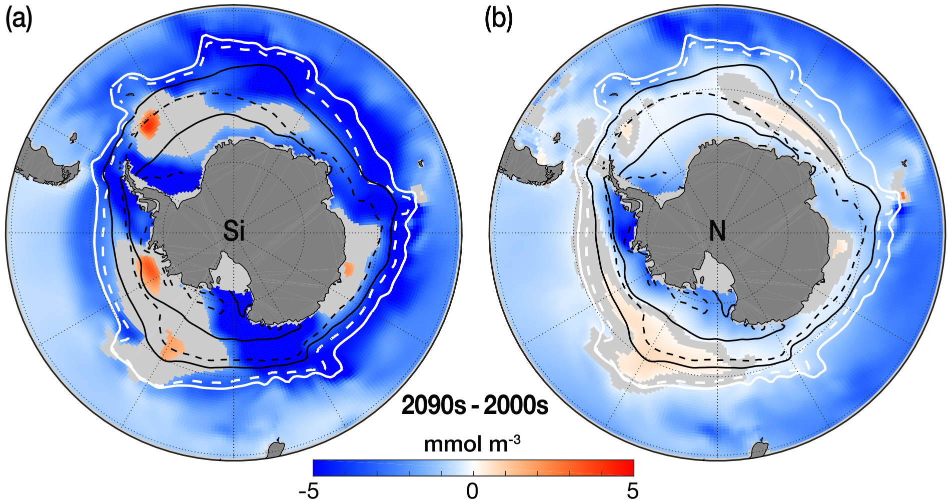

Figure 5.6: Epoch differences (2090s − 2000s) in CESM-LE simulated surface (a) Si and (b) N concentration (colors); only significant changes are shown (see Section 5.3.1). Gray contours indicate the present (solid) and future (dashed) decadal mean positions of the SF. Black contours mark the present (solid) and future (dashed) decadal mean maximum (September; most northerly) and minimum (February; most southerly) sea ice extent (see Section 5.3.1).

in the context of physical circulation and phytoplankton dynamics. Next, we highlight broader implications and consequences of variability and long-term change in the SF in light of observational work and CESM-LE-projected future anthropogenic warming. We further contextualize these CESM-LE results by comparing to model results from three of the CMIP5 model suite. Lastly, we discuss the limitations of this study.

5.5.1 A more poleward SF: Mechanisms and implications

We assessed long-term change in the position of the surface SF. According to the CESM-LE simulations, the SF shifts south both in zonal average (1920–2100; Figure 5.5a) and at nearly every longitude (2090s–2000s; Figure 5.5b). A more poleward SF can be explained by a combination of physical and biological processes that drive nutrient reductions at the surface (2090s–2000s; Figure 5.6).

Physical mechanisms

We find that the Southern Ocean warms by up to 6°C (Figure 5.7a), acting to increase stratification by up to 40% (Figure 5.7b) and shoal MLDs by 20 m in some regions (MLDs; Figure 5.7c). While zonal wind stress increases significantly across the east Indian and Pacific basins (not shown), which would act to deepen MLDs, the robust MLD shoaling across the basin (Figure 5.7c) suggests that the ML response is dominated by increased stratification; ML deepening found nearer the Antarctic continent is likely a result of a reduction in maximum (September) sea ice extent under RCP 8.5 forcing (see Figure 5.7c).

Biological mechanisms and implications

Phytoplankton physiology will be directly and indirectly affected by Southern Ocean warming: warming increases phytoplankton growth rates while warming-induced stratification limits access to nutrients through a reduction in the vertical supply. While spatially heterogeneous, we observe significant increases in diatom carbon (i.e., biomass) in large regions of the Southern Ocean over the 21st century (Figure 5.7d), consistent with studies that have reported increased diatom net primary productivity here (*Marinov et al.*, 2010; *Leung et al.*, 2015; *Krumhardt et al.*, 2017). We attribute increases in diatom biomass to reduced iron (Fe) limitation: greater Fe availability across the basin in the 2090s relative to the 2000s is likely the result of an excess of Fe that has been laterally advected, unused, from lower latitudes that have experienced reduced productivity (*Marinov et al.*, 2010; *Moore et al.*, 2013).

Small phytoplankton are more competitive for nutrients at low concentrations; this larger surface area-to-volume ratio is parameterized in CESM via prescribed half-saturation coefficients for nutrient uptake. It is therefore expected that small phytoplankton will tend to dominate over the larger diatoms in a warmer world (*Marinov et al.*, 2010). Indeed, small phytoplankton dominate the total carbon pool across the ACC latitudes over the entire simulation period (1920–2100), despite long-term increases in diatom biomass (Figure 5.7d);

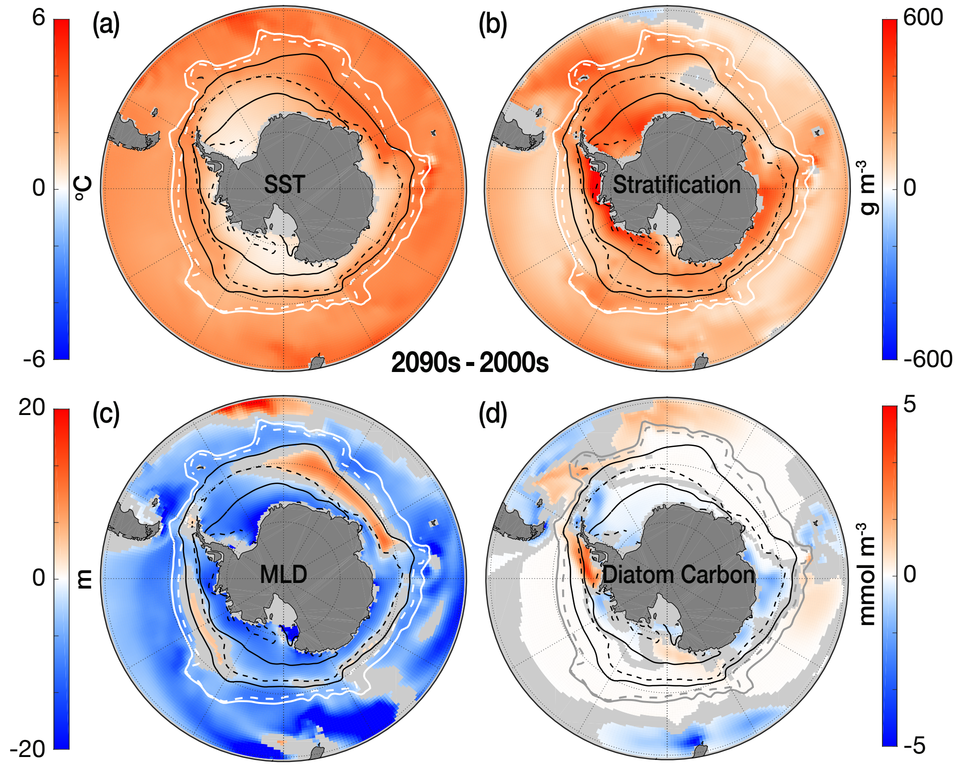

Figure 5.7: Epoch differences (2090s − 2000s) in CESM-LE simulated surface (a) SST, (b) stratification, (c) MLD, and (d) diatom carbon; only significant changes are shown (see Section 5.3.1). Contours in stereographic plots are the same as in Figure 5.6, except in (d) where the SF contours are gray instead of white in order to improve readability.

where we find increases in diatom biomass (Figure 5.7d), we find decreases in small phytoplankton biomass (not shown). Therefore, it is likely that some portion of the long-term decrease in surface nutrients (Figure 5.6) is a biological depletion signal, attributable to increased diatom productivity here, adding to the physical reduction signal described above and driving the long-term trend more negative. Given that increased nutrient depletion lowers preformed nutrient concentrations, we speculate that the efficiency of the biological pump in this region increases under RCP 8.5 forcing (see *Marinov et al.*, 2006).

The SF on Glacial-Interglacial timescales

A long-term poleward displacement in the SF has implications for water-mass formation in the Southern Ocean and thus global nutrient and carbon cycling. Hereafter, we refer to waters north (south) of the PF/SF as Subantarctic (Antarctic) waters. Si-enriched Antarctic waters moving northward across the PF are stripped by diatoms in the upwelling zone, setting the nutrient concentration of the subsequent entrainment to Subantarctic Mode Water (SAMW). SAMW plays a significant role in the global thermocline nutrient cycle (*McCartney*, 1982; *Sloyan and Rintoul*, 2001) and thus low-latitude productivity (*Sarmiento et al.*, 2004; *Marinov et al.*, 2006) as it spreads equatorward at depth. *Sarmiento et al.* (2004) define a tracer, Si*, to track SAMW: Si* = 0 equates to our Si:N = 1 definition and coincides with this frontal zone of upwelling UCDW and subsequent SAMW formation. We speculate that a significant meridional displacement in the SF (the latitude where Si:N = 1 or Si* = 0) suggests a displaced SAMW formation region (to the south), altered SAMW nutrient properties (reduced nutrients), and thus changes to global thermocline nutrient cycling and low-latitude productivity (reduced productivity). Indeed, *Leung et al.* (2015) and *Krumhardt et al.* (2017) find reduced low-latitude productivity, as simulated by the CMIP5 model suite and the CESM-LE, respectively.

While these Subantarctic waters are important in determining low-latitude productivity, *Marinov et al.* (2006) further highlight the key role of Antarctic waters in determining the air-sea carbon balance. A more poleward SF has implications for the interpretation of paleoclimate records, e.g., explaining lower atmospheric carbon dioxide concentrations during the Last Glacial Maximum (*Martin*, 1990; *Sigman and Boyle*, 2000; *Stephens and Keeling*, 2000; *Toggweiler et al.*, 2006; *Toggweiler*, 2009). It begs the question whether a significantly displaced SF (i.e., a reduction in the total extent of Antarctic surface waters) will impact future air-sea carbon flux. The relationship between diatom productivity and export in the silicate-replete Antarctic waters and the opal-dominated sediments below has been used to reconstruct paleo positions of the PF and to infer changes in Si availability and diatom productivity on glacial-interglacial timescales (*Abelmann et al.*, 2006; *Anderson et al.*, 2009; *Kemp et al.*, 2010). Whether the PF was displaced significantly north or south from its modern-day position on these timescales is still an open question (see *Kemp et al.*, 2010). Our simulated results suggest that on a near-centennial timescale, the SF can vary by up to 6°latitude in regions not characterized by shallow bathymetry.

5.5.2 Observational and intermodel comparison

The simulated diatom response to reduced Fe limitation highlights how important Fe is for phytoplankton productivity in this vast HNLC region of the World Ocean. Among the simulated limiting factors, either by macronutrients (Si, N, phosphate), Fe, or light, Fe limitation tends to dominate our latitudes of interest (i.e., the ACC latitudes of the Southern Ocean). As simulated by the CESM-LE, Si is never a limiting factor for diatoms in these latitudes, even in the lower latitudes of the Indian and Pacific sectors where surface Si concentrations can be <5 mmol m^{-3}. While it is well established that Fe and light limitation may put serious constraints on phytoplankton growth in the Southern Ocean, diatoms do experience Si limitation as well as co-limitation with Fe and/or light (*Cortese and Gersonde*, 2008; *Hoffmann et al.*, 2008). Indeed, some microcosm and open Southern Ocean studies suggest that Si is a major driver in the partitioning of diatoms vs. smaller phytoplankton (e.g., coccolithophores; *Egge and Aksnes*, 1992; *Eynaud et al.*, 1999; *Mohan et al.*, 2008). Therefore, a long-term southward shift in the Southern Ocean SF has implications for the biogeography of the Southern Ocean. Perhaps if Fe limitation as simulated by the CESM did not dominate to the point of preventing realistic Si limitation in some regions of the Southern Ocean, the diatom response to a more southward SF and thus reduced Si and N availability at the surface would look differently in Figure 5.7d.

The CESM-LE simulations tend to have surface Si concentrations (Figure 5.8a) that compare well spatially, but are of lesser magnitude, relative to observed climatologies (e.g., WOA13 in Figure 5.1a), with some indication that the model underestimates the amplitude of interannual variability (not shown). *Moore et al.* (2013) document the known low nutrient bias in the Southern Ocean, partially explained by weak vertical exchange and MLD biases, processes that influence CESM-simulated biogeochemistry. However, when present-day mean

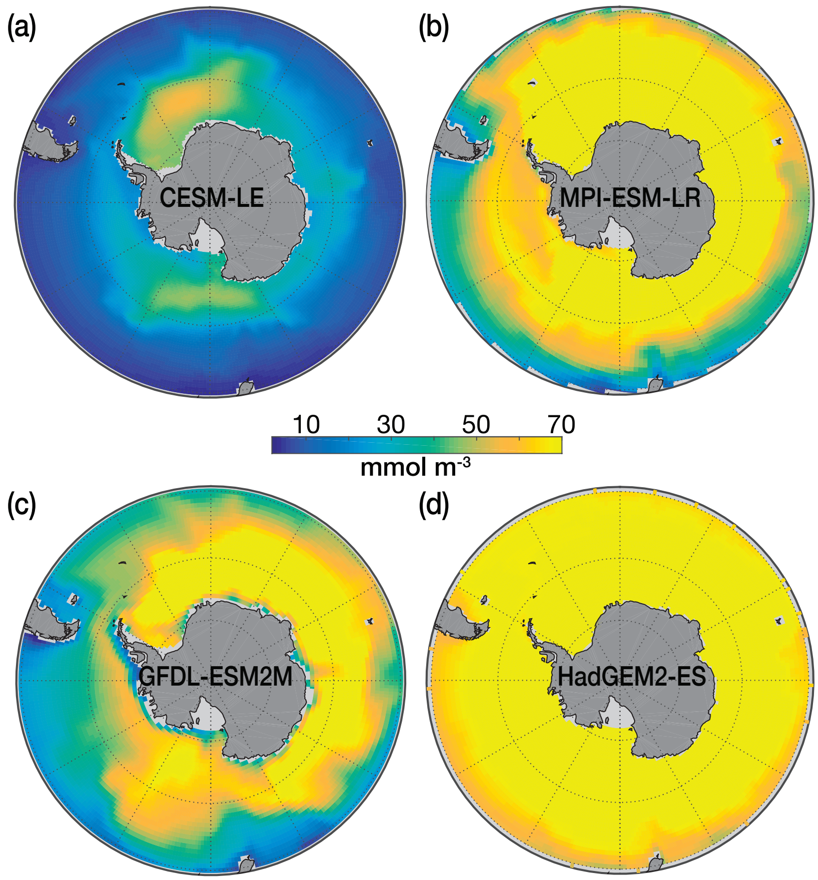

Figure 5.8: Present-day (2000s) mean surface Si concentration from the (a) CESM-LE ensemble mean, (b) MPI-ESM-LR, (c) GFDL-ESM2M, and (d) HadGEM2-ES. Compare to climatological mean surface Si distribution from WOA13 (Figure 5.1a).

CESM-LE Si is compared to the individual CMIP5 models analyzed here, it is clear that these CMIP5 ESMs exhibit a high Si bias in the Southern Ocean (Figure 5.8b–d), resulting in a misrepresentation of the observed SF. While the MPI-ESM-LR, GFDL-ESM2M, and HadGEM2-ES simulate comparable mean surface N concentrations relative to WOA13, when combined with high Si bias, a greater mean surface Si:N relative to the CESM-LE and WOA13 is the result (not shown); it should be noted that HadGEM2-ES's particular high Si bias marks it as the only ESM where nutrient depletion ratios decrease poleward. These discrepancies make difficult the direct comparison of the simulated SF across the CMIP5 models (not shown) but cement the CESM-LE as the optimal tool in investigating the Southern Ocean SF.

5.5.3 Study limitations

Unlike the observed complex frontal structure of the PF, which can split into multiple filaments in regions characterized by deeper bottom depths (*Sokolov and Rintoul*, 2002; *Graham et al.*, 2012), the SF identified in this study is generally located at one latitudinal point at a given longitudinal location (by nature, rather than by choice or mapping scheme). Whether the coarse resolution of the model or our prescribed SF definition hides a more complex frontal feature has not been investigated. Under stressed or limited conditions, particularly under extreme Fe or light limitation, diatoms preferentially strip Si over N, acting to increase the Si:N depletion ratio, with varying magnitude across species (*Franck et al.*, 2000; *Brzezinski and Jones*, 2003). The effects of Fe limitation on diatom Si:N depletion ratios could explain why the magnitude of the long-term decrease in surface Si is greater than that for N (Figure 5.6). One could argue that our CESM-LE SF definition may not be suitable given observed and simulated Fe and light limitation here. While our definition does coincide with enhanced gradients in Si, future studies interested in the response of phytoplankton groups to changes in the SF should test a variety of ratio values. Furthermore, observations show that under severe Fe limitation, some species of Southern Ocean diatoms tend to be characterized as "highly-silicified" (*Smetacek et al.*, 2004; *Hoffmann et al.*, 2007), with unique implications for ocean carbon and Si cycles (see *Assmy et al.*, 2013). As CESM does not simulate the degree to which a diatom is silicified, the diatom response reported here does not capture this observed adaptation.

5.6 Conclusions

We quantify the temporal variability in the Southern Ocean SF using CESM-LE simulated Si and N concentrations in the surface layer. In summary, we find that the latitudinal location of the SF varies seasonally, in its northernmost position in austral winter and southernmost position in summer, reflecting seasonal diatom utilization of Si and N. The SF is influenced by the underlying bathymetry on interdecadal timescales, acting to limit its meridional extent and temporal variance over shallow regions, while over deep basins, interannual to interdecadal variability in the SF increases under RCP 8.5 forcing. In the long term, the SF shifts poleward both in zonal average and at nearly every longitude under historical and RCP 8.5 forcing. We find that an equivalent SF defined in three individual models of the CMIP5 suite cannot be directly compared, due to large discrepancies and inadequacies in simulating observed nutrient distributions in the Southern Ocean; we therefore conclude that currently, the CESM-LE is most representative and suited for identifying and tracking the SF in space and time. We attribute a more poleward SF in the CESM-LE to a reduction in the vertical supply of silicate and nitrate driven by warming, increased stratification, and shallower mixed layer depths across the basin. Despite a more poleward SF and reductions in silicate, Southern Ocean diatoms tend to fare better in this future scenario, most likely due to reduced iron limitation over time. These results suggest large-scale shifts in biogeochemical cycling in a warmer world.

Acknowledgments

Climatological nutrient data from the World Ocean Atlas Database (2013) is available at http://nodc.noaa.gov/OC5/woa13/. Weekly Polar Front realizations spanning 2002 and 2014 are available at doi.pangaea.de/10.1594/PANGAEA.855640. CESM computing resources were provided by CISL at NCAR. CESM ensemble output is available from the Earth System Grid at earthsystemgrid.org/dataset/ucar.cgd.ccsm4.CESM_CAM5_BGC_LE.html. This study was supported by NSF (OCE-1558225; PLR-1543457; OCE-1258995; OCE-1155240) and NOAA (NA12OAR4310058). NCAR is sponsored by NSF.

Chapter 6

Summary and Conclusions

Using hydrographic and satellite observations and a coupled climate model, this dissertation investigates the mean and time-varying large-scale, persistent physical and biogeochemical features that characterize the Southern Ocean on seasonal, interannual, and interdecadal timescales. Through changes in atmospheric forcing and associated physical and biogeochemical processes, large-scale changes in the Great Calcite Belt, Antarctic Polar Front (PF), and Southern Ocean Silicate Front (SF) have been identified over the recent past and coming century.

Large decreases in satellite-estimated biocalcification in austral summer are found to occur in large portions of the Southern Ocean within the Great Calcite Belt. Hydrographic observations of changing seawater carbonate chemistry support these findings, by indicating that the effects of ocean acidification are already impacting calcifying phytoplankton here. A regional increase in calcification is found to correspond to a long-term southward displacement of the PF, suggesting that a frontal shift may have altered local physical and chemical properties, particularly those that influence interspecies competition for nutrients. These results highlight and motivate the potential influence of frontal variability on local biogeography.

A higher resolution investigation of the mean state and variability of the PF is afforded through the utilization of sea surface temperatures (SSTs) estimated from cloud-penetrating microwave radiometers and a more comprehensive, local frontal identification scheme. A large portion of the variability in the PF is found to be tied to the underlying bathymetry of the Southern Ocean. While the Polar Front exhibits greater interannual variability and can shift meridionally by hundreds of kilometers in regions not characterized by shallow bathymetry, this thermal front has intensified across the basin. Over this time period, frontal intensification is thought to be linked to a more zonally asymmetric Southern Hemisphere atmospheric circulation; observational estimates of surface wind speed, westerly jet position, and SST indicate that a dominant high pressure system over the Atlantic sector and low pressure system over the Pacific are linked to regional but zonally symmetric changes in the strength of the PF.

Hydrographic observations suggest that the Polar Front is largely coincident with an important biogeochemical front, the Southern Ocean Silicate Front (SF), but due to a lack of time-varying nutrient observations, the mean state and variability of the SF has been largely unknown. Model output is used to demonstrate that the SF coincides with and varies much like the observed PF in many regions of the Southern Ocean, particularly in regions characterized by shallow bathymetry. Model results suggest that a more stratified upper ocean via large-scale changes in temperature under RCP 8.5 forcing partially explain the long-term southward displacement in the mean position of the SF by the end of the 21st century.

In conjunction with this work on the PF, a consensus is forming within the community on the importance of methodology in locating particular ACC fronts and studying the temporal variability of front locations. Concurrent with this dissertation, several recent studies, both published and not yet published, suggest a re-evaluation of our current ACC frontal identification methods and caution against the interpretation of studies using fixed sea surface height contours to detect long-term frontal displacements (N. Swart, pers. comm.; *Graham et al.*, 2012; *Gille*, 2014; *Chapman*, 2014). These independent studies, along with this dissertation, confirm that despite significant changes in atmospheric forcing in recent decades, the fronts and jets of the ACC have remained relatively unchanged in position.

Future research on this topic will need to address some of the shortcomings of this work, particularly the degree of time and space resolution. While the satellite ocean color community has nearly two decades of retrievals, from the initial Sea-viewing Wide Field-of-view Sensor (SeaWiFS) and transition to the Moderate Resolution Imaging Spectroradiometer (MODIS) platforms, estimates of the long-term biological trends in the Southern Ocean still suffer from sensor differences, extensive cloud cover and thus seasonal bias, ground validation, and short and sparse time series. Some studies and programs have worked to alleviate or elucidate these biases by developing Southern Ocean-specific algorithms (*Johnson et al.*, 2013), increasing *in situ* validation efforts (*Balch et al.*, 2016), improving the transition between sensor platforms as reflected in the retrieval time series (e.g., GlobColour; www.globcolour.info), and elucidating the detection timescales of climate change in satellite ocean color records (*Henson et al.*, 2010). The microwave-estimated PF and modeled SF studies also suffer from low spatial resolution. The PF as identified from microwave radiometers at 0.25° resolution is likely a smoothed look at this variable physical feature, yielding no information on its important, submesoscale features. Additionally, the coarse resolution of the model employed here could be leading to inconsistencies with realistic physical and biological mechanisms associated with SF variability (e.g., eddy parameterization, phytoplankton dynamics, iron limitation, etc.), likely causing spurious results. It is therefore vital to continue to work toward bridging the gap between modeled and observed physics and biogeochemistry in order to adequately assess the role of climate variability and change in controlling these inherently interdependent processes of the Southern Ocean.

Keeping the above known caveats in mind, the insights gained herein represent significant progress in the study of physical and biogeochemical oceanography in the Southern Ocean. These insights can be applied toward understanding these important large-scale features and help lay the groundwork for future investigations here. Many coupled climate models project a continued poleward strengthening of the westerlies in the future, with much of this trend influenced by greenhouse gas concentrations and stratospheric ozone changes, as well as drastic reductions in the amount of Antarctic sea ice. Given the complexity of the biological response to ocean acidification across communities and even amongst species, the response of Southern Ocean calcifiers is still largely unknown. As the PF and SF have direct influence on both the physical and biological processes of the Southern Ocean, a continued striving toward a better understanding of these key features is critical.

In the context of past climatic variability, sediment cores suggest that the PF and/or SF was displaced significantly from its modern-day position. This dissertation highlights the clear need to quantify/characterize the modern-day coupling or decoupling of these two frontal features, and their impact on local biological productivity and biogeography, before interpreting these sediment records and inferring details about the paleo position of the westerlies. Indeed, an important feedback may exist between the position of the westerlies and atmospheric carbon dioxide concentrations on glacial-interglacial timescales (e.g., *Toggweiler et al.*, 2006).

Sparse observations and high variability of the system drive large unknowns in the Southern Ocean. Historically, upper ocean observations are sparse, but, to the delight and advantage of the Southern Ocean community, highly complimentary: ship-based hydrography (early 1900s–present; seasonally biased), autonomous floats (2002–present; spatial bias due to sea ice), and a seal CTD database (2004–present; less seasonal bias than hydrography), are a few examples. Additionally, given the importance of increasing our understanding of the deep Southern Ocean, the international community has implemented programs such as *Deep Argo*. As such, it is currently an exciting time for Southern Ocean research, as technology and creativity are improving existing and creating new observing and modeling capabilities. Future Southern Ocean work depends on continued improvement and representation in Earth System Models and sustained long-term observing platforms, including satellites and repeat hydrographic cruises; such a symbiosis between models and observations will only improve our understanding of both the mean, variability, and long-term change in the Southern Ocean and our ability to predict future change.

Bibliography

Abelmann, A., R. Gersonde, G. Cortese, G. Kuhn, and V. Smetacek (2006), Extensive phytoplankton blooms in the Atlantic sector of the glacial Southern Ocean, *Paleoceanography*, *21*(PA1013), doi:10.1029/2005PA001199.

Aksnes, D. L., J. K. Egge, R. Rosland, and B. R. Heimdal (1994), Representation of *Emiliania huxleyi* in phytoplankton simulation models. A first approach, *Sarsia*, *79*(4), 291–300.

Anderson, R. F., S. Ali, L. I. Bradtmiller, S. H. H. Nielsen, M. Q. Fleisher, B. E. Anderson, and L. H. Burckle (2009), Wind-driven upwelling in the Southern Ocean and the deglacial rise in atmospheric CO_2, *Science*, *323*(5920), 1443–1448, doi:10.1126/science.1167441.

Ansorge, I. J., J. M. Jackson, K. Reid, J. V. Durgadoo, S. Swart, and S. Eberenz (2014), Evidence of a southward eddy corridor in the south-west Indian ocean, *Deep-Sea Res II*, doi:10.1016/j.dsr2.2014.05.012.

Aoki, S., M. Yoritaka, and A. Masuyama (2003), Multidecadal warming of subsurface temperature in the Indian sector of the Southern Ocean, *Journal of Geophysical Research*, *108*(C4), 8081, doi:10.1029/2000JC000307.

Arrigo, K. R., D. H. Robinson, D. L. Worthen, R. B. Dunbar, G. R. DiTullio, M. VanWoert, and M. P. Lizotte (1999), Phytoplankton community structure and the drawdown of nutrients and CO_2 in the Southern Ocean, *Science*, *283*(5400), 365–367.

Assmy, P., V. Smetacek, M. Montresor, C. Klaas, J. Henjes, V. H. Strass, J. M. Arrieta, U. Bathmann, G. M. Berg, E. Breitbarth, B. Cisewski, L. Friedrichs, N. Fuchs, G. J. Herndl, S. Jansen, S. Krägefsky, M. Latasa, I. Peeken, R. Röttgers, R. Scharek, S. Schüller, A. Webb, and D. Wolf-Gladrow (2013), Thick-shelled, grazer-protected diatoms decouple ocean carbon and silicon cycles in the iron-limited Antarctic Circumpolar Current, *PNAS*, *110*(51), 20,633–20,638, doi:10.1073/pnas.1309345110.

Balch, W. M., H. R. Gordon, B. C. Bowler, D. T. Drapeau, and E. S. Booth (2005), Calcium carbonate budgets in the surface global ocean based on modis data, *J. Geophys. Res. Oceans*, *110*(C07001).

Balch, W. M., D. T. Drapeau, B. C. Bowler, and E. S. Booth (2007), Prediction of pelagic calcification rates using satellite measurements., *Deep-Sea Res II*, *54*, 478—495.

Balch, W. M., D. T. Drapeau, B. C. Bowler, E. Lyczskowski, E. S. Booth, and D. Alley (2011), The contribution of coccolithophores to the optical and inorganic carbon budgets during the Southern Ocean Gas Exchange Experiment: New evidence in support of the "Great Calcite Belt" hypothesis, *J. Geophys. Res.*, *116*(C00F06).

Balch, W. M., D. T. Drapeau, B. C. Bowler, E. R. Lyczskowski, L. C. Lubelczyk, S. C. Painter, and A. J. Poulton (2014), Surface biological, chemical, and optical properties of the patagonian shelf coccolithophore bloom, the brightest waters of the great calcite belt, *Limnol. Oceanogr.*, *59*(5), 1715–1732.

Balch, W. M., N. R. Bates, P. J. Lam, B. S. Twining, S. Z. Rosengard, B. C. Bowler, D. T. Drapeau, R. Garley, L. C. Lubelczyk, C. Mitchell, and S. Rauschenberg (2016), Factors regulating the Great Calcite Belt in the Southern Ocean and its biogeochemical significance, *Global Biogeochemical Cycles*, *30*, 1124–1144, doi:10.1002/2016GB005414.

Banks, H. T., R. A. Wood, J. M. Gregory, T. C. Johns, and G. S. Jones (2000), Are observed decadal changes in intermediate water masses a signature of anthropogenic climate change?, *Geophysical Research Letters*, *27*, 2961–2964.

Beaufort, L., M. Couapel, N. Buchet, H. Claustre, and C. Goyet (2008), Calcite production by coccolithophores in the south east pacific ocean, *Biogeosciences*, *5*(4), 1101–1117, doi:10.5194/bg-5-1101-2008.

Beaufort, L., I. Probert, T. de Garidel-Thoron, E. M. Bendif, D. Ruiz-Pino, N. Metzl, C. Goyet, N. Buchet, P. Coupel, M. Grelaud, B. Rost, R. E. M. Rickaby, and C. de Vargas (2011), Sensitivity of coccolithophores to carbonate chemistry and ocean acidification, *Nature*, *476*(7358), 80–83.

Belkin, I. M., and A. L. Gordon (1996), Southern Ocean fronts from the Greenwich meridian to Tasmania, *Journal of Geophysical Research*, *101*, 3675–3696.

Bhanoo, S. N. (2015), Marine Life: Phytoplankton on Decline in Southern Ocean, *New York Times*, p. D4.

Billany, W., S. Swart, J. Hermes, and C. J. C. Reason (2010), Variability of the Southern Ocean fronts at the Greenwich Meridian, *Journal of Marine Systems*, *82*, 304–310, doi:10.1016/j.jmarsys.2010.06.005.

Böning, C. W., A. Dispert, M. Visbeck, S. R. Rintoul, and F. U. Schwarzkopf (2008), The response of the Antarctic Circumpolar Current to recent climate change, *Nature Geoscience*, *1*, 864–869.

Boyd, P. W., J. LaRoche, M. Gall, R. Frew, and R. M. L. McKay (1999), Role of iron, light, and silicate in controlling algal biomass in subantarctic waters SE of New Zealand, *Journal of Geophysical Research*, *104*(C6), 395–408.

Boyd, P. W., T. Jickells, C. S. Law, S. Blain, E. A. Boyle, K. O. Buesseler, K. H. Coale, J. J. Cullen, H. J. W. de Baar, M. Follows, M. Harvey, C. Lancelot, M. Levasseur, N. P. J.

Owens, R. Pollard, R. B. Rivkin, J. Sarmiento, V. Schoemann, V. Smetacek, S. Takeda, A. Tsuda, S. Turner, and A. J. Watson (2007), Mesoscale iron enrichment experiments 1993–2005: Synthesis and future directions, *Science*, *315*, 612–617, doi:10.1126/science.1131669.

Boyer, T. P., J. I. Antonov, O. K. Baranova, C. Coleman, H. E. Garcia, A. Grodsky, D. R. Johnson, R. A. Locarnini, A. V. Mishonov, T. D. O'Brien, C. R. Paver, J. R. Reagan, D. Seidov, I. V. Smolyar, and M. M. Zweng (2013), *World Ocean Database 2013*, no. 72 in NOAA Atlas NESDIS, 209 pp.

Bretherton, C. S., M. Widmann, V. P. Dymnikov, J. M. Wallace, and I. Bladé (1999), The Effective Number of Spatial Degrees of Freedom of a Time-Varying Field, *Journal of Climate*, *12*, 1990–2009, doi:10.1175/1520-0442(1999)012⟨1990:TENOSD⟩2.0.CO;2.

Broecker, W. S., and T.-H. Peng (1982), Tracers in the sea, *A publication of the Lamont-Doherty Geological Observatory.*

Broecker, W. S., S. Sutherland, and T.-H. Peng (1999), A possible 20th-century slowdown of Southern Ocean deep water formation, *Science*, *286*(5442), 1132–1135.

Brown, Z. W., and K. R. Arrigo (2012), Contrasting trends in sea ice and primary production in the Bering Sea and Arctic Ocean, *ICES Journal of Marine Science: Journal du Conseil*, *69*(7), 1180–1193.

Brzezinski, M. A., and J. L. Jones (2003), The balance between silica production and silica dissolution in the sea: Insights from Monterey Bay, California, applied to the global data set, *Limnology and Oceanography*, *48*(5), 1846–1854.

Cai, W., T. Cowan, S. Godfrey, and S. Wijffels (2010), Simulations of Processes Associated with the Fast Warming Rate of the Southern Midlatitude Ocean, *Journal of Climate*, *23*, 197–206, doi:10.1175/2009JCLI3081.1.

Cavalieri, D., C. Parkinson, P. Gloersen, and H. Zwally (1996, updated yearly), *Sea Ice Concentrations from Nimbus-7 SSMR and DMSP SSM/I-SSMIS Passive Microwave Data.*

Chapman, C. C. (2014), Southern Ocean jets and how to find them: Improving and comparing common jet detection methods, *Journal of Geophysical Research: Oceans*, *119*, 4318–4339, doi:10.1002/2014JC009810.

Chase, Z., K. E. Kohfeld, and K. Matsumoto (2015), Controls on biogenic silica burial in the Southern Ocean, *Global Biogeochemical Cycles*, *29*, 1599–1616, doi:10.1002/2015GB005186.

Chelton, D. B., M. G. Schlax, D. L. Witter, and J. G. Richman (1990), Geosat altimeter observations of the surface circulation of the Southern Ocean, *Journal of Geophysical Research*, *95*(C10), 17,877–17,903, doi:10.1029/JC095iC10p17877.

Collins, W. J., et al. (2011), Development and evaluation of an Earth-system model - HadGEM2, *Geosci. Model Dev.*, *4*(4), 1051–1075, doi:10.5194/gmd-4-1051-2011.

Cortese, G., and R. Gersonde (2008), Plio/Pleistocene changes in the main biogenic silica carrier in the Southern Ocean, Atlantic Sector, *Marine Geology*, *252*, 100–110, doi:10.1016/j.margeo.2008.03.015.

Cubillos, J., S. Wright, G. Nash, M. De Salas, B. Griffiths, B. Tilbrook, A. Poisson, and G. Hallegraeff (2007), Calcification morphotypes of the coccolithophorid *Emilianiahuxleyi* in the Southern Ocean: changes in 2001 to 2006 compared to historical data, *Marine Ecology-Progress Series*, *348*(October), 47–54.

Cunningham, S. A., S. G. Alderson, and B. A. King (2003), Transport and variability of the antarctic circumpolar current in drake passage, *Journal of Geophysical Research*, *108*(C5), 8084.

Danabasoglu, G., S. C. Bates, B. P. Briegleb, S. R. Jayne, M. Jochum, W. G. Large, S. Peacock, and S. G. Yeager (2012), The CCSM4 ocean component, *Journal of Climate*, *25*(5), 1361–1389, doi:10.1175/JCLI-D-11-00091.1.

De Deckker, P., M. Moros, K. Perner, and E. Jansen (2012), Influence of the tropics and southern westerlies on glacial interhemispheric asymmetry, *Nature Geoscience*, *5*, 266–269, doi:10.1038/NGEO1431.

de Szoeke, R. A., and M. D. Levine (1981), The advective flux of heat by mean geostrophic motions in the Southern Ocean, *Deep-Sea Res. Part A: Oceanographic Research Papers*, *28*(10), 1057–1085, doi:10.1016/0198-0149(81)90048-0.

Deacon, G. E. R. (1933), A general account of the hydrology of the South Atlantic Ocean, *Discovery Rep.*, *VII*, 177–238.

Deacon, G. E. R. (1937), The hydrology of the Southern Ocean, *Discovery Rep.*, *XV*, 1–124.

Deacon, G. E. R. (1982), Physical and biological zonation in the Southern Ocean, *Deep-Sea Research*, *29*(1), 1–15, doi:10.1016/0198-0149(82)90058-9.

Delille, B., J. Harlay, I. Zondervan, S. Jacquet, L. Chou, R. Wollast, R. G. J. Bellerby, M. Frankignoulle, A. V. Borges, U. Riebesell, and J. P. Gattuso (2005), Response of primary production and calcification to changes of $p\mathrm{CO_2}$ during experimental blooms of the coccolithophorid *Emiliania huxleyi*, *Global Biogeochemical Cycles*, *19*, 1–14, doi:10.1029/2004GB002318.

DeMaster, D. J. (1981), The supply and accumulation of silica in the marine environment, *Geochimica et Cosmochimica Acta*, *45*, 1715–1732.

DeMaster, D. J. (2002), The accumulation and cycling of biogenic silica in the Southern Ocean: revisiting the marine silica budget, *Deep-Sea Research II*, *49*, 3155–3167.

Dickson, A. (1990), Standard potential of the reaction: AgCl(s) + 1/2 H_2(g) = Ag(s) + HCl(aq), and the standard acidity constant of the ion HSO_4^- in synthetic seawater from 273.15 to 318.15 K, *Journal of Chemical Thermodynamics*, *22*, 113–127.

Doney, S. C., K. Lindsay, I. Fung, and J. John (2006), Natural variability in a stable, 1000-yr global coupled climate-carbon cycle simulation, *Journal of Climate*, *19*(13), 3033–3054, doi:10.1175/JCLI3783.1.

Doney, S. C., V. J. Fabry, R. A. Feely, and J. A. Kleypas (2009), Ocean acidification: the other CO_2 problem, *Annual Review of Marine Science*, *1*, 169–192.

Dong, S., J. Sprintall, and S. T. Gille (2006a), Location of the Antarctic Polar Front from AMSR-E Satellite Sea Surface Temperature Measurements, *Journal of Physical Oceanography*, *36*, 2075–2089.

Dong, S., S. T. Gille, J. Sprintall, and C. Gentemann (2006b), Validation of the Advanced Microwave Scanning Radiometer for the Earth Observing System (AMSR-E) sea surface temperature in the Southern Ocean, *J. Geophys. Res.*, *111*(C04002), doi:10.1029/2005JC002934.

Dugdale, R. C., and J. J. MacIsacc (1971), A computation model for th euptake of nitrate in the Peru upwelling region, *Inv. Pesq.*, *35*(1), 299–308.

Dunne, J. P., et al. (2012), GFDL's ESM2 global coupled climate-carbon earth system models. Part I: Physical formulation and baseline simulation characteristics, *Journal of Climate*, *25*, 6646–6665, doi:10.1175/JCLI-D-12-00150.1.

Dunne, J. P., et al. (2013), GFDL's ESM2 global coupled climate-carbon earth system models. Part II: Carbon system formulation and baseline simulation characteristics, *Journal of Climate*, *26*, 2247–2267, doi:10.1175/JCLI-D-12-00150.1.

Egge, J. K., and D. L. Aksnes (1992), Silicate as regulating nutrient in phytoplankton competition, *Marine Ecology Progress Series*, *83*(2–3), 281–289.

Engel, A., I. Zondervan, K. Aerts, L. Beaufort, A. Benthien, L. Chou, B. Delille, J.-P. Gattuso, J. Harlay, C. Heemann, et al. (2005), Testing the direct effect of CO_2 concentration on a bloom of the coccolithophorid *emilianiahuxleyi* in mesocosm experiments, *Limnology and Oceanography*, *50*(2), 493–507.

Eynaud, F., J. Giraudeau, J.-J. Pichon, and C. J. Pudsey (1999), Sea-surface distribution of coccolithophores, diatoms, silicoflagellates and dinoflagellates in the South Atlantic Ocean during the late austral summer 1995, *Deep-Sea Research I*, *46*, 451–482.

Fabry, V. J., B. A. Seibel, R. A. Feely, and J. C. Orr (2008), Impacts of ocean acidification on marine fauna and ecosystem processes, *ICES Journal of Marine Science*, *65*, 414–432.

Fabry, V. J., J. B. McClintock, J. T. Mathis, and J. M. Grebmeier (2009), Ocean Acidification at High Latitudes: The Bellwether, *Oceanography*, *22*(4), 160–171.

Falkowski, P. G., R. T. Barber, and V. V. Smetacek (1998), Biogeochemical controls and feedbacks on ocean primary production, *Science*, *281*(5374), 200–206, doi:10.1126/science.281.5374.200.

Feely, R. A., S. C. Doney, and S. R. Cooley (2009), Ocean Acidification: Present Conditions and Future Changes in a High-CO_2 World, *Oceanography*, *22*(4), 36–47.

Franck, V. M., M. A. Brzezinski, K. H. Coale, and D. M. Nelson (2000), Iron and silicic acid concentrations regulate Si uptake north and south of the Polar Frontal Zone in the Pacific Sector of the Southern Ocean, *Deep-Sea Research II*, *47*, 3315–3338.

Freeman, N. M., and N. S. Lovenduski (2015), Decreased calcification in the Southern Ocean over the satellite record, *Geophysical Research Letters*, doi:10.1002/2014GL062769.

Freeman, N. M., and N. S. Lovenduski (2016a), Mapping the Antarctic Polar Front: weekly realizations from 2002 to 2014, *Earth System Science Data*, *8*, 191–198, doi: 10.5194/essd-8-191-2016.

Freeman, N. M., and N. S. Lovenduski (2016b), Mapping the Antarctic Polar Front: Weekly realizations from 2002 to 2014, links to NetCDF file and MPEG4 movie, doi:10.1594/PANGAEA.855640.

Freeman, N. M., N. S. Lovenduski, and P. R. Gent (2016), Temporal variability in the Antarctic Polar Front (2002-2014), *Journal of Geophysical Research: Oceans*, *121*, 7263–7276, doi:10.1002/2016JC012145.

Frölicher, T. L., J. L. Sarmiento, D. J. Paynter, J. P. Krasting, and M. Winton (2014), Dominance of the Southern Ocean in anthropogenic carbon and heat uptake in CMIP5 models, *Journal of Climate*, *28*, 862–886.

Fyfe, J. C., and O. A. Saenko (2006), Simulated changes in the extratropical Southern Hemisphere winds and currents, *Geophysical Research Letters*, *33*(L06701), doi:10.1029/2005GL025332.

Garcia, H. E., R. A. Locarnini, T. P. Boyer, J. I. Antonov, O. K. Baranova, M. M. Zweng, J. R. Reagan, and D. R. Johnson (2014), Dissolved Inorganic Nutrients (phosphate, nitrate, silicate), in *World Ocean Atlas 2013*, *NOAA Atlas NESDIS*, vol. 4, edited by S. Levitus and A. Mishonov, p. 25.

Gille, S. T. (1994), Mean sea surface height of the Antarctic Circumpolar Current from Geosat data: Method and application, *Journal of Geophysical Research*, *99*, 255–273.

Gille, S. T. (2002), Warming of the Southern Ocean since the 1950s, *Science*, *295*(5558), 1275–1277.

Gille, S. T. (2008), Decadal-Scale Temperature Trends in the Southern Hemisphere Ocean, *Journal of Climate*, *21*, 4749–4765, doi:10.1175/2008JCLI2131.1.

Gille, S. T. (2014), Meridional displacement of the Antarctic Circumpolar Current, *Philosophical Transactions of the Royal Society A: Mathematical, Physical and Engineering Sciences*, *372*(20130273), doi:10.1098/rsta.2013.0273.

Giorgetta, M. A., et al. (2013), Climate and carbon cycle changes from 1850 to 2100 in MPI-ESM simulations for the Coupled Model Intercomparison Project phase 5, *J. Adv. Model. Earth Syst.*, *5*, 572–597, doi:10.1002/jame.20038.

Gordon, A. L., E. Molinelli, and T. Baker (1978), Large-Scale Relative Dynamic Topography of the Southern Ocean, *Journal of Geophysical Research*, *83*(C6).

Gordon, H. R., G. C. Boynton, W. M. Balch, S. B. Groom, D. S. Harbour, and T. J. Smyth (2001), Retrieval of coccolithophore calcite concentration from SeaWiFS imagery, *Geochemical Research Letters*, *28*(8), 1587–1590.

Graham, R. M., A. M. De Boer, K. J. Heywood, M. R. Chapman, and D. P. Stevens (2012), Southern Ocean fronts: Controlled by wind or topography?, *Journal of Geophysical Research: Oceans*, *117*(C08018), doi:10.1029/2012JC007887.

Gravalosa, J. M., J.-A. Flores, F. J. Sierro, and R. Gersonde (2008), Sea surface distribution of coccolithophores in the eastern Pacific sector of the Southern Ocean (Bellingshausen and Amundsen Seas) during the late austral summer of 2001, *Marine Micropaleontology*, *69*(1), 16–25, doi:10.1016/j.marmicro.2007.11.006.

HadGEM2 Development Team (2011), The HadGEM2 family of Met Office Unified Model climate configurations, *Geosci. Model Dev.*, *4*(3), 723–757, doi:10.5194/gmd-4-723-2011.

Hall, A., and M. Visbeck (2002), Synchronous Variability in the Southern Hemisphere Atmosphere, Sea Ice, and Ocean Resulting from the Annular Mode, *Journal of Climate*, *15*, 3043–3057, doi:10.1175/1520-0442(2002)015⟨3043:SVITSH⟩2.0.CO;2.

Haumann, F. A., D. Notz, and H. Schmidt (2014), Anthropogenic influence on recent circulation-driven Antarctic sea ice changes, *Geophysical Research Letters*, *41*, 8429–8437, doi:10.1002/2014GL061659.

Henson, S. A., J. L. Sarmiento, J. P. Dunne, L. Bopp, I. D. Lima, S. C. Doney, J. John, and C. Beaulieu (2010), Detection of anthropogenic climate change in satellite records of ocean chlorophyll and productivity, *Biogeosciences*, *7*, 621–640.

Ho, M., A. S. Kiem, and D. C. Verdon-Kidd (2012), The Southern Annular Mode: a comparison of indices, *Hydrology and Earth System Sciences*, *16*, 967–982, doi:10.5194/hess-16-967-2012.

Hoffmann, L. J., I. Peeken, and K. Lochte (2007), Effects of iron on the elemental stoichiometry during EIFEX and in the diatoms *Fragilariopsis kerguelensis* and *Chaetoceros dichaeta*, *Biogeosciences*, *4*, 569–579.

Hoffmann, L. J., I. Peeken, and K. Lochte (2008), Iron, silicate, and light co-limitation of three Southern Ocean diatom species, *Polar Biology*, *31*, 1067–1080, doi:10.1007/s00300-008-0448-6.

Hogg, A. M., M. P. Meredith, D. P. Chambers, E. P. Abrahamsen, C. W. Hughes, and A. K. Morrison (2015), Recent trends in the Southern Ocean eddy field, *Journal of Geophysical Research: Oceans*, *120*, 257–267, doi:10.1002/2014JC010470.

Holligan, P., A. Charalampopoulou, and R. Hutson (2010), Seasonal distributions of the coccolithophore, emiliania huxleyi, and of particulate inorganic carbon in surface waters of the scotia sea, *Journal of Marine Systems*, *82*(4), 195–205.

Howard, W. R., and W. L. Prell (1992), Late Quaternary Surface Circulation of the Southern Indian Ocean and its Relationship to Orbital Variations, *Paleoceanography*, *7*(1), 79–117, doi:10.1029/91PA02994.

Hughes, C. W., and E. R. Ash (2001), Eddy forcing of the mean flow in the Southern Ocean, *Journal of Geophysical Research: Oceans (1978–2012)*, *106*(C2), 2713–2722, doi:10.1029/2000JC900332.

Hunke, E., and W. Lipscomb (2008), *CICE: The Los Alamos sea ice model, documentation and software user's manual, version 4.0*, Los Alamos National Laboratory, Los Alamos, New Mexico.

Hurrell, J. W., et al. (2013), The Community Earth System Model: A framework for collaborative research, *Bulletin of the American Meteorological Society*, *94*, 1339–1360, doi:10.1175/BAMS-D-12-00121.1.

Iglesias-Rodriguez, M. D., P. R. Halloran, R. E. Rickaby, I. R. Hall, E. Colmenero-Hidalgo, J. R. Gittins, D. R. Green, T. Tyrrell, S. J. Gibbs, P. von Dassow, et al. (2008), Phytoplankton calcification in a high-CO_2 world, *Science*, *320*(5874), 336–340.

Johnson, R., P. G. Strutton, S. W. Wright, A. McMinn, and K. M. Meiners (2013), Three improved satellite chlorophyll algorithms for the Southern Ocean, *J. Geophys. Res.*, *118*, 3694–3703.

Karsten, R. H., and J. Marshall (2002), Constructing the residual circulation of the ACC from observations, *Journal of Physical Oceanography*, *32*, 3315–3327.

Kay, J. E., C. Deser, A. Phillips, A. Mai, C. Hannay, G. Strand, J. Arblaster, S. Bates, G. Danabasoglu, J. Edwards, M. Holland, P. Kushner, J.-F. Lamarque, D. Lawrence, K. Lindsay, A. Middleton, E. Munoz, R. Neale, K. Oleson, L. Polvani, and M. Vertenstein (2015), The Community Earth System Model (CESM) Large Ensemble Project: A Community Resource for Studying Climate Change in the Presence of Internal Climate Variability, *Bulletin of the American Meteorological Society*, *96*, 1333–1349, doi:10.1175/BAMS-D-13-00255.1.

Kemp, A. E. S., I. Grigorov, R. B. Pearce, and A. C. Naveira Garabato (2010), Migration of the Antarctic Polar Front through the mid-Pleistocene transition: evidence and climatic implications, *Quarternary Science Reviews*, *29*, 1993–2009.

Key, R. M., A. Olsen, S. van Heuven, S. K. Lauvset, A. Velo, X. Lin, C. Schirnick, A. Kozyr, T. Tanhua, M. Hoppema, S. Jutterström, R. Steinfeldt, E. Jeansson, M. Ishii, F. F. Perez, and T. Suzuki (2015), Global Ocean Data Analysis Project, Version 2 (GLODAPv2), *Tech. rep.*, ORNL/CDIAC-162, NDP-P093. Carbon Dioxide Information Analysis Center, Oak Ridge National Laboratory, US Department of Energy, Oak Ridge, Tennessee, doi: 10.3334/CDIAC/OTG.NDP093_GLODAPv2.

Khatiwala, S., F. Primeau, and T. Hall (2009), Reconstruction of the history of anthropogenic CO_2 concentrations in the ocean, *Nature*, *462*, 346–349.

Kim, Y. S., and A. H. Orsi (2014), On the variability of Antarctic Circumpolar Current fronts inferred from 1992-2011 altimetry, *Journal of Physical Oceanography*, *44*, 3054–3071, doi:10.1175/JPO-D-13-0217.1.

Kohfeld, K. E., R. M. Graham, A. M. de Boer, L. C. Sime, E. W. Wolff, C. Le Quéré, and L. Bopp (2013), Southern Hemisphere westerly wind changes during the Last Glacial Maximum: paleo-data synthesis, *Quarternary Science Reviews*, *68*, 76–95, doi:10.1016/j.quascirev.2013.01.017.

Kostianoy, A. G., A. I. Ginzburg, M. Frankignoulle, and B. Delille (2004), Fronts in the Southern Indian ocean as inferred from satellite sea surface temperature data, *Journal of Marine Systems*, *45*, 55–73, doi:10.1016/j.jmarsys.2003.09.004.

Krumhardt, K. M., N. S. Lovenduski, M. C. Long, and K. Lindsay (2017), Avoidable impacts of ocean warming on marine primary production: Insights from the CESM ensembles, *Global Biogeochemical Cycles*, *31*, doi:10.1002/2016GB005528.

Landschützer, P., N. Gruber, F. A. Haumann, C. Rodenbeck, D. C. E. Bakker, S. van Heuven, M. Hoppema, N. Metzl, C. Sweeny, T. Takahashi, B. Tilbrook, and R. Wanninkhof (2015), The reinvigoration of the Southern Ocean carbon sink, *Science*, *349*(1221), doi:10.1126/science.aab2620.

Langer, G., G. Nehrke, I. Probert, J. Ly, and P. Ziveri (2009), Strain-specific responses of *Emiliania huxleyi* to changing seawater carbonate chemistry, *Biogeosciences Discussions*, *6*(2), 4361–4383, doi:10.5194/bgd-6-4361-2009.

Langlais, C., S. R. Rintoul, and A. Schiller (2011), Variability and mesoscale activity of the Southern Ocean fronts: Identification of a circumpolar coordinate system, *Ocean Modelling*, *39*, 79–96, doi:10.1016/j.ocemod.2011.04.010.

Lauvset, S. K., R. M. Key, A. Olsen, S. van Heuven, A. Velo, X. Lin, C. Schirnick, A. Kozyr, T. Tanhua, M. Hoppema, S. Jutterström, R. Steinfeldt, E. Jeansson, M. Ishii, F. F. Perez, T. Suzuku, and S. Watelet (2016), A new global interior ocean mapped climatology: the 1° x 1° GLODAP version 2, *Earth System Science Data*, *8*, 325–340, doi:10.5194/essd-8-325-2016.

Legeckis, R. (1977), Oceanic Polar Front in the Drake Passage - satellite observations during 1976, *Deep-Sea Research*, *24*, 701–704, doi:10.1016/0146-6291(77)90510-0.

Leung, S., A. Cabré, and I. Marinov (2015), A latitudinally banded phytoplankton response to 21st century climate change in the Southern Ocean across the CMIP5 model suite, *Biogeosciences*, *12*, 5715–5734, doi:10.5194/bg-12-5715-2015.

Lewis, E., and D. W. R. Wallace (1998), Program developed for CO_2 system calculations, *Carbon Dioxide Information and Analysis Center Report, ORNL/CDIAC-105*.

Lovenduski, N. S., G. A. McKinley, A. R. Fay, K. Lindsay, and M. C. Long (2016), Partitioning uncertainty in ocean carbon uptake projections: internal variability, emission scenario, and model structure, *Global Biogeochemical Cycles*, *30*, 1276–1282, doi: 10.1002/2016GB005426.

Mackintosh, N. A. (1946), The Antarctic Convergence and the distribution of surface temperatures in Antarctic waters, *Discovery Rep.*, *XXIII*, 177–212.

Marinov, I., A. Gnanadesikan, J. R. Toggweiler, and J. L. Sarmiento (2006), The Southern Ocean biogeochemical divide, *Nature*, *441*(7096), 964–967.

Marinov, I., S. C. Doney, and I. D. Lima (2010), Response of ocean phytoplankton community structure to climate change over the 21st century: Partitioning the effects of nutrients, temperature and light, *Biogeosciences*, *7*(12), 3941–3959, doi:10.5194/bg-6-3941-2010.

Marshall, G. J. (2003), Trends in the Southern Annular Mode from Observations and Reanalyses, *Journal of Climate*, *16*, 4134–4143, doi:10.1175/1520-0442(2003)016⟨4134:TITSAM⟩2.0.CO;2.

Marshall, J., and K. Speer (2012), Closure of the meridional overturning circulation through Southern Ocean upwelling, *Nature Geoscience*, *5*, 171–180, doi:10.1038/NGEO1391.

Martin, J. H. (1990), Glacial-interglacial CO_2 change: The iron hypothesis, *Paleoceanography*, *5*(1), 1–13.

McCartney, M. S. (1982), The subtropical recirculation of Mode Waters, *Reprint from Journal of Marine Research*, *40*(Supplement), 427–464.

Meijers, A. J. S. (2014), The Southern Ocean in the Coupled Model Intercomparison Project phase 5, *Phil. Trans. R. Soc. A*, *372*(20130296), doi:10.1098/rsta.2013.0296.

Meredith, M. P. (2016), Understanding the structure of changes in the Southern Ocean eddy field, *Geophysical Research Letters*, *43*, 5829–5832, doi:10.1002/2016GL069677.

Mignone, B. K., A. Gnanadesikan, J. L. Sarmiento, and R. D. Slater (2006), Central role of Southern Hemisphere winds and eddies in modulating the oceanic uptake of anthropogenic carbon, *Geophysical Research Letters*, *33*(L01604), doi:10.1029/2005GL024464.

Mikaloff Fletcher, S. E., N. Gruber, A. R. Jacobson, S. C. Doney, S. Dutkiewicz, M. Gerber, M. Follows, F. Joos, K. Lindsay, D. Menemenlis, A. Mouchet, S. A. Müller, and J. L. Sarmiento (2006), Inverse estimates of anthropogenic CO_2 uptake, transport, and storage by the ocean, *Global Biogeochemical Cycles*, *20*(GB2002), doi:10.1029/2005GB002530.

Mikaloff Fletcher, S. E., N. Gruber, A. R. Jacobson, M. Gloor, S. C. Doney, S. Dutkiewicz, M. Gerber, M. Follows, F. Joos, K. Lindsay, D. Menemenlis, A. Mouchet, S. A. Müller, and J. L. Sarmiento (2007), Inverse estimates of the oceanic sources and sinks of natural CO_2 and the implied oceanic carbon transport, *Global Biogeochemical Cycles*, *21*(GB1010), doi:10.1029/2006GB002751.

Mohan, R., L. P. Mergulhao, M. V. Guptha, A. Rajakumar, M. Thamban, N. AnilKumar, M. Sudhakar, and R. Ravindra (2008), Ecology of coccolithophores in the Indian sector of the Southern Ocean, *Marine Micropaleontology*, *67*, 30–45, doi:10.1016/j.marmicro.2007.08.005.

Moore, J. K., and M. R. Abbott (2000), Phytoplankton chlorophyll distributions and primary production in the Southern Ocean, *Journal of Geophysical Research: Oceans*, *105*(C12), 28,709–28,722, doi:10.1029/1999JC000043.

Moore, J. K., and M. R. Abbott (2002), Surface chlorophyll concentrations in relation to the Antarctic Polar Front: seasonal and spatial patters from satellite observations, *Journal of Marine Systems*, *37*, 69–86.

Moore, J. K., and O. Bracuher (2008), Sedimentary and mineral dust sources of dissolved iron to the world ocean, *Biogeosciences*, *5*(3), 631–656, doi:10.5194/bg-5-631-2008.

Moore, J. K., M. R. Abbott, and J. G. Richman (1997), Variability in the location of the antarctic polar front (90^o-20^ow) from satellite sea surface temperature data, *Journal of Geophysical Research*, *102*(C13), 27,825–27,833.

Moore, J. K., M. R. Abbott, and J. G. Richman (1999), Location and dynamics of the Antarctic Polar Front from satellite sea surface temperature data, *Journal of Geophysical Research: Oceans*, *104*(C2), 3059–3073, doi:10.1029/1998JC900032.

Moore, J. K., S. C. Doney, and K. Lindsay (2004), Upper ocean ecosystem dynamics and iron cycling in a global three-dimensional model, *Global Biogeochemical Cycles*, *18*(GB4028), doi:10.1029/2004GB002220.

Moore, J. K., K. Lindsay, S. C. Doney, M. C. Long, and K. Misumi (2013), Marine ecosystem dynamics and biogeochemical cycling in the Community Earth System Model [CESM1(BGC)]: Comparison of the 1990s with the 2090s under the RCP4.5 and RCP8.5 scenarios, *Journal of Climate*, *26*(23), 9291–9312, doi:10.1175/JCLI-D-12-00566.1.

Morrow, R., G. Valladeau, and J. B. Sallée (2008), Observed subsurface signature of Southern Ocean sea level rise, *Progress in Oceanography*, *77*(4), 351–366, doi:10.1016/j.pocean.2007.03.002.

Munro, D. R., N. S. Lovenduski, T. Takahashi, B. B. Stephens, T. Newberger, and C. Sweeney (2015a), Recent evidence for a strengthening CO_2 sink in the Southern Ocean from carbonate system measurements in the Drake Passage (2002-2015), *Geophysical Research Letters*, *42*, doi:10.1002/2015GL065194.

Munro, D. R., N. S. Lovenduski, B. B. Stephens, T. Newberger, K. R. Arrigo, T. Takahashi, P. D. Quay, J. Sprintall, N. M. Freeman, and C. Sweeney (2015b), Estimates of net community production in the Southern Ocean determined from time series observations (2002-2011) of nutrients, dissolved inorganic carbon, and surface ocean pCO_2 in Drake Passage, *Deep-Sea Res II*, *114*, 49–63, doi:10.1016/j.dsr2.2014.12.014.

Murnane, R. J., J. L. Sarmiento, and C. Le Quéré (1999), Spatial distribution of air-sea CO_2 fluxes and the interhemispheric transport of carbon by the oceans, *Global Biogeochemical Cycles*, *13*(2), 287–305, doi:10.1029/1998GB900009.

Oke, P. R., and M. H. England (2004), Oceanic response to changes in the latitude of the Southern Hemisphere subpolar westerly winds, *Journal of Climate*, *17*, 1040–1054, doi: 10.1175/1520-0442(2004)017⟨1040:ORTCIT⟩2.0.CO;2.

Olsen, A., R. M. Key, S. van Heuven, S. K. Lauvset, A. Velo, X. Lin, C. Schirnick, A. Kozyr, T. Tanhua, M. Hoppema, S. Jutterström, R. Steinfeldt, E. Jeansson, M. Ishii, F. F. Pérez, and T. Suzuku (2016), The Global Ocean Data Analysis Project version 2 (GLODAPv2) - an internally consistent data product for the world ocean, *Earth System Science Data*, *8*, 297–323, doi:10.5194/essd-8-297-2016.

Orsi, A. H., and U. Harris (2001), Locations of the various fronts in the Southern Ocean, Australian Antarctic Data Centre - CAASM Metadata.

Orsi, A. H., T. W. III, and W. D. N. Jr. (1995), On the meridional extent and fronts of the Antarctic Circumpolar Current, *Deep Sea Research Part I: Oceanographic Research Papers*, *42*(5), 641–673, doi:10.1016/0967-0637(95)00021-W.

Painter, S. C., A. J. Poulton, J. T. Allen, R. Pidcock, and W. M. Balch (2010), The COPAS'08 expedition to the Patagonian Shelf: Physical and environmental conditions during the 2008 coccolithophore bloom, *Continental Shelf Research*, *30*, 1907–1923, doi: 10.1016/j.csr.2010.08.013.

Palter, J. B., J. L. Sarmiento, A. Gnanadesikan, J. Simeon, and R. D. Slater (2010), Fueling export production: nutrient return pathways from the deep ocean and their dependence on the Meridional Overturning Circulation, *Biogeosciences*, *7*(11), 3549–3568, doi:10.5194/bg-7-3549-2010.

Pollard, R. T., M. I. Lucas, and J. F. Read (2002), Physical controls on biogeochemical zonation in the Southern Ocean, *Deep Sea Research Part II*, *49*, 3289–3305.

Pondaven, P., O. Ragueneau, P. J. Tréguer, A. Hauvespre, L. Dezileau, and J. L. Reyss (2000), Resolving the 'opal paradox' in the Southern Ocean, *Nature*, *405*, 168–172.

Read, J. F., and R. T. Pollard (1993), Structure and transport of the Antarctic Circumpolar Current and Agulhas Return Current at 40^{o}E, *Journal of Geophysical Research: Oceans (1978–2012)*, *98*(C7), 12,281–12,295.

Rembauville, M., J. Meilland, P. Ziveri, R. Schiebel, S. Blain, and I. Salter (2016), Planktic foraminifer and coccolith contribution to carbonate export fluxes over the central Kerguelen Plateau, *Deep-Sea Research I*, *111*, 91–101, doi:10.1016/j.dsr.2016.02.017.

Remote Sensing Systems (2016), [updated Dec 2015], Monthly Mean Wind Speed Data Set on a 1 degree grid made from Remote Sensing Systems Version-7 Microwave Radiometer Data, V0701, [accessed on 26 Jan 2016], Santa Rosa, CA, USA. Available at www.remss.com.

Renwick, J. A. (2002), Southern Hemisphere Circulation and Relations with Sea Ice and Sea Surface Temperature, *Journal of Climate*, *15*, 3058–3068, doi:10.1175/1520-0442(2002)015⟨3058:SHCARW⟩2.0.CO;2.

Reynolds, R. W., and T. M. Smith (1994), Improved global sea surface temperature analyses using optimum interpolation, *Journal of Climate*, *7*, 929–948.

Riebesell, U., I. Zondervan, B. Rost, P. D. Tortell, R. E. Zeebe, and F. M. M. Morel (2000), Reduced calcification of marine plankton in response to increased atmospheric CO_2, *Nature*, *407*, 2–5.

Rignot, E., J. L. Bamber, M. R. van den Broeke, C. Davis, Y. Li, W. J. van de Berg, and E. van Meijgaard (2008), Recent Antarctic ice mass loss from radar interferometry and regional climate modelling, *Nature Geoscience*, *1*, 106–110, doi:10.1038/ngeo102.

Rintoul, S. R., C. Hughes, and D. Olbers (2001), The Antarctic Circumpolar Current System, in *Ocean Circulation and Climate*, edited by G. Siedler, J. Church, and J. Gould, pp. 271–302, Academic Press.

Sabine, C. L., R. A. Feely, N. Gruber, R. M. Key, K. Lee, J. L. Bullister, R. Wanninkhof, C. S. Wong, D. W. R. Wallace, B. Tilbrook, F. J. Millero, T.-H. Peng, A. Kozyr, T. Ono, and A. F. Rios (2004), The oceanic sink for anthropogenic CO_2, *Science*, *305*(5682), 367–371, doi:10.1126/science.1097403.

Sabine, C. L., S. Hankin, H. Koyuk, D. C. E. Bakker, B. Pfeil, A. Olsen, N. Metzl, A. Kozyr, A. Fassbender, A. Manke, J. Malczyk, J. Akl, S. R. Alin, R. G. J. Bellerby, A. Borges, J. Boutin, P. J. Brown, W. J. Cai, F. P. Chavez, A. Chen, C. Cosca, R. A. Feely, M. González-Dávila, C. Goyet, N. Hardman-Mountford, C. Heinze, M. Hoppema, C. W. Hunt, D. Hydes, M. Ishii, T. Johannessen, R. M. Key, A. Körtzinger, P. Landschützer, S. K. Lauvset, N. Lefèvre, A. Lenton, A. Lourantou, L. Merlivat, T. Midorikawa, L. Mintrop, C. Miyazaki, A. Murata, A. Nakadate, Y. Nakano, S. Nakaoka, Y. Nojiri, A. M. Omar, X. A. Padin, G. H. Park, K. Paterson, F. F. Perez, D. Pierrot, A. Poisson, A. F. Ríos, J. Salisbury, J. M. Santana-Casiano, V. V. S. S. Sarma, R. Schlitzer, B. Schneider, U. Schuster, R. Sieger, I. Skjelvan, T. Steinhoff, T. Suzuki, T. Takahashi, K. Tedesco, M. Telszewski, H. Thomas, B. Tilbrook, D. Vandemark, T. Veness, A. J. Watson, R. Weiss, C. S. Wong, and H. Yoshikawa-Inoue (2013), Surface Ocean CO2 Atlas (SOCAT) gridded data products, *Earth System Science Data*, *5*, 145–153, doi:10.5194/essd-5-145-2013.

Sadeghi, A., T. Dinter, M. Vountas, B. Taylor, M. Altenburg-Soppa, and A. Bracher (2012), Remote sensing of coccolithophore blooms in selected oceanic regions using the

PhytoDOAS method applied to hyper-spectral satellite data, *Biogeosciences*, *9*, 2127–2143, doi:10.5194/bg-9-2127-2012.

Sallée, J. B., K. Speer, and R. Morrow (2008), Response of the Antarctic Circumpolar Current to Atmospheric Variability, *Journal of Climate*, *21*(12), 3020–3039.

Sallée, J. B., R. J. Matear, S. R. Rintoul, and A. Lenton (2012), Localized subduction of anthropogenic carbon dioxide in the Southern Hemisphere oceans, *Nature Geoscience*, *5*, doi:10.1038/NGEO1523.

Sarmiento, J. L., T. M. C. Hughes, R. J. Stouffer, and S. Manabe (1998), Simulated response of the ocean carbon cycle to anthropogenic climate warming, *Nature*, *393*, 245–249, doi:10.1038/30455.

Sarmiento, J. L., N. Gruber, M. A. Brzezinski, and J. P. Dunne (2004), High-latitude controls of thermocline nutrients and low latitude biological productivity, *Nature*, *427*, 56–60.

Sarmiento, J. L., J. Simeon, A. Gnanadesikan, N. Gruber, R. M. Key, and R. Schlitzer (2007), Deep ocean biogeochemistry of silicic acid and nitrate, *Global Biogeochemical Cycles*, *21*(GB1S90), doi:10.1029/2006GB002720.

Sarthou, G., K. R. Timmermans, S. Blain, and P. J. Tréguer (2005), Growth physiology and fate of diatoms in the ocean: a review, *Journal of Sea Research*, *53*, 25–42, doi:10.1016/j.seares.2004.01.007.

Sen Gupta, A., and M. H. England (2006), Coupled Ocean-Atmosphere-Ice Response to Variations in the Southern Annular Mode, *Journal of Climate*, *19*, 4457–4486, doi:10.1175/JCLI3843.1.

Sigman, D. M., and E. A. Boyle (2000), Glacial/interglacial variations in atmospheric carbon dioxide, *Nature*, *407*.

Sloyan, B. M., and S. R. Rintoul (2001), Circulation, renewal, and modification of Antarctic Mode and Intermediate Water, *Journal of Physical Oceanography*, *31*, 1005–1030.

Smetacek, V. (1999), Diatoms and the ocean carbon cycle, *Protist*, *150*, 25–32.

Smetacek, V., H. J. W. de Barr, U. V. Bathmann, K. Lochte, and M. M. Rutgers van der Loeff (1997), Ecology and biogeochemistry of the Antarctic Circumpolar Current during austral spring: a summary of Southern Ocean JGOFS cruise ANT X/6 of R.V. *Polarstern*, *Deep Sea Research Part II*, *44*(1–2), 1–21.

Smetacek, V., P. Assmy, and J. Henjes (2004), The role of grazing in structuring Southern Ocean pelagic ecosystems and biogeochemical cycles, *Antarctic Science*, *16*(4), 541–558, doi:10.1017/S0954102004002317.

Smith, R. D., et al. (2010), *The Parallel Ocean Program (POP) reference manual*, Los Alamos National Laboratory, Los Alamos, New Mexico [Available at http://www.cesm.ucar.edu/models/cesm1.0/pop2/doc/sci/POPRefManual.pdf].

Smith, W. H., and D. T. Sandwell (1994), Bathymetric prediction from dense satellite altimetry, *Journal of Geophysical Research*, *99*(B11), 21,803–21,824.

Smith, W. O., and J. C. Comiso (2008), Influence of sea ice on primary production in the southern ocean: A satellite perspective, *Journal of Geophysical Research: Oceans (1978–2012)*, *113*(C05S93).

Sokolov, S., and S. R. Rintoul (2002), Structure of Southern Ocean fronts at 140^{o}E, *Journal of Marine Systems*, *37*, 151–184.

Sokolov, S., and S. R. Rintoul (2007a), Multiple Jets of the Antarctic Circumpolar Current South of Australia, *Journal of Physical Oceanography*, *37*, 1394–1412, doi:10.1175/JPO3111.1.

Sokolov, S., and S. R. Rintoul (2007b), On the relationship betwen fronts of the Antarctic Circumpolar Current and surface chlorophyll concentrations in the Southern Ocean, *J. Geophys. Res.*, *112*, doi:10.1029/2006jc004072.

Sokolov, S., and S. R. Rintoul (2009a), Circumpolar structure and distribution of the Antarctic Circumpolar Current fronts: 1. Mean circumpolar paths, *Journal of Geophysical Research*, *114*(C11018), doi:10.1029/2008JC005108.

Sokolov, S., and S. R. Rintoul (2009b), Circumpolar structure and distribution of the Antarctic Circumpolar Current fronts: 2. Variability and relationship to sea surface height, *Journal of Geophysical Research*, *14*(C11019).

Sprintall, J. (2003), Seasonal to interannual upper-ocean variability in the Drake Passage, *Journal of Marine Research*, *61*, 27–57, doi:10.1357/002224003322586408.

Sprintall, J. (2008), Long-term trends and interannual variability of temperature in Drake Passage, *Progress in Oceanography*, *77*(4), 316–330, doi:10.1016/j.pocean.2006.06.004.

Stephens, B. B., and R. F. Keeling (2000), The influence of Antarctic sea ice on glacial-interglacial CO_2 variations, *Nature*, *404*.

Stephenson, G. R., Jr., S. T. Gille, and J. Sprintall (2013), Processes controlling upper-ocean heat content in Drake Passage, *Journal of Geophysical Research: Oceans*, *118*, 4409–4423, doi:10.1002/jgrc.201315.

Swart, N. C., and J. C. Fyfe (2012), Observed and simulated changes in the Southern Hemisphere surface westerly wind-stress, *Geophysical Research Letters*, *39*(L16711), doi:10.1029/2012GL052810.

Swart, N. C., J. C. Fyfe, N. Gillett, and G. J. Marshall (2015), Comparing Trends in the Southern Annular Mode and Surface Westerly Jet, *Journal of Climate*, *28*, 8840–8859, doi:10.1175/JCLI-D-15-0334.1.

Swart, S., and S. Speich (2010), An altimetry-based gravest empirical mode south of Africa: 2. Dynamic nature of the Antarctic Circumpolar Current fronts, *Journal of Geophysical Research*, *115*(C03003), doi:10.1029/2009JC005300.

Takahashi, T., R. Williams, and D. Bos (1982), Carbonate chemistry, in *GEOSECS Pacific Expedition, Volume 3, Hydrographic Data 1973-1974*, pp. 77–83.

Taylor, K. E., R. J. Stouffer, and G. A. Meehl (2012), An overview of CMIP5 and the experiment design, *Bulletin of the American Meteorological Society*, *93*, 485–498, doi: 10.1175/BAMS-D-11-00094.1.

Thompson, D. W. J., and J. M. Wallace (2000), Annular Modes in the Extratropical Circulation. Part I: Month-to-Month Variability, *Journal of Climate*, *13*, 1000–1016.

Thompson, D. W. J., and J. M. Wallace (2001), Regional climate impacts of the Northern Hemisphere Annular Mode, *Science*, *293*(5527), 85–89.

Thompson, D. W. J., J. M. Wallace, and G. C. Hegerl (2000), Annular Modes in the Extratropical Circulation. Part II: Trends, *Journal of Climate*, *13*, 1018–1036, doi: 10.1175/1520-0442(2000)013⟨1018:AMITEC⟩2.0.CO;2.

Thompson, D. W. J., S. Solomon, P. J. Kushner, M. H. England, K. M. Grise, and D. J. Karoly (2011), Signatures of the Antarctic ozone hole in Southern Hemisphere surface climate change, *Nature Geoscience*, *4*, 741–749, doi:10.1038/ngeo1296.

Toggweiler, J. R. (2009), Shifting Westerlies, *Science*, *323*, doi:10.1126/science.1169823.

Toggweiler, J. R., J. L. Russell, and S. R. Carson (2006), Midlatitude westerlies, atmospheric CO_2, and climate change during the ice ages, *Paleoceanography*, *21*(PA2005), doi:10.1029/2005PA001154.

Tréguer, P. J. (2014), The Southern Ocean silica cycle, *Comptes Rendus Geoscience*, *346*, 279–286, doi:10.1016/j.crte.2014.07.003.

Trull, T. W., S. R. Rintoul, M. Hadfield, and E. R. Abraham (2001), Circulation and seasonal evolution of polar waters south of Australia: implications for iron fertilization of the Southern Ocean., *Deep-Sea Res., Part II*, *48*(11-12), 2439–2466.

Uppstrom, L. (1979), The boron/chloronity ratio to deep-sea water from the Pacific Ocean, *Deep-Sea Research*, *21*, 161–162.

Wake, B. (2015), Marine Biogeochemistry: Calcification changes, *Nature Climate Change*, *5*(4), 300–300, doi:10.1038/nclimate2601.

Wentz, F. J. (2015), A 17-yr climate record of environmental parameters derived from the Tropical Rainfall Measuring Mission (TRMM) Microwave Imager, *Journal of Climate*, *28*, 6882–6902, doi:10.1175/JCLI-D-15-0155.1.

Wentz, F. J., C. Gentemann, D. Smith, and D. Chelton (2000), Satellite Measurements of Sea Surface Temperature Through Clouds, *Science*, *288*, 847–850, doi:10.1126/science.288.5467.847.

Zhang, Z. M., M. Lewis, M. Lee, B. Johnson, and G. Korotaev (2002), The volume scattering function of natural bubble population, *Limnology and Oceanography*, *47*(5), 1273–1282.

Zondervan, I., R. E. Zeebe, B. Rost, and U. Riebesell (2001), Decreasing marine biogenic calcification: A negative feedback on rising atmospheric $p\mathrm{CO}_2$, *Global Biogeochemical Cycles*, *15*, 507–516, doi:10.1029/2000GB001291.

Appendix A

Supplementary Material for Chapter 2

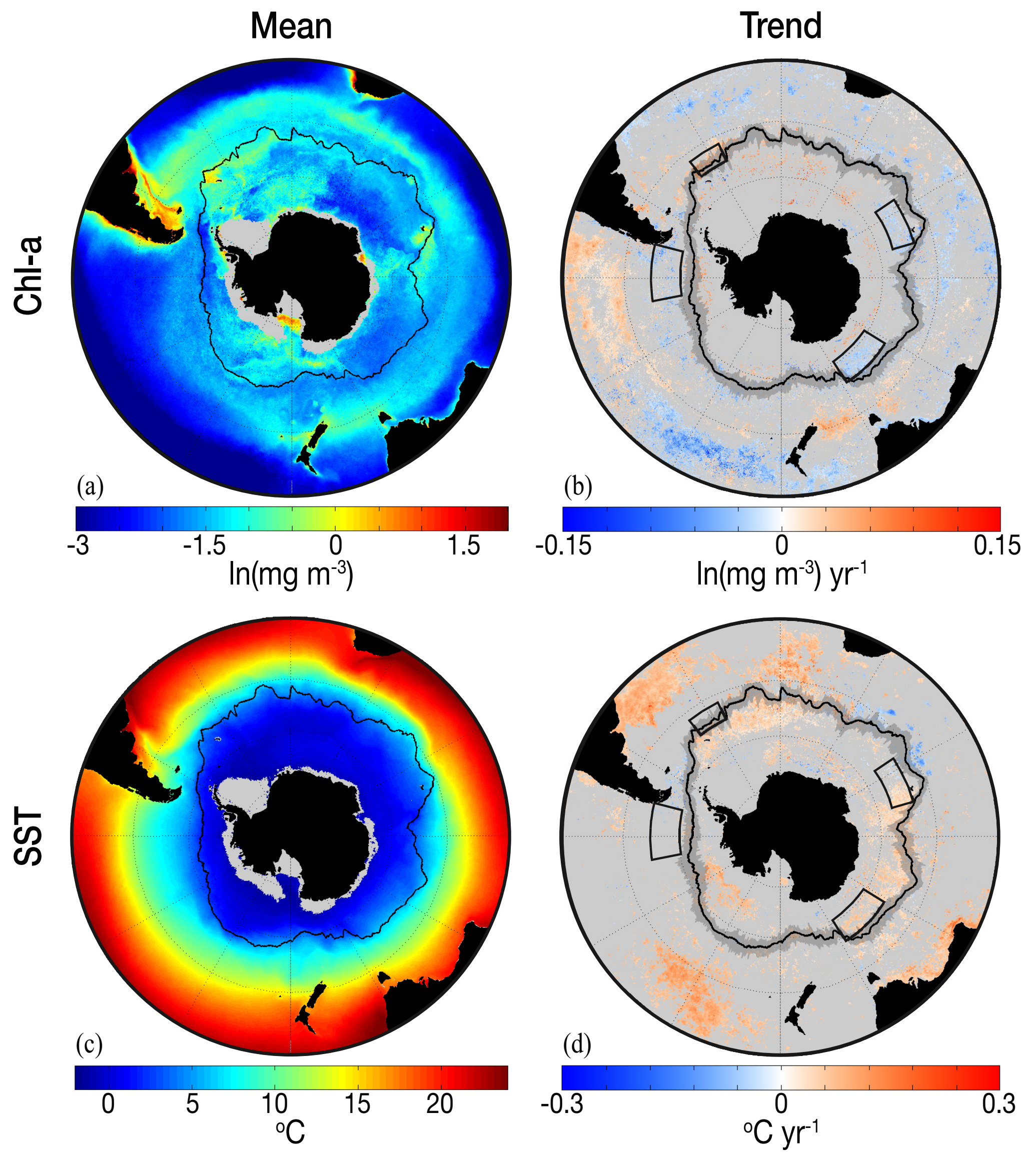

Figure A.1: Maps of Southern Ocean (>30° S) summer (DJF) mean state of (a) chlorophyll-a concentration and (c) sea surface temperature (SST) and linear trends in (b) chlorophyll and (d) SST, corrected for the presence of summer sea ice (see Section 2.3). Only those trends with significance ≥95% are shown. The black line and gray shading in (b) and (d) indicate the average summer location of the Antarctic Polar Front (see Section 2.3). Boxes in (b) and (d) indicate the same regions as in Figure 2.1.

Table A.1: Carbonate analyses data information table.

	SURFACE [CO_3^{2-}] (Figure 3a)							
	Carbon Parameter							
input	**fCO$_2$**[a]	**pCO$_2$**[b]	**Alkalinity**[c]	**Silicate**[d]	**Phosphate**[d]	**Salinity**[d]	**SST**[e]	**Pressure**[f]
time frame	1998-2011	1998-2013	climatology				concurrent with f/pCO$_2$ measurement	
format method	austral summer mean concentrations from all data collected during DJF		average of the DJF months from each climatology				austral summer mean values from monthly data	austral summer mean values from monthly means
	WATER COLUMN [CO_3^{2-}] (Figure 3b)							
input	**TCO$_2$**		**Alkalinity**	**Silicate**	**Phosphate**	**Salinity**	**Temp.**	**Pressure**
type	bottle[g]					CTD[g]		
available years	1994, 1996, 1998, 2001, 2003 (only samples taken in D, J, and/or F)							
format method	for a given year, [CO_3^{2-}] estimated at each sample location, then binned according to latitude (every 1 deg.) and depth (every 20 m)							

[a] Surface Ocean CO_2 Atlas gridded data products (*Sabine et al.*, 2013).
[b] Global Surface pCO_2 (LDEO) Database V2013 (http://cdiac.ornl.gov/oceans/LDEO_Underway_Database/).
[c] LDEO Surface Gridded Carbon Parameters dataset (http://www.ldeo.columbia.edu/res/pi/CO2/carbondioxide/global_ph_data/).
[d] World Ocean Atlas 2013 (http://nodc.noaa.gov/).
[e] Merged satellite time series detailed in main text (Figure S1c,d): Level-3 AVHRR Oceans Pathfinder (1997-2009; http://science.oregonstate.edu/ocean.productivity/) and MODIS-Aqua (2002-2014; http://oceancolor.gsfc.nasa.gov/).
[f] NCEP/NCAR Reanalysis monthly surface product from NOAA/OAR/ESRL PSD, Boulder, Colorado, USA (http://www.esrl.noaa.gov/psd/).
[g] SR03 (south of Australia), CLIVAR & Carbon Hydrographic Data Office (http://cchdo.ucsd.edu/).

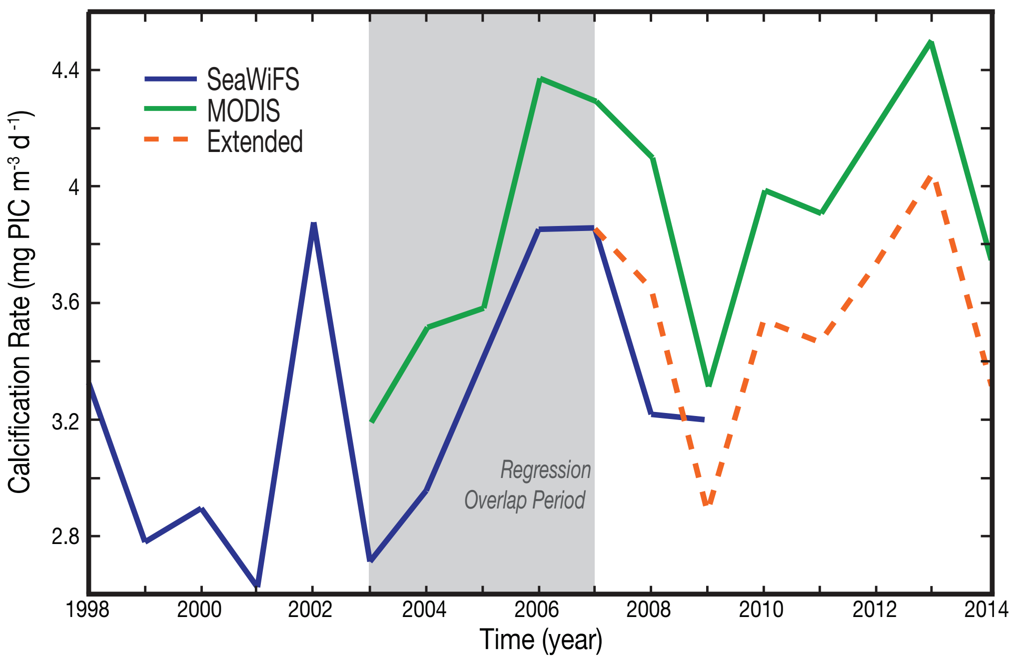

Figure A.2: Example of regression method, combing calcification rates calculated from SeaWiFS (1997–2009) and MODIS-Aqua (2002–2014) datasets, following *Brown and Arrigo* (2012). Time series of the grid point located at 50°S and 37°W (found within Region 1). Gray shading indicates time period of overlap period used (2003–2007).

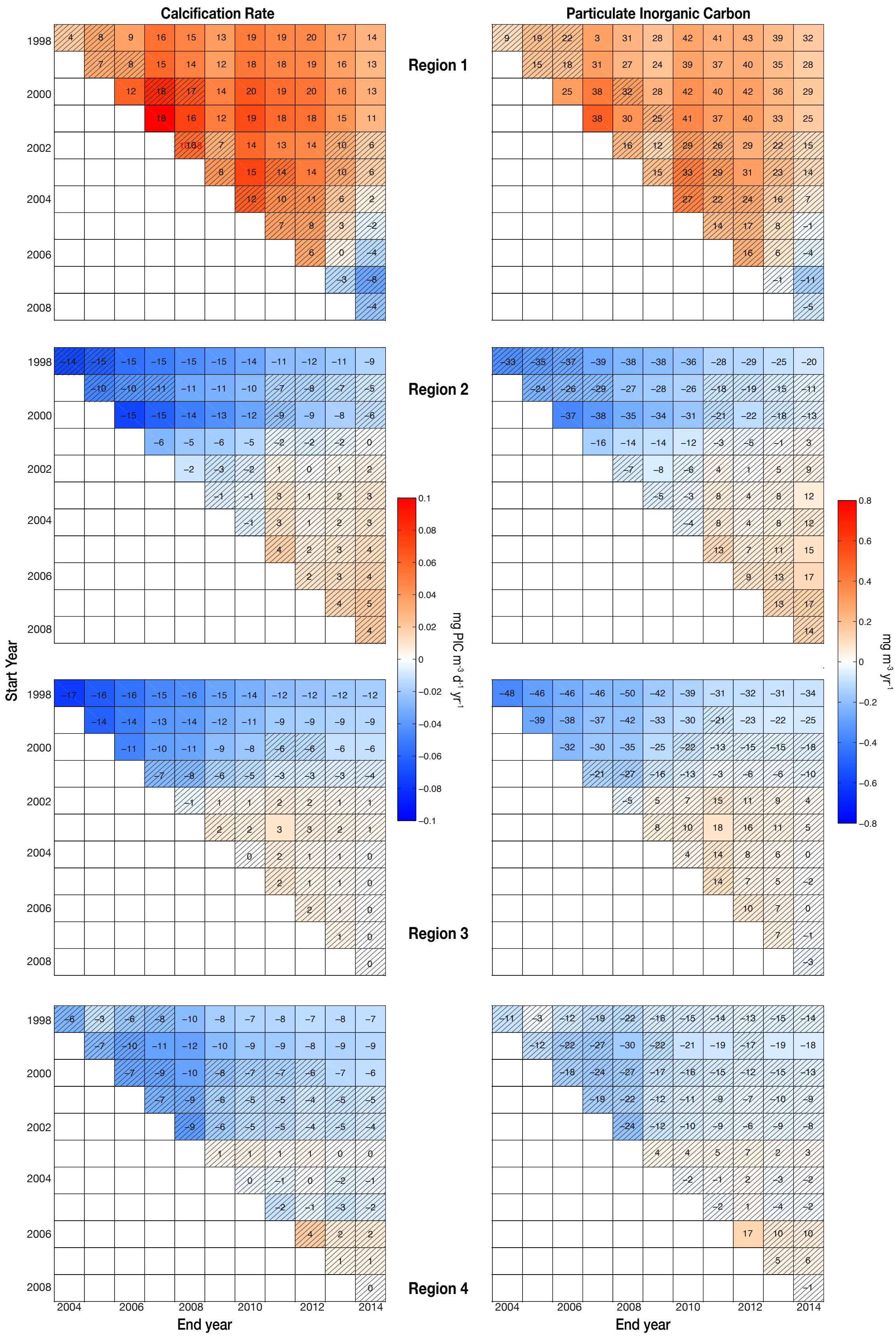

Figure A.3: Positive (warm), negative (cool) trends in mean calcification rate by region with varying start and end years (trends not significant at the ≥95% significance level are hatched).

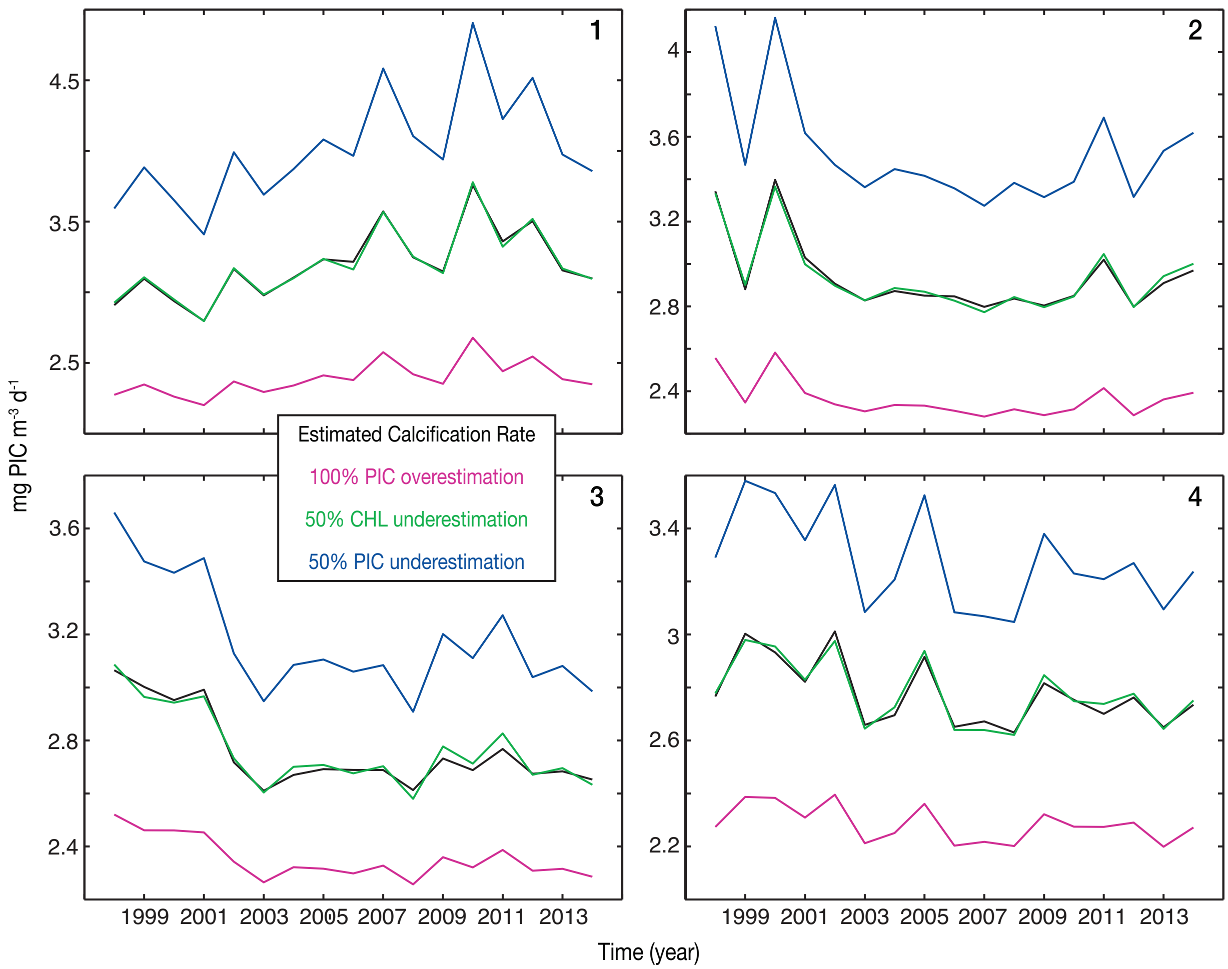

Figure A.4: Sensitivity tests for over-/underestimation of PIC or chlorophyll-a concentration in computing calcification rate for boxed regions; region number indicated in top right corner of each.

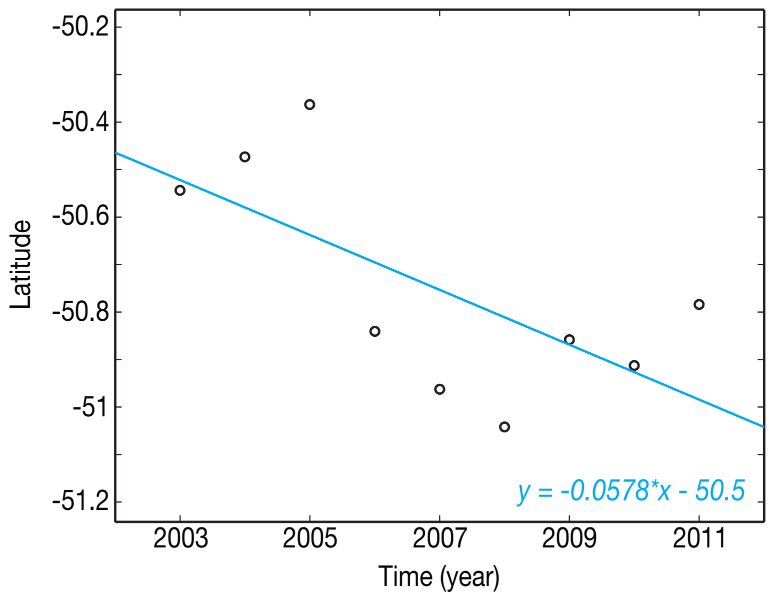

Figure A.5: Time series and significant (at 95% level) fitted linear trend line (cyan) of the summer mean latitudinal location of the Antarctic Polar Front within Region 4.